Università degli Studi di Roma “La Sapienza”

Facoltà di Ingegneria

Tesi per il Conseguimento del Titolo di Dottore in Ricerca in:

Elettromagnetismo - XVII ciclo - a. a. 2003/2004

All-optical processing by second order nonlinearities

Candidato:

Alessio Bosco

Docenti Guida:

Char.mo Prof. Mario Bertolotti
Char.mo Prof. Eugenio Fazio

Coordinatore:

Char.mo Prof. Giorgio Gerosa

Contents

Part III: *Soliton Generation by Photorefractive Effect*

Introduction

The evolution in the efficiency of the communication systems is intrinsically characterized by the increasing of the information flow that is possible to exchange. Starting from the few bits per sec. possible with electro-mechanic technologies (telegraph), trough the Mbit/sec of the coaxial cables, radio and satellite connections, telecommunication systems reached the Tbit/sec thanks to the recent development of optical fibers technologies. This strong difference depends especially on the extremely large band available. Indeed, in optical networks the information carrier has frequency much higher (190-380 THz) and lower attenuation than in electronic and radio connections. The enormous band theoretically displaced (of the order of THz) could transport over than 15,000,000 of vocal signals through a single cable [Practical realization like FLAG (Fiber-Optic Link Around the Globe) transcontinental cable can approximate this limit, thus reaching 10 Gbit/sec full-duplex].

The recent development of ultrafast photonic network architectures, based on binary modulated packets of optical pulses, has led to the obvious demand for all-optical digital processing[1,2]. Indeed, nowadays the handling of optical data (for instance address recognition, routing, switching and calculation) still remains an open question, being the transmitted information mainly manipulated in electronic way. This means that the optical signals need to be converted to electronic and vice versa (see an example in Fig. I.1) any time they are received or sent. In fact, all-optical processing, acting directly on light signals, would allow these networks to keep their high bandwidths by reducing the need to work at the lower speed of electronic rates, thus maintaining the high speed of optical data.

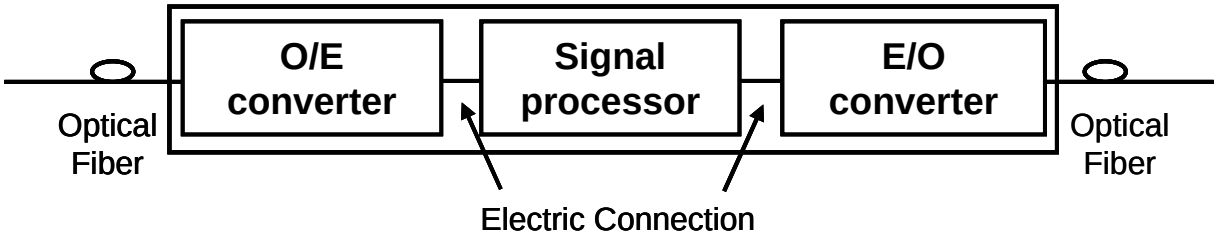

Fig. I.1 Schematic example of a optical fiber network when a signal processing is needed.

Considering all-optical processing devices, different functionalities should be covered for different purposes: among all possible scenarios, three main functionalities has been identified and analysed in the present thesis, introducing new experimental configurations which present many advantages with respect to the equivalent electronic devices.

First of all “all-optical processing” means the possibility of doing logical and algebraic operations using just light. Thus at the beginning a new configuration for logic gates and algebraic operation is shown, both theoretically and experimentally. Such proposed devices are based on parametric frequency conversion. This procedure has many advantages, among which the possibility of parallel operation and the non-resonant response of the materials represent the biggest ones. The former allows bit-to-bit calculus of arrays of binary numbers at once, while the latter allows the operation with bits encoded by ultra-short light pulses (few tens of femtoseconds), at really high repetition rates (10^{13}-10^{14} bits/s). Those processes have been studied both in bulk $\chi^{(2)}$ crystal and composed structures [usually referred to as one-dimensional photonic crystals (1D PhC)]. The technology of PhC, whose structure can be engineered to increase the conversion efficiency of some order of

magnitude, is indeed really promising to reduce the dimensions down to few micrometers, towards a future possibility of integration.

A limiting factor for these applications is given by the conversion efficiency of the parametric frequency conversion, that is usually relatively low and nonlinear, which means it scales with the intensity. Consequently such proposed devices become more and more precise if really high light intensities are adopted which, on the contrary, cannot be used in optical and photonic circuits. In order to overpass such limitation, a parallel line has been followed and new configurations of all-optical switching devices have been proposed. They are studied within resonant cavities and are based not just on amplitude modulation but also in nonlinear phase modulation given by nonlinear conversion processes. This new procedure will strongly reduce the threshold intensities necessary to switch the device thanks to the increasing of interaction length given by the cavity feedback.

Clearly all-optical signal processing means not just switching but also addressing information by light: thus the last proposed configuration will describe experiments devoted to write addressable waveguides by light, which means the generation of spatial optical solitons[3]. Spatial solitons represent at the moment the best possibility to realise planar and channel waveguides with both ultra-low losses and ultra-low dispersion. This occurs because “spatial soliton” means light propagating without diffraction within a material modification realised by the light itself, and consequently optimised for modal propagation. This is a big advantage with respect to any other light waveguide: in the commonly used waveguides the index profile is designed by a man-project or by the chemical-physical processes

used to built them. Instead solitons write their own waveguides in order to propagate without diffraction. Soliton waveguides remain written and can be used further on. Moreover solitons can interact one-each-other and change their optical path. Based on such phenomena many logical gates have been already proposed in literature.

This work describes these all-optical proposals, based on second order nonlinearities, capable to perform "*on the fly*" bit-level functions such as address recognition, packet header modification and data integrity verification. It has been divided in three parts, each one dealing with one of the three identified and already discussed problematics.

In the first part (Chapters 1 and 2) it is presented the experimental realization of all-optical logical gates, fundamental elements to implement a full addition of binary optical words. This binary full-adder function, which could be used for the network applications mentioned above, from a more general point of view, obviously adds, to the range of digital optical processing, capability that is required for generalized optical computing[4]. The idea on which they are based is the three fields interaction such as type-II SHG and parametric down amplification. In particular, in chapter 1 the main lines of this new proposed technology are drawn. Besides several possible processing functionalities (for instance multiplexing and de-multiplexing) implementable by using this technology are discussed. In chapter 2 is illustrated that the nonlinear response of the materials can increase by performing the same processes in 1D PhC.

The second part (Chapter 3) is devoted to the problem of efficiency enhancement by using a nonlinear Fabry-Perot cavity. The possibility to switch a

ultra-low-intensity (~W/cm^2) light signal by amplitude and phase modulation occurring in parametric down amplification processes have been studied from the theoretical point of view. The studied process was totally independent from the input phase of the interacting beams and the threshold intensity of the pump of the parametric amplifier, able to switch the signal from the reflection to the transmission (or vice versa) is really low (10^5-10^6 W/cm^2), both qualities needed for any possible applications in the range of the photonics fiber transmission.

The last three chapters, forming the third part of this work, are dedicated to generation of spatial solitons. I studied in this work solitons generation by using photorefractive effect[5,6] (driven by second order nonlinearity), which allows to produce such kind of beams with intensity several orders of magnitude lower (W/cm2) than any other possible way (cascading $\chi^{(2)}$ processes, Kerr and other $\chi^{(3)}$ nonlinearities, etc..). In particular, chapter 4 describes the generation of solitons at 514nm wavelength, which is in the visible range. In chapter 5 is illustrated a totally new point of view of this effect for which it is possible to shift the working wavelength towards the infrared region commonly used for optical fiber transmission. Finally the last chapter deals with the generation of solitons by ultrafast (65 fs) light pulses instead of common continues wave (CW) laser beam.

References

1. 1 D. Cotter, J.K. Lucek, P. Gunning, D.G. Moodie, A.J. Poustie, K.J. Blow, R.J. Manning, in: A. Hasegawa Ed. , New Trends in Optical Soliton Communications, Kluwer Academic, Dordrecht, 1998, pp. 367–380.

2. P.Shor, Proc. of the 35th Ann. Symp. on Fundamental of Computer Science, Los Alamitos, CA: IEEE Press, pg.124-134.
3. E. DelRe, B. Crosignani, and P. di Porto, in Spatial Solitons, edited by S. Trillo and W. Tourellas, Springer Series in Optical Sciences Vol. 82 (Springer, Berlin, 2001).
4. V.P. Heuring, H.F. Jordan, J.P. Pratt, Appl. Opt. 31 1992 p. 3213.
5. M. Segev, B. Crosignani, A. Yariv, and B. Fischer, Phys. Rev. Lett. 68, 923 (1992).
6. Crosignani, M. Segev, D. Engin, P. di Porto, A. Yariv, and G. J. Salamo, J. Opt. Soc. Am. B 10, 446 (1993).

PART I:

All-Optical calculus through Second Order Nonlinearities

Chapter 1

All-optical algebra based on $\chi^{(2)}$ nonlinearity

1.1 Introduction

All-optical signal processing such as demultiplexing, wavelength conversion, regeneration and Boolean logic will play a critical role in the development of ultrafast photonic network architectures. The capability of this technology to handle a single ultra-high speed data channel exclusively in the optical domain without opto-electrical conversions can significantly improve the performance of the photonic systems in terms of flexibility, scalability, wavelength management simplification, optical components minimization and cost reduction.

In order to realize the all-optical signal processing functions, several possible structures have been proposed. For instance, the first optical vectorial chip[1] was released in 2001. Slightly later, Andreoni et al.[2-3] studied the possibility to use nonlinear optical processes, such as holographic second harmonic generation[4,5] (SHG), for implementing all-optical logical gates.

Among many logic units, XOR and AND gates are fundamental to accomplish a binary algebra useful for realizing various functionalities such as packet switching, binary addiction and counting, data encoding and more generally optical processing. Following this line, the all-optical XOR and AND gates have been implemented exploiting the logical functionalities exhibited by second order non-linear processes

such as SHG and optical parametric down-amplification (PDA). In this configuration, two binary strips, encoded by transverse amplitude modulation, are processed directly bit by bit in an intrinsic parallel way.

1.2 Logic gates

The interactions examined are summarized by the notation shown in Fig.1.1. In Fig. 1.1(a) is represented the type-II SHG in low-efficiency conditions. For this interaction the input are two beams at the fundamental frequency (FF) ω, orthogonally polarized (nominally p- and s-). At the output three channels are present: two at the FF and one at the second harmonic (SH). In the high efficiency conditions, depicted in Fig.1.1(b), the two outputs at the FF are drawn by a dotted line since they wuold not be present when depletion occurs.

In Fig.1.1(c) and 1(d) the PDA is indicated by reverse symbols. The inputs are the SH and one polarization at the FF. After the interaction the beam at 2ω will amplify the injected FF polarization, and will generate the orthogonally polarized idler. Again there is a distinction between low and high efficiency condition: in the last case the SH signal at the output is represented by a dotted line, meaning the depletion could occur when both polarization are present at the input.

Let us now introduce, as shown in fig.1.2, the logical functions corresponding to the nonlinear processes illustrated previously. In those figures, the optical bits are considered being encoded on the transverse pattern of the input beams (the subscript 2 indicates the information encoded on the beam at the SH). Actually, in

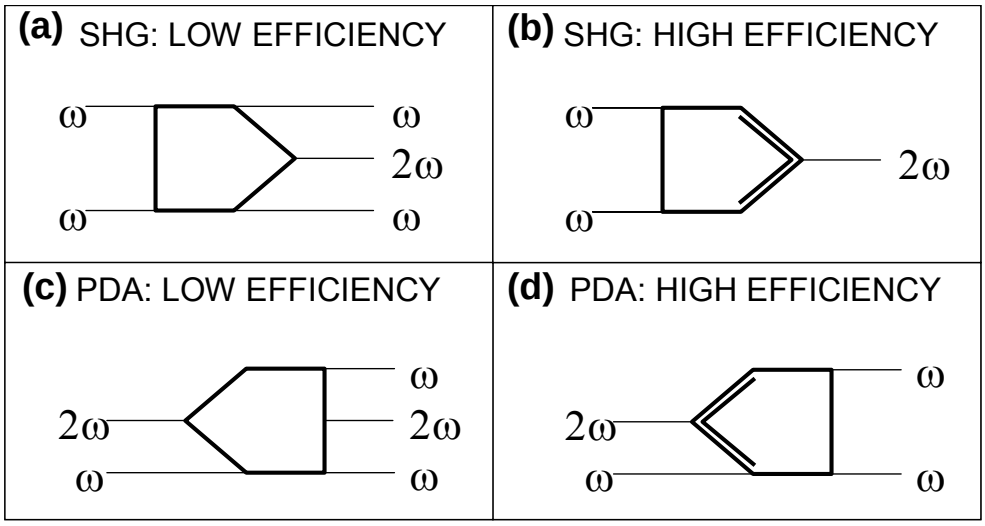

Fig. 1.1.Notation: (a) SHG signals in low efficiency conditions (b) SHG signals in high efficiency conditions where the dotted line means that if there are present both the inputs the outputs are depleted (c) PDA signals in low efficiency conditions (d) PDA signals in low efficiency conditions with a dotted line for second harmonic, possibly depleted. The arrows mean the double frequency (2ω) respect to fundamental (ω). For SHG and PDA reverse symbols are used.

type-II SHG, the SH beam is generated only in presence of both p- and s-polarized FF beams. The type-II SHG is then equivalent to the AND gate's output, that is a logic number 1 only if both of the input numbers are equal to 1 [as shown in fig.1.2(a) and fig.1.2(b)]. When the process occurs in low-efficiency conditions, the pump FF beams carrying the input information, respectively A and B, will propagate unaffectedly to the output. In the high-efficiency case the pump beams while interacting will get their intensity decreased. The output corresponding to the polarization of the input A is then equal to $\mathrm{A}\cdot NOT(\mathrm{B})$ (indicated in figures as A$\underline{\mathrm{B}}$), i. e. it is exactly A only if B=0 (no interaction occurs), otherwise is 0. The output at the other polarization is for symmetry $\underline{\mathrm{A}}$B.

Concerning the PDA interactions pictured in fig.1.2(c) and (d), the generated FF beam carries the information corresponding to $A \cdot B$ both in low- and high-efficiency conditions, occurring the process only in presence of both FF and SH fields.

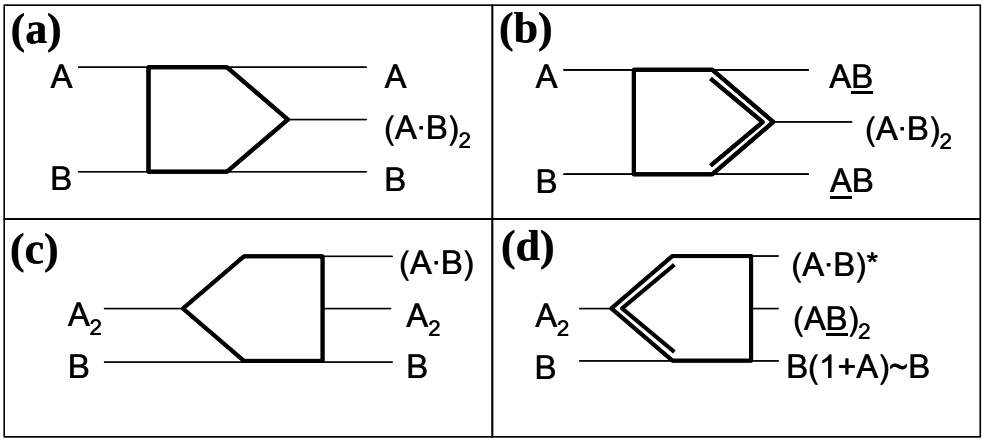

Fig. 1.2. Logic functionalities: (a) in low efficiency condition SHG the AND function of inputs is present at the output on second harmonic; (b) in high efficiency condition SHG at the output on FF are present $A \cdot \underline{B}$ on the first polarization, $B \cdot \underline{A}$ on the orthogonal one and on SH the AND of the inputs; (c) in low efficiency condition PDA the FF not present at the input give at the output the AND function of the inputs; (d) in high efficiency condition PDA the FF not present at the input give at the output the complex coniugate of the AND function of the inputs.

Using the functionalities previously discussed, it is possible to introduce the possible basic logic gates realizable with SHG and PDA. These logic gates are summarized in fig.1.3. In fig.1.3(a) and (b) the cross-identity are represented, that can be used to convert a signal from the FF to the SH [Up-Identity, U-I in fig.1.3(a)] and vice versa [Down-Identity, D-I fig.1.3(b)].

The implementation of a NOT gate is then described. Such a gate can be obtained using type-II SHG in high efficiency conditions. In these conditions, while

the SH is generated, the interacting FF beams will get depleted and the output will be 0. The implementation of the NOT gate might be obtained as schematized in fig.1.3(c). One of the two FF fields works as a supply for the gate: when the input is high (level 1) the two beams will interact and the FF residual beam will give an output low (level 0). Otherwise, if the input level is low, at the output there will be the unperturbed supply beam. In fig.1.3(d) is represented the Up-Not gate, that transfers, in a similar way, the NOT information of a bit, encoded on a FF beam, directly to the SH signal. Straightforward it is the implementation of the Up-AND gate, where the AND information is encoded on the SH output [fig.1.3(e)], and for the XOR gate [fig.1.3(f)], obtained by overlapping the output at the FF of the process described in fig.1.2(b).

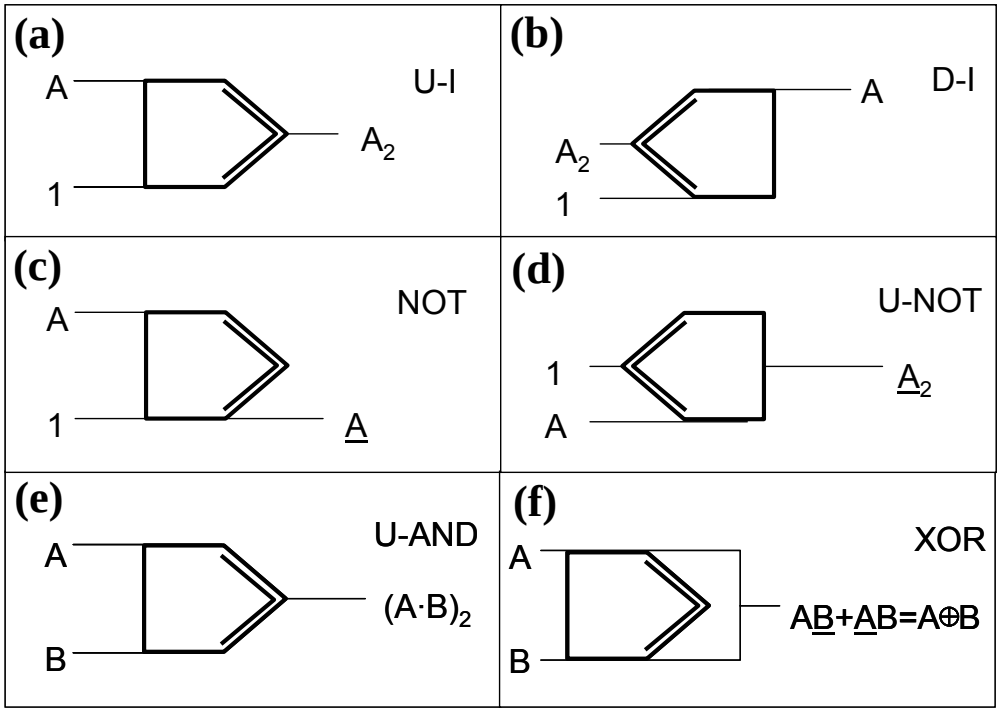

Fig. 1.3.Logic gates: (a) up-identity transform a signal in fundamental frequency to second harmonic; (b) down-identity changes a signal present on the SH to FF; (c) NOT function done using SHG; (d) up-NOT gives on second harmonic the input's negation; (e) up-AND function gives the AND of inputs to the output on SH; (f) XOR function obtained combining the two ouput polarizations on FF of a SHG in high efficiency conditions.

The simultaneous availability of a XOR and a AND logic functions, whose truth tables are reported in Tab. 1.1, will be of great interest as illustrated below.

A	B	AND(A,B)	XOR(A,B)
0	0	0	0
0	1	0	1
1	0	0	1
1	1	1	0

Tab. 1.1. AND and XOR gates' truth table

.

First of all, it needs to be highlighted that the SHG is not sufficient by itself to implement a fully equivalent AND gate. Indeed, considering the optical bit encoded on the transverse pattern of a laser beam, both input and output signals should be carried by beams that are homogeneous in wavelength. The above described D-I can be used for the frequency conversion of the output. Fig.1.4 shows the working scheme of the full-AND gate, having input and output signals with the same wavelength.

The last fundamental element which is possible to realize is the OR gate. Indeed, though a simple superposition of optical beams could appear as working like an OR gate, the output polarization will not be defined. The proposed structure, able to homogenize the output polarization, is shown in Fig.1.5. The output of the linear superposition, which can be polarized vertically (if for instance A=1 and B=0),

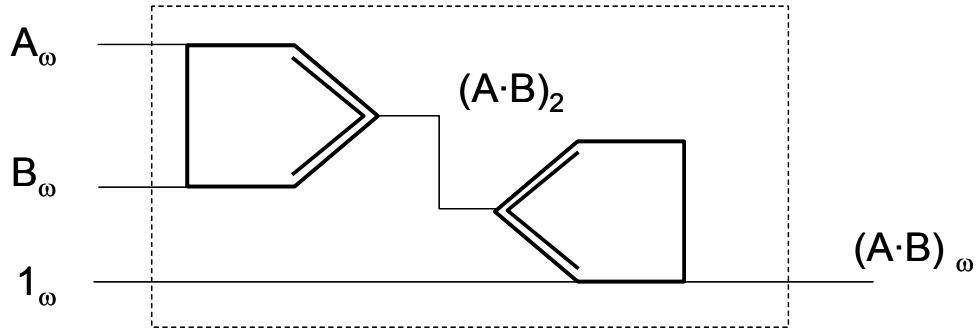

Fig. 1.4.Fully equivalent AND gate: two input signals and an idler enter in the system; the signals are combined by an AND gate giving an output on SH and then that output is transferred to the FF by the down-identity.

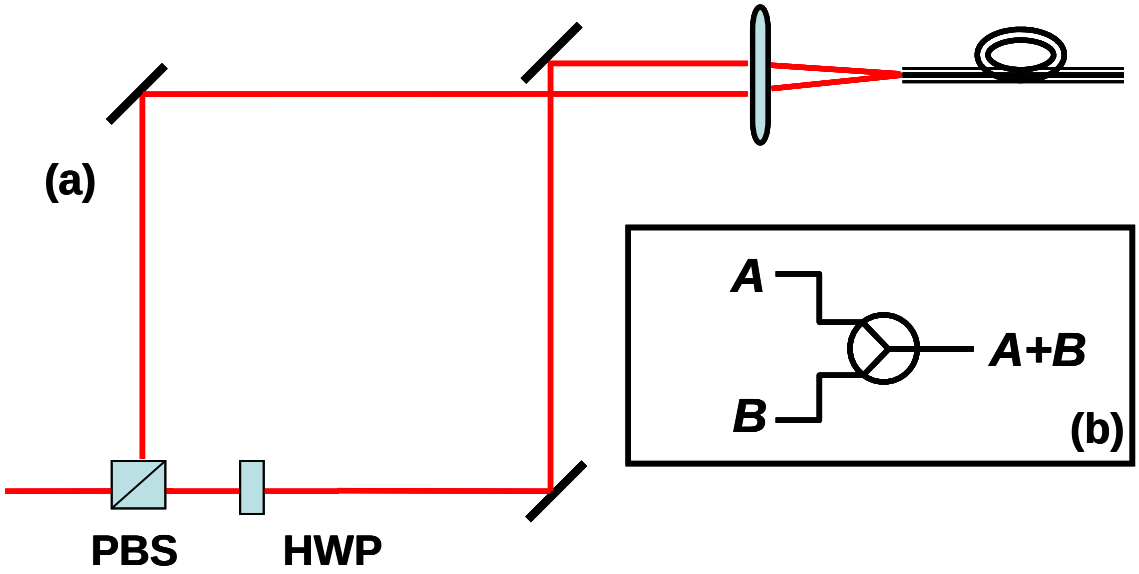

Fig. 1.5. All-optical OR gate: (a) physical realization and (b) symbolyic representation. The output of the linear superposition, which can be polarized vertically (if for instance A=1 and B=0), horizontally (A=0, B=1) or at 45 degrees, pass through a polarizer beam splitter (PBS), which identify two polarization channels. One of them is rotated in polarization by a half wave plate (HWP) and superposed again to the other one into a waveguide.

which identifies two polarization channels. One of them is rotated in polarization by a $\lambda/2$ wave plate and superposed again to the other one into a waveguide. This simple circuit will be indicated by the symbol in Fig.1.5(b); A and B appear as separated inputs indicating that they are distinguishable in polarization.

1.3 Experiment

The XOR logical gate was experimentally tested using the set-up as shown in Fig. 1.6. The laser system consisted of an amplified Ti-Sapphire laser providing 2ps-long pulses at λ=800nm, with energy of about 500μJ. A 50% beam splitter divided the beam in two arms that represent the input logical states. A half wave plate (WP) rotated the polarization of one beam to obtain, after the polarizing beam splitter (PBS), two cross-polarized beams. The crystal was a β-BaB_2O_4 (BBO) used in type-II phase- matched SHG of 800nm.

The mask used in this experiment was a pinhole 3mm wide whose image was reproduced on the BBO crystal by a 1m-long lens. The BBO crystal was in fact put 10cm further than the focal plane (fp) of the lens and the mask at distance 11m from that lens. In this way, the pinhole image was reduced, on the crystal, down to the 10% in dimension. The output logical state, which is encoded on the FF, was separated from the SH signal (carrying the AND information) by a dichroic mirror and visualized by a CCD camera. Following the XOR gate's truth table (tab. 1.1), it is demonstrated the possibility to implement such logical gate using type-II SHG in high

efficiency conditions. In these conditions, as discussed above, while the interacting beams are generating the SH, will get depleted and the output will be 0.

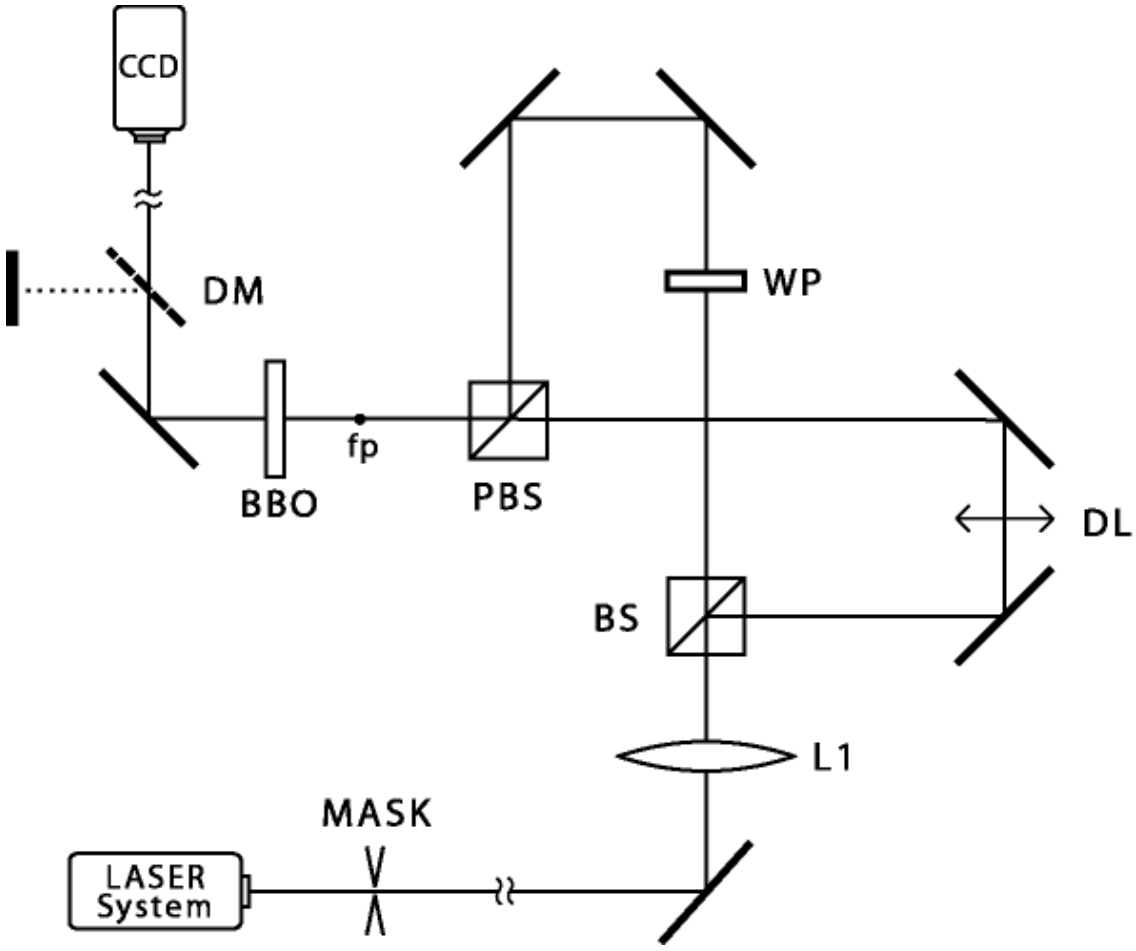

Fig. 1.6. Experimental set-up: the beam exits from the laser and passes through the mask, a pinhole whose image is formed on the crystal by a long-focal lens. Then the beam is divided into two arms by a beams splitter: the refracted beam passes through a $\lambda/2$ wave plate, thus rotating its polarization ; the reflected beam passes trough a delay line and it is combined with the other by a polarizer beam splitter. The two beams interacts into the crystal and then FF is divided from SH by a dichroic mirror and could be seen in the camera.

In Fig. 1.7 are depicted the output, taken by a CCD camera, of the AND [figs. 1.7(a)-1.7(d)] and of the XOR [figs.1.7(e)-1.7(h)] logical gates, corresponding to different input states. The input A is here encoded on the p-polarized beam and the B on the s-polarized beam. The energy of each interacting beam was about 70μJ on the crystal surface. The images of figs. 1.7(a) and 1.7(e) depict the trivial case when both input are 0. The pairs of Fig. 1.7(b), 1.7(f) and 1.7(c), 1.7(g) show the output corresponding to the AND and the XOR operations with input 1 and 0 whose result is 1 (respectively A=1, B=0 and A=0, B=1). In figs. 1.7(d) and 1.7(h) is instead reported the more interesting case in which both the input are equal to 1. As a matter of fact, in this case, the output intensity is approximately zero for the XOR gate [fig. 1.7(h)]. The beams are actually depleted down to the 20% each one. Choosing the zero-level of this logic as the 40% of our level one (here 70μJ), one may see that the system is working as a XOR gate.

1.4 Optical netwoks

What has been discussed above clarifies how a complete set of logical gates could be made.These fundamental elements could be arranged for synthesizing complex functionalities, both for arithmetic calculation (e. g. binary full-addition) and optical commutation (network switching of interconnection and the routing processes).

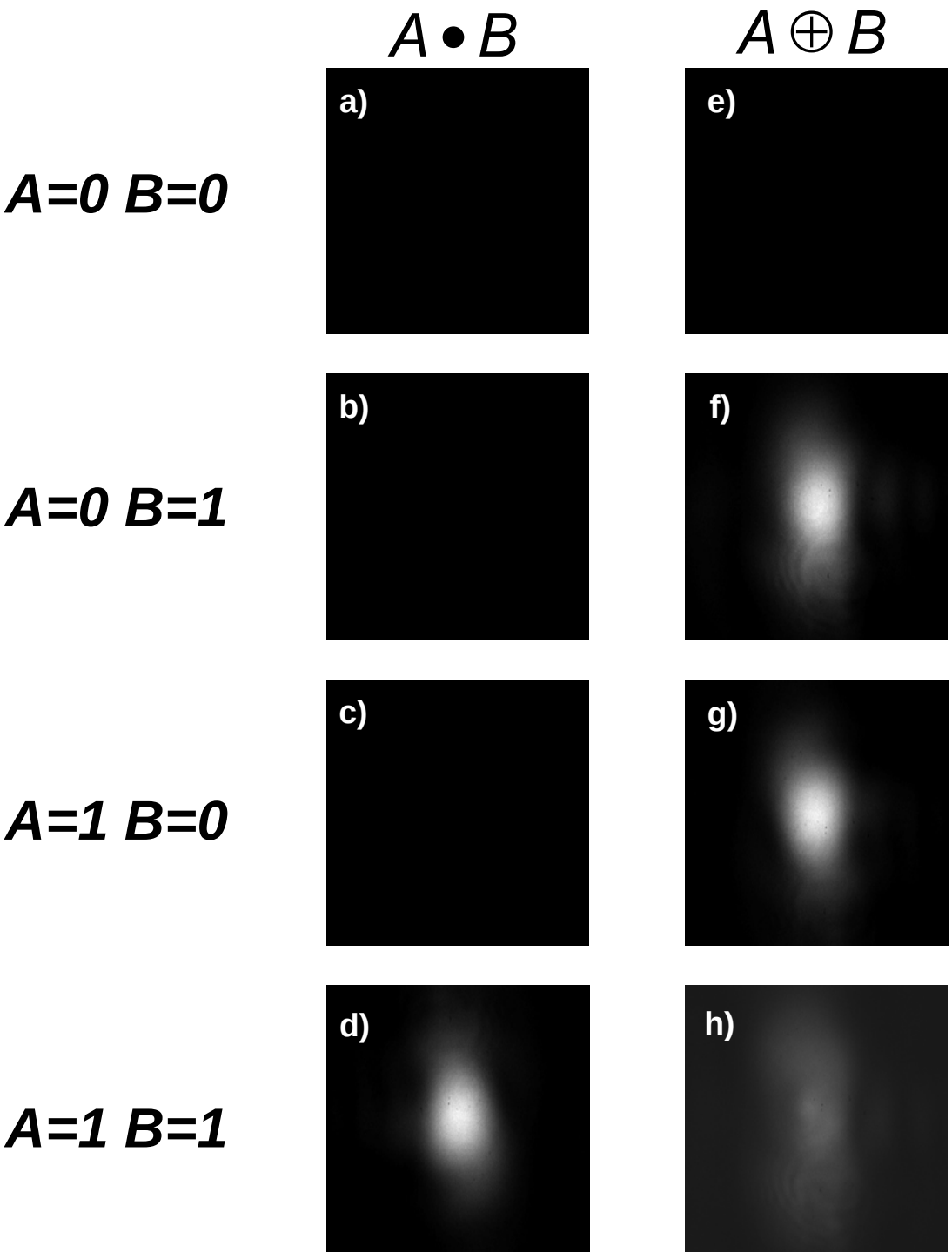

Fig. 1.7. Experimental results: (a)-(d) output of the SHG (AND gate); (e)-(h) putput of the depleted pump (XOR gate). The input are the following: (a), (e): A=0,B=0: (b), (f): A=0,B=1: (c), (g): A=1,B=0: (d), (h): A=1,B=1.

a) Arithmetic calculation

It has been shown that SHG, in strong conversion conditions, produces two results: the SH carries the AND function of the interacting beams (that can be successively converted to the FF), while the FF residual field brings the XOR information. This would be correspondent to the operational working of a half-adder, as shown in fig.1.8. Indeed, the number resulting from the sum of two binary numbers has digits that are given by the XOR operation of each summed bit. Moreover there is a carried-over digit which is brought by the AND operation. For instance, the sum 1+1 is the binary number 10, the bit 0 being the result of the XOR function (1 XOR 1), while the bit 1 (the carried-over) is the result of the AND function [see fig.1.7(d) and 1.7(h)].

The unit described previously is a self-consistent 1-bit-adder. To enlarge the number of bits that could be summed, the procedure is to implement a sequential algorithm which can be point out in few points:

1) Make a vector **XOR** (bit by bit) of two numbers using the unit described above;
2) Make a vector **AND** of two numbers (note that they are provided at the same time);
3) Shift the **AND** result obtained one bit left;
4) Make a vector **XOR** of the result of the point 1) with the binary number obtained at the point 3);
5) Repeat points 3) e 4) n-1 times where n is the total number of bits;

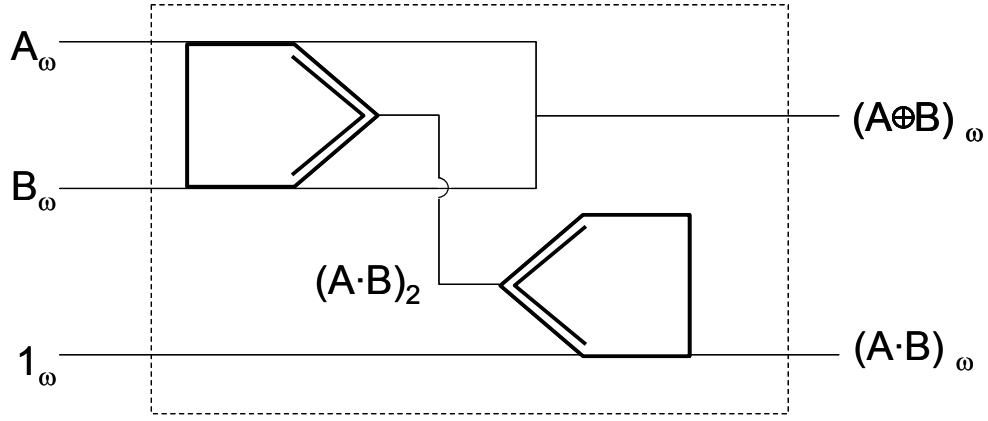

Fig. 1.8.All-optical one-bit adder: two inputs and an idler are injected into a SHG gate; the outputs on FF are combined giving the XOR function, the output on SH is inserted into a PDA calculating down identity. The result is an all-optical half-adder.

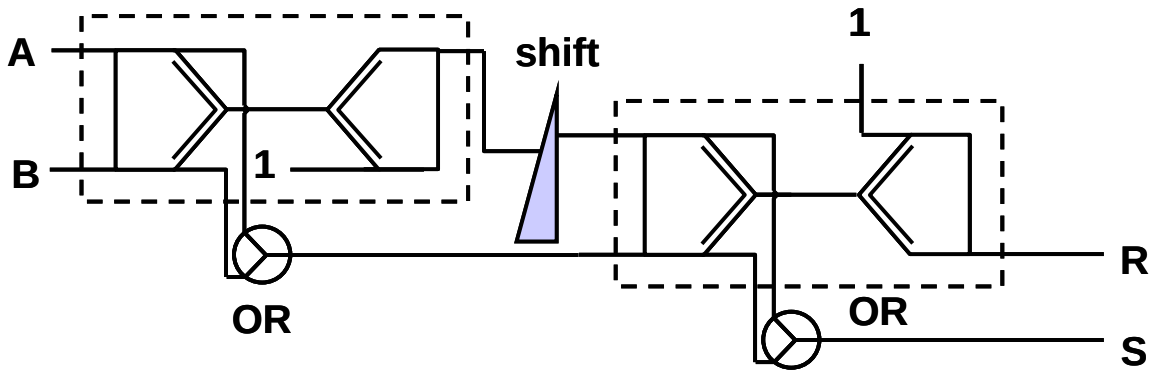

Fig. 1.9.All-optical 2-bit adder. The units in dotted-line box are the same of fig. 1.8 (optical half adder).The rest from the first operation (AND) is shifted to the left at each calculation step.

At the end of the process the sum is carried by the last AND step and the information on the rest (that is different from 0 only in case of overflow) by the last XOR.

For example, a possible implementation of an optical circuit, thought to execute the 2-bits arithmetic sum, whose Boolean algebraic representation is the following:

$$\begin{array}{lll} & A_1 & A_0 + \\ & B_1 & B_0 = \\ A_1 \cdot B_1 & (A_1 \oplus B_1) \oplus (A_0 \cdot B_0) & (A_0 \oplus B_0) \end{array}$$

The Boolean functions are, from left to right side, the carry, the bit more meaningful and the bit less meaningful. The optical circuit shown in Fig.1.9 could be obtained from this representation. Note that the rest is shifted to the left at each calculation step: this property does not depend on the number of bits involved in the process.

b) Commutation systems

In fig.1.10 are shown the logical schemes of multiplexing [fig.1.10(a)] and demultiplexing [fig.1.10(b)] circuits and their possible optical realization [figs.1.10(c) and 1.10(d)]. In the case of multiplexer [fig.1.10(a)] the two inputs A and B will be sent to the output depending on the logical value of the control signal C [the output U is indeed given by $A \cdot C + B \cdot \underline{C}$, where $\underline{C}$ stands for NOT(C)]. The demultiplexer works in a similar way: the input A interacts in two different AND gates with C and $\underline{C}$; it can be routed in the selected path.

The clear advantage in using the described technology is that these processes are completely parallel and it is possible to code multi-bit information on the section

of the beam without increasing the complexity of the network (the only limit is due by the possibility to code information on a section of the beam without diffraction).

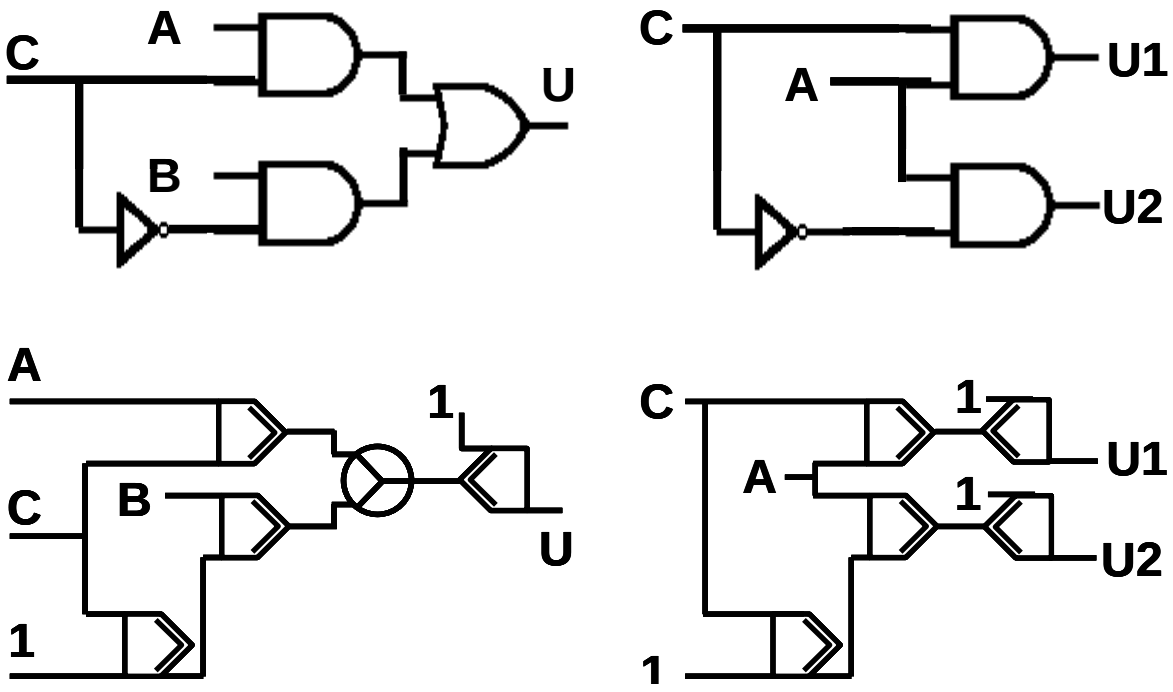

Fig. 1.10. Logical schemes of multiplexing (a) and demultiplexing (b) circuits and their possible optical realization (c) and (d).

References

1. http://www.lenslet.com
2. A.Andreoni, M.Bondani e M.Potenza , “Combinational tasks performed by second-harmonic-generated holograms”, Opt.Lett. 25 1570-1572 (2000).
3. A.Andreoni, M.Bondani e M.Potenza ,”Boolean algebra operations performed on optical bits by the generation of holografic fields through second-order nonlinear interactions”, Rev.Sc.Instr. 72 2525-2531 (2001).
4. B.I. Stepanov, E.V.Ivakin, A.S. Rubanov, Dokl.Akad.Nauk SSR, 196, 567-571 (1971).
5. A.Miniewicz, S.Bartkievicz, A.Januszko, J.Parka, J.Inclusion Phenom. 35, 317-320 (1999).

Chapter 2

$\chi(2)$ processes in ultracompact materials: 1D Photonic Crystals

2.1 Introduction

As shown in chapter 1, three fields interactions (in particular type-II SHG and parametric down amplification) might implement a complete all-optical algebra. Though the proposed technology exhibits many possible advantages, such as intrinsic parallelism and ultra-low delay, the increasing of integration level must be sought in order to reach and possibly overcome the actual skills of conventional electronics.

The reduction of dimensions of the materials used to perform these nonlinear processes is a mandatory step towards a possible future integration. The main point is that a dimensions reduction, if not linked to a contemporaneous growing of the nonlinear response, implies a decreasing of efficiency which is a critical aspect for the described technology. Finite one-dimensional (1D), periodic or quasi-periodic multi-layer stacks, usually referred to as 1D photonic crystals (PhCs), might be a solution to this question. These structures, in fact, may perform efficient parametric processes as widely demonstrated both theoretically and experimentally[1-7]. The main advantage that these artificial structures offer is the ability to enhance the nonlinear response normally associated with bulk $\chi^{(2)}$ materials thanks to the localization of light at frequencies tuned at the photonic band edge.

Moreover, they permit the tailoring of optical parameters. In fact, the natural dispersion of ordinary materials can be compensated by introducing geometrical dispersion, which is brought about and controlled by properly juxtaposing a high and a low index material. This effect may provide enough anomalous dispersion across the photonic band gap to make exact PM conditions[1-4] always possible. In particular, highly nonlinear materials such as gallium arsenide ($\chi^{(2)}$~120 pm/V), which cannot usually be phase-matched[1,7] because of their optical isotropy, could be used for second order nonlinear processes.

In this chapter, the first experimental evidence of a three field interaction (phase-matched, noncollinear, type-II SHG) in a 1D PhC is reported. The enhanced nonlinearity of the structure was 52 pm/V which is approximately 30 times higher than the BBO's one.

2.2 Design and realization of the sample

The structure (composed of 15 $Al_{(0.3)}Ga_{(0.7)}As/Al_2O_3$ periods) was designed according to a theoretical representation of the effective index of refraction[1] for a multi-layer structure, such that multiple scattering events are taken into account to all orders, and the result is a bulk medium with an effective index of refraction n_{eff}. Using this approach, PM conditions can be found by applying the effective momentum conservation law in 1D structures:

$$\vec{k}_{eff}^{(2\omega,p)} - \vec{k}_{eff}^{(\omega,p)} - \vec{k}_{eff}^{(\omega,s)} = \vec{0}$$

which, projected onto two components, one along the plane of the layers, and the other one perpendicularly to it, can be written as:

$$2n_{eff}^{(2\omega,p)} - n_{eff}^{(\omega,p)} - n_{eff}^{(\omega,s)} = 0 \qquad (2.1.a)$$

$$2sin(\theta_{2\omega,p}) - sin(\theta_{\omega,p}) - sin(\theta_{\omega,s}) = 0\,, \qquad (2.1.b)$$

where θ corresponds to the external incidence angle formed by each k-vector with the normal to the sample's surface; the labels *p, s*, ω and 2ω refer to the fields' polarizations and frequencies. For a finite periodic structure, Equation (2.1.a) is automatically satisfied when the two fundamental fields are tuned at the band edge resonance, and the SH is tuned at the second peak near the second-order band gap[1]. Equation (2.1.b) depends only on the incidence angles of the fields, as if the k-vector components did not feel the refractive index discontinuity.

According to Eqs. (2.1), exact, noncollinear PM for SHG of 1510nm fundamental wavelength was found for a 15-period structure composed of $Al_{(0.3)}Ga_{(0.7)}As$ (160nm)/Al_2O_3 (97nm). Total sample thickness was 3.5μm. A multi-layer structure of AlGaAs/AlAs was first grown on a 500μm-thick (100) GaAs substrate by solid-source molecular beam epitaxy. A 30nm GaAs cap was grown on the top of the multi-layer to protect the surface from subsequent oxidation. Successively, 20 μm-wide trenches were etched through the entire multi-layer by reactive-ion etching in order to expose the AlAs layers for lateral oxidation. The AlAs layers were oxidized by heating the sample at 410 C for 105 min in a H_2O atmosphere created by bubbling N_2 in a water bath at 85 C[8].

The schematic layout of the multi-layer structure and the real picture of the sample's top surface are shown in fig. 2.1; its active area is formed by 100μm broad stripes separated by 20μm etched trenches.

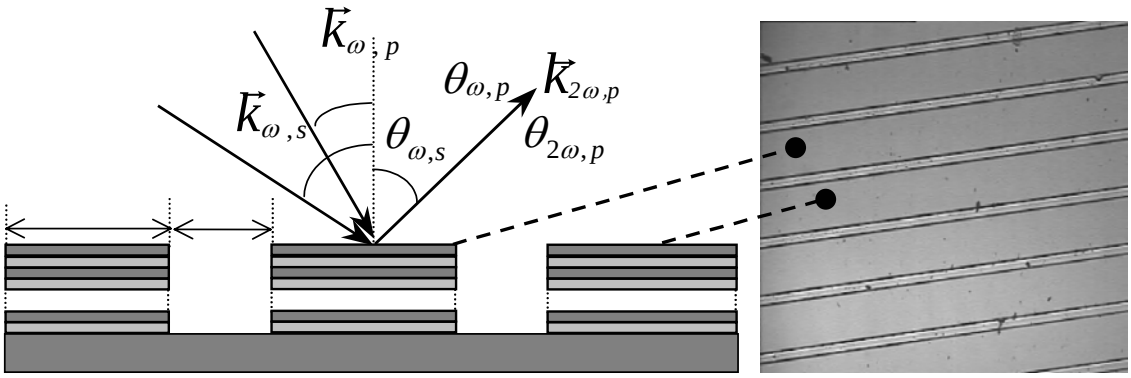

Fig. 2.1. Layout of the multi-layer structure (left view) and picture of the sample's top surface (right view). The largest stripes (100μm) form the active area of the photonic crystal.

2.3 Linear spectral analysis

A spectral analysis of the structure was performed with a micro-reflectometer connected to a Fourier-transform analyzer. Reflection spectra were recorded at several incident angles, for both s- and p-polarizations. The spot-size was set to fit a single active stripe, a procedure that allowed checking the sample homogeneity by comparing different spectra from several stripes. Fig. 2.2(a) depicts the experimental reflectivity spectra around the fundamental wavelength for p-polarized beam incident at an external angle of 30 degrees, and fig. 2.2(b) for s-polarized beam incident at 57

degrees. The “p” spectrum around the second harmonic wavelength for an angle of 43.5 degrees is illustrated in fig. 2.2(c). For these angles, the two fundamental beams at 1510 nm are tuned to the first resonance peak closest to the band-gap, while the p-polarized SH beam is tuned to the second peak close to the second order band-gap (the position of the wavelength in the spectra is marked by arrows). As discussed above, this condition ensures that noncollinear type II phase-matching at 1510 nm, as expected from the design.

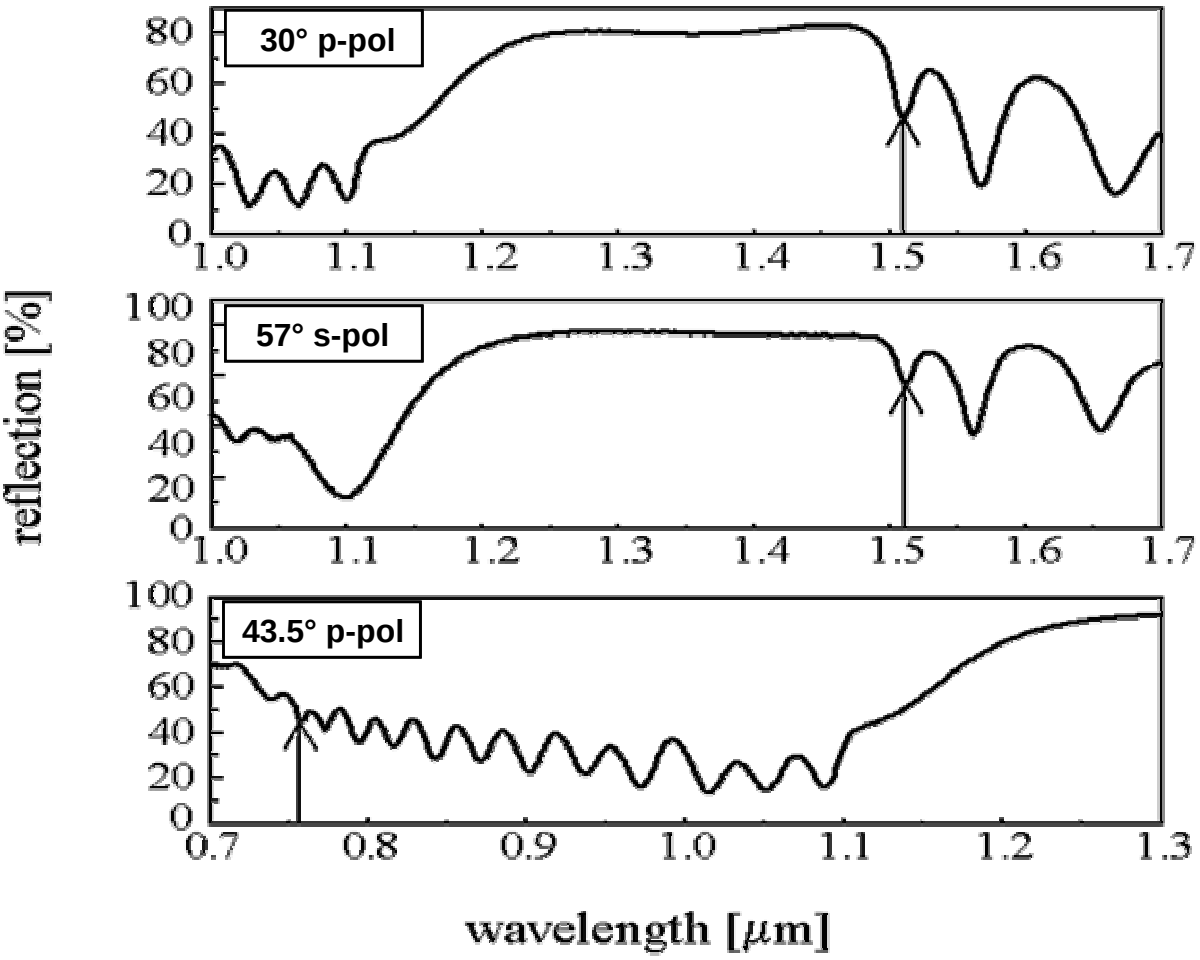

Fig. 2.2. Experimental reflection spectral analysis. (a) Reflection spectra for p-polarized light incident at 30 degrees. (b) Reflection spectra for s-polarized light incident at 57 degrees. (c) Spectrum of p-polarized light around the SH wavelength for an incident angle of 43.5 degrees; the 2nd order band gap for p-polarization is the largest peak on the left side. The vertical arrows indicate the tuning of the fundamental (1510nm) and the SH (755nm) wavelengths.

2.4 Experimental results

The experimental SHG was obtained using the set-up shown in fig. 2.3. The laser system consisted of an amplified Ti-Zaffire laser that pumped a parametric amplifier. The outgoing beam provided 2ps-long pulses at 1 kHz repetition rate, with

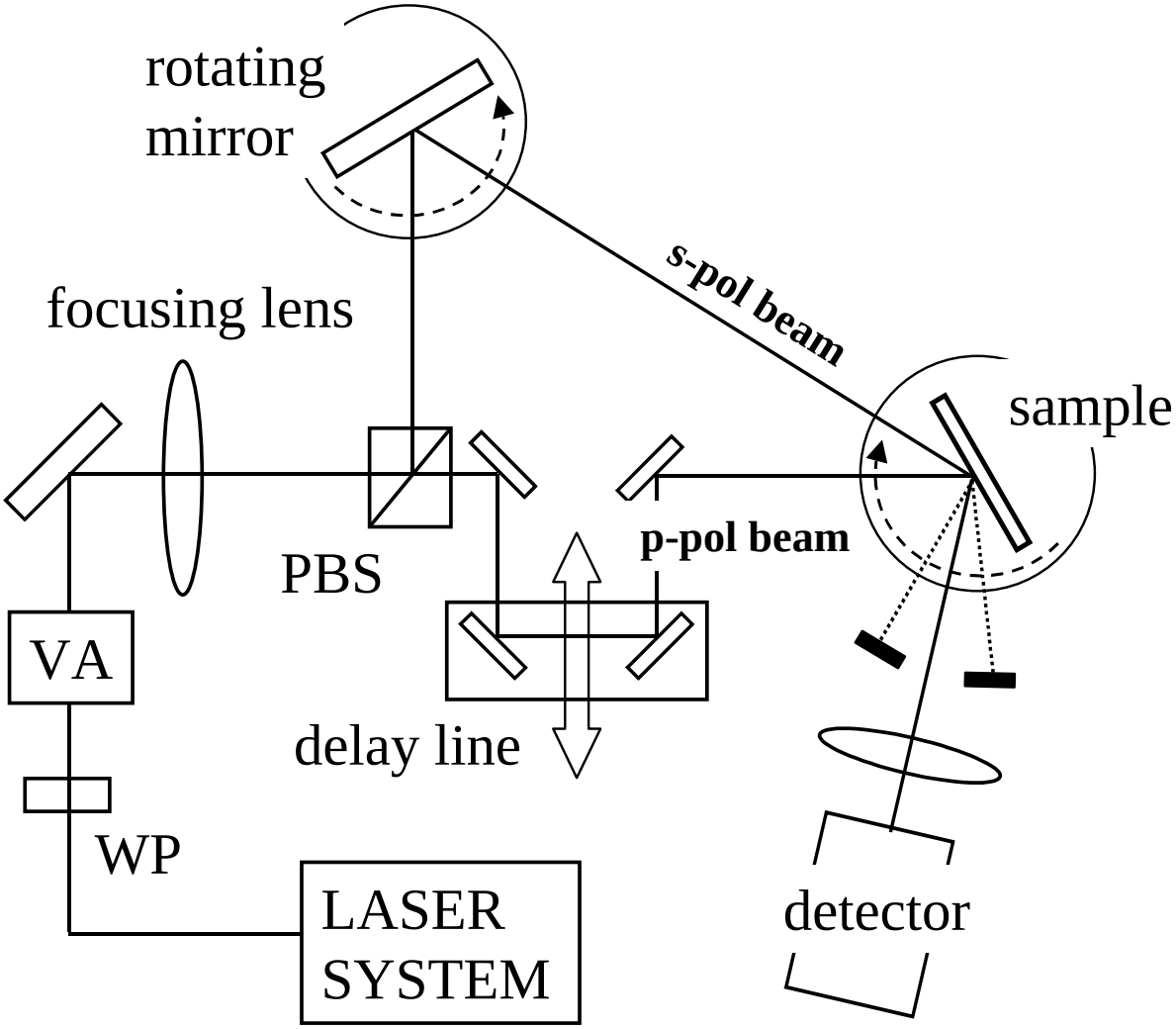

Fig. 2.3. Layout of the experimental set-up. The SH signal was detected by a Si detector (response time about 2ns) connected to an oscilloscope with 500MHz bandwidth.

energy of about 25μJ. A wave-plate (WP) rotated the polarization to obtain, after the polarizing beam splitter (PBS), two cross-polarized beams whose intensities were controlled by the variable attenuator (VA). Both beams were focused on the sample by the same lens (focal length 500mm) down to 180 μm-wide spot-sizes. The two cross polarized beams were sent to the sample with a relative angle of 27 degrees. Their energies were varied up to a maximum of 4.5μJ for each beam, corresponding to a peak intensity of approximately 9GW/cm^2. In our conditions, the PBG acts like a resonant cavity; thus the SH is generated in both forward and backward directions. According to our theoretical model[6], the conversion efficiency ($\eta = I_{SH} / I_{pump}$) in non-depleted pump regime can be written as:

$$\eta^{(+,-)} = \frac{8\pi^2 \left| d_{eff}^{(+,-)} \right|^2 L^2 I_{pump}}{\varepsilon_0 c \lambda^2 n_{eff}^{(\omega,p)} n_{eff}^{(\omega,s)} n_{eff}^{(2\omega,p)}} \qquad (2.2)$$

where, λ is the pump wavelength in vacuum, (+,-) stand for forward and backward directions and $d_{eff}^{(+,-)}$ is the effective coupling coefficient containing the information on the fields overlap inside the structure, as described in Ref. 6. We note that Eq. (2.2) is formally equivalent to the equation that describes a phase-matched bulk medium, where the refractive index and the nonlinear coupling coefficient are replaced by effective quantities. Only the reflected SH was experimentally measured because of the strong absorption present in the GaAs substrate at the SH wavelength. Fig. 2.4 shows the measured reflected SH peak power versus the fundamental beam power. The experimental points are well fitted by a 2nd order polynomial function; this means that the process followed the theory of SHG in the non-depleted pump approximation.

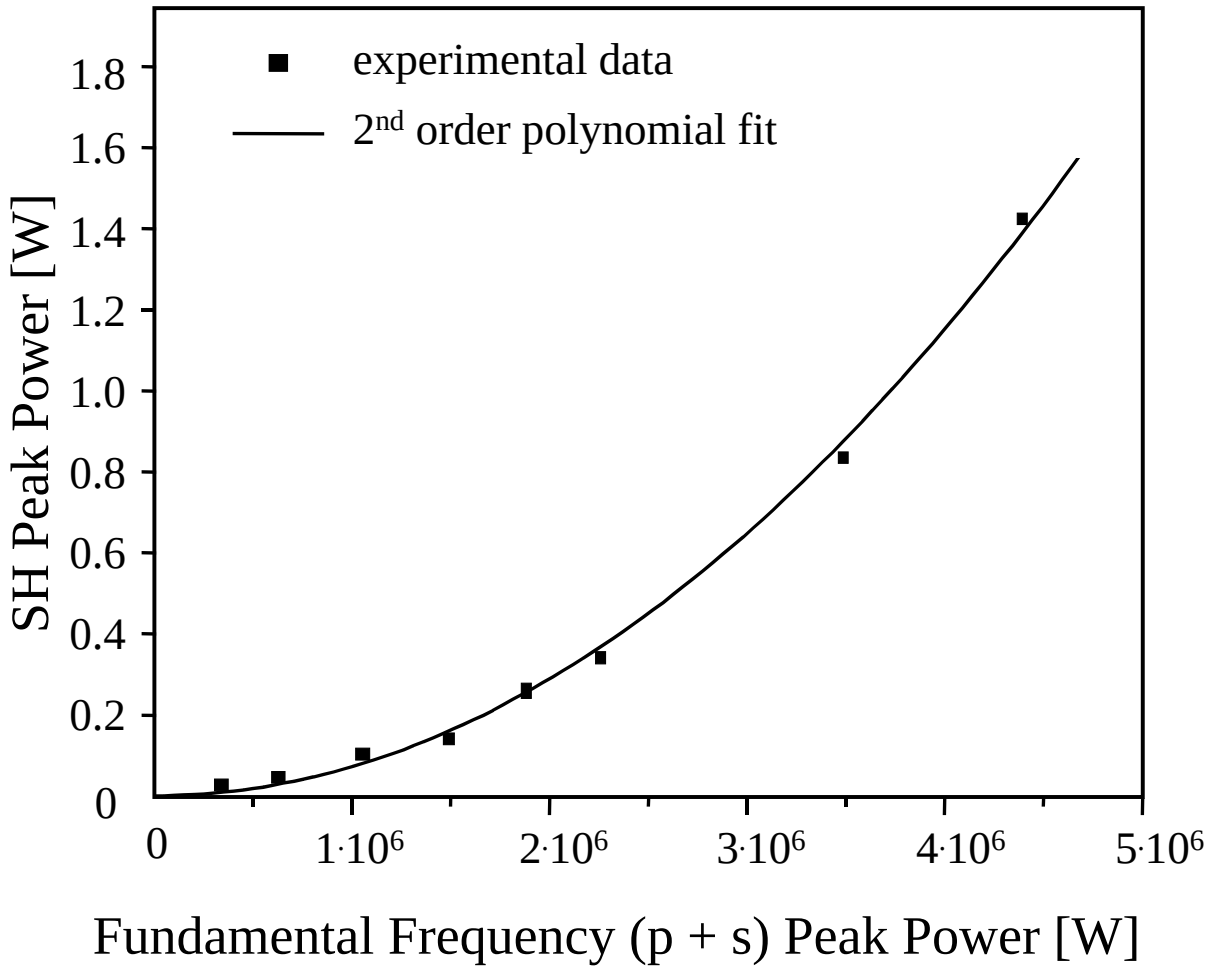

Fig. 2.4. Measured SH peak power Vs total fundamental (p + s) beam power (dots). The solid line represents the second order polynomial fit function needed to calculate the process efficiency.

The measured conversion efficiency corresponding to the maximum fundamental beam intensity was $\eta_{PBG}^{(-)} = (5.6 \pm 0.1) \times 10^{-7}$. The effective nonlinearity shown by the sample was then calculated by comparing this result with the one obtained by a reference nonlinear crystal, operating in transmission, under the same conditions of incident angles and fundamental beam intensity. For this calibration a crystal known

in literature with the acronym DAST[9] was used. The crystal was 1.5mm long, with d_{eff} =(15±3) pm/V for SHG at 1530nm[10]. The measured conversion efficiency was $\eta_D^{(+)} = (3.4 \pm 0.1) \times 10^{-2}$. Substituting the experimental data and the refractive indices for DAST[10] and for the sample[1] in Eq. (2.2), we obtain by comparison:

$$d_{eff}^{(PBG,-)} = \frac{d_{eff}^{(DAST)}}{L_{PBG}} \sqrt{\frac{\left(n_{eff}^{(\omega,p)} n_{eff}^{(\omega,s)} n_{eff}^{(2\omega,p)} \eta^{(-)}\right)_{PBG}}{\left(n^{(\omega,p)} n^{(\omega,s)} n^{(2\omega,p)} \eta^{(+)}\right)_{DAST}}} . \qquad (2.3)$$

Thus, the stratified structure showed an effective nonlinear coefficient $d_{eff}^{(-)}$=(52±12) pm/V.

Angular measurements of the SHG have been performed keeping the relative angle between the incident beams constant to 27 degrees, and by varying the sample orientation. Fig. 2.5 shows the generated power versus the angle between the sample normal and the fundamental p-polarized directions. The solid line represents the theoretical predictions[6]: the model developed for monochromatic plane waves is in qualitative agreement with the experimental data . Note that, in spite of what occurs in bulk media, the SH signal is generated in a broad angular range. The inset of fig. 2.5 shows Bloch diagrams calculated for the fundamental and SH fields. Since the structure is embedded in air, there is a limit on the photonic-crystal modes that can be excited from outside. The dashed line sets the maximum value for the k_y component corresponding to a 90 degree external angle. PM conditions are almost fulfilled for any angle above the gap region. The presence of two peaks in the experimental angular emission is related to enhancement effects that are typical of structure of finite length. The main peak is obtained when the

overlap between the two pump fields is maximized and perfect PM is achieved (30 degrees). The second peak at 28 degrees corresponds to band edge tuning for the SH. The strong SH field localization maintains the efficiency of the process, although the pump fields are slightly off resonance.

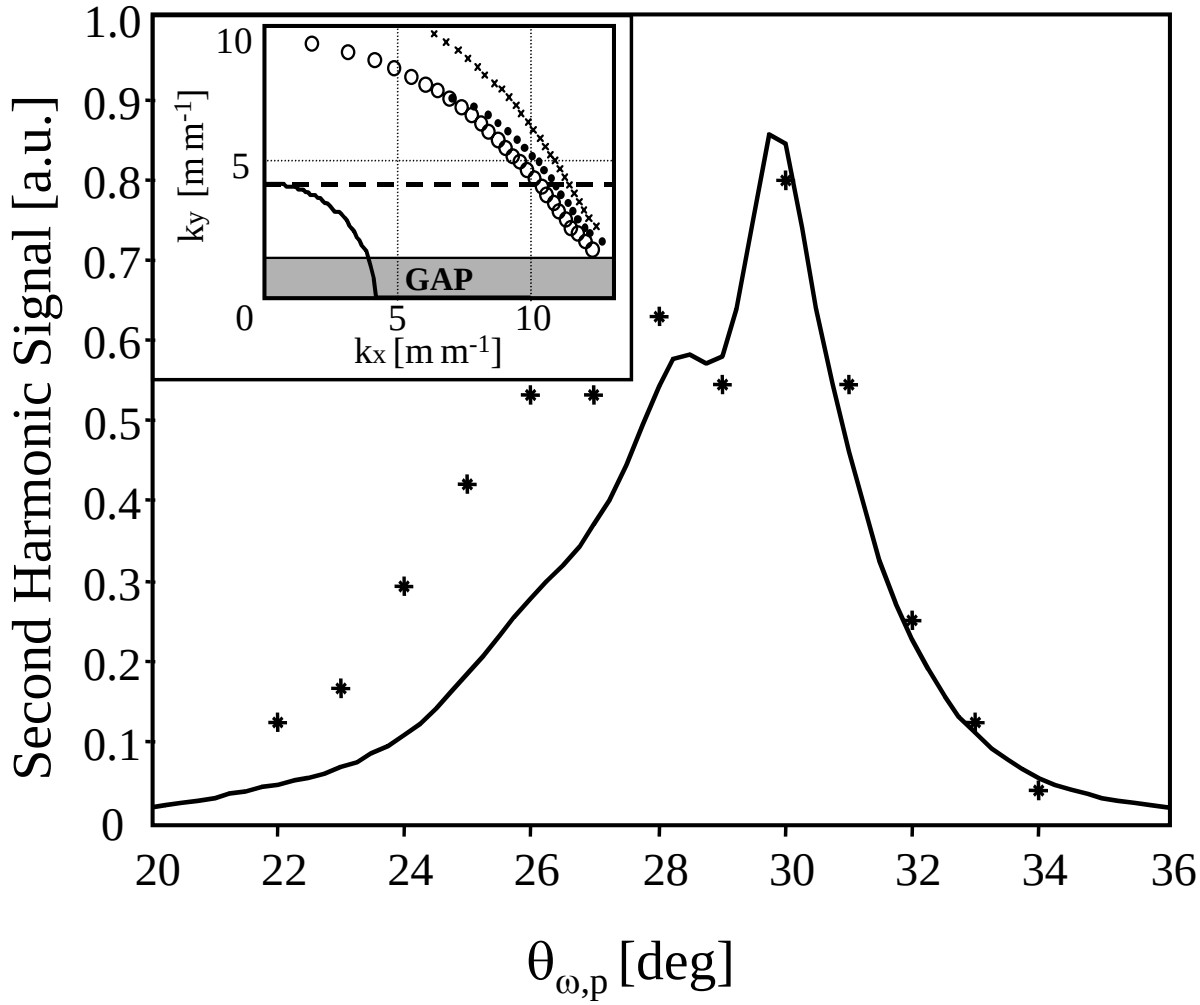

Fig. 2.5. Experimental (*) and theoretical (solid line) angular dependence of the generated p-polarized SH signal. The horizontal axis refers to the fundamental p-polarized beam incidence angle. The angle under which the SH is generated is varying fulfilling the relation 2.b. Inset. Bloch equifrequency curves calculated at the fundamental (circles: p-pol, crosses: s-pol) and at p-pol second harmonic (dots, scaled by a 2 factor) frequencies. The solid-line circle represents the relation $k_x^2+k_y^2=\omega^2/c^2$ for the incident field. Photonic crystal modes can be excited with a k_y value between the dashed line and the gap area.

References

1. M. Centini, C. Sibilia, M. Scalora, G. D'Aguanno, M. Bertolotti, M. J. Bloemer, C. M. Bowden and I. Nefedov, Phys. Rev. E 60, 4891 (1999)
2. G. D'Aguanno, M. Centini, C. Sibilia, M. Bertolotti, M. Scalora, M. J. Bloemer, C. M. Bowden, Opt. Lett. 24, 1663 (1999)
3. Y. Dumeige, P. Vidakovic, S. Sauvage, I. Sagnes, J. A. Levenson, C. Sibilia, M. Centini, G. D'Aguanno and M. Scalora, Appl. Phys. Lett. 78, 3021 (2001)
4. T. V. Dolgova, A. I. Maidykovski, M. G. Martemyanov, A. A. Fedyanin, O. A. Aktsipetrov, G. Marowsky, V. A. Yakovlev, G. Mattei, Appl. Phys. Lett. 81, 2725 (2002)
5. Y. Dumeige, I. Sagnes, P. Monnier, P. Vidakovic, I. Abram, C. Mériadec and A. Levenson, Phys. Rev. Lett. 89, 043901 (2002)
6. G. D'Aguanno, M. Centini, M. Scalora, C. Sibilia, M. Bertolotti, M. J. Bloemer, C. M. Bowden, J. Opt. Soc. Am. B 19, 2111 (2002)
7. A. Fiore, V. Berger, E. Rosencher, P. Bravetti, J. Nagle, Nature 391, 463 (1998)
8. J.M. Dallesasse, N. Holonyak, Jr., A.R. Sugg, T.A. Richard and N. El-Zein, Appl. Phys. Lett. 57, 2844 (1990)
9. F. Pan, G. Knopfle, Ch. Bosshard, S. Follonier, R. Spreiter, M. S. Wong, P. Gunter, Appl. Phys. Lett. 69, 13 (1996)
10. U. Meier, M. Bosch, Ch. Bosshard, F. Pan, P. Gunter, J. Appl. Phys. 83, 3486 (1998)

PART II:

All-Optical Switching in $\chi^{(2)}$ Fabry-Perot Resonator

Chapter 3

Efficiency enhancement by using switching resonant cavities

3.1 Introduction

We have seen in the previous chapters new configurations of all-optical circuits and how integrate them using more efficient composite materials. However it was clear from the experiments that high intensities were necessary to work with such devices. This is clearly a limiting factor for real applications in photonic circuits. Just to give some numbers for comparison, the needed intensity to switch a proposed logic gate is of the order of 10^7-10^9 W/cm^2. Nonlinear processes within optical fibers (such as stimulated Brillouin and Raman scatterings, self-phase modulation through Kerr nonlinearity, etc...) can occur typically at the same intensities necessary to obtain parametric frequency conversion in $\chi^{(2)}$ nonlinearities. The question is now: what might be an allowed intensity level for light propagating an interacting within an optical fiber? Considering a next-future telecommunication system working at 40 Gb/s, with 100 fs pulses at an average power of 1 mW within a single mode fiber (the core would reasonably be as large as 4 μm), the peak intensity per pulse is of the order of 10^6 W/cm^2. Thus, an improving of the efficiency of proposed devices must be studied in order to decrease the switching thresholds of at least 1 order of magnitude.

This was investigated by adopting $\chi^{(2)}$ Fabry-Perot resonant cavities, for which the switching process, from transmission to reflection states, is driven by phase modulation phenomena instead of complete depletion of the beams due to high-efficiency amplitude conversion phenomena. Moreover the cavity feed-back increases the interaction length, allowing consequently a strong increasing of the nonlinear process efficiency (here nonlinear phase modulation), factor that strongly decreases the needed intensities to reach the switching threshold.

All-optical switching and bistability in Fabry-Perot cavities were first proposed in the early 1960s[1] although the first experimental observations occurred between 1978 and 1983. In these investigations Fabry–Perot cavities filled with materials whose refractive indices could be modulated by the light intensity were considered. As a result the light itself suffered phase modulation, inducing switching of the resonance conditions of the resonators. Many different kinds of resonators have been proposed, both in bulk materials[1] and in optical fiber[2–5], that can switch from transmission to reflection regimes by using the nonlinear response of third-order nonlinear materials. These materials offer the possibility of switching light passing through them because their refractive index depends on light intensity. In the early 1990s De Salvo *et al.* demonstrated the possibility of achieving phase modulation of light by using second-order nonlinear optical processes[6–8]. This nonlinearity seems to be more attractive than the third-order one because it is coherent with the inducing light (although Fazio *et al.* demonstrated that even in this case a time-delayed response is possible[9]). Second-order nonlinearity has been largely applied to all-optical switching both in

bulk materials[10,11] and in waveguide geometries[12]. The possibility of achieving optical bistability in resonant cavities filled with second-order nonlinear optical materials as proposed for the first time by Lugiato *et al*.[13]. In 1995 Lefort and Barthelemy proposed[14] a resonant cavity that was able to switch from transmission to reflection. Along the same line Sibilia *et al.*[15] investigated the influence of the field phase modulations on second-harmonic generation inside a ring cavity and consequently its stability. Recently Cojocaru *et al.*[16] investigated the application of Fabry–Perot micro-resonators as active nonlinear mirrors for optical time division multiplexing and demultiplexing.

Following this line, in this chapter I focused attention on the possibility of achieving bistability from Fabry–Perot microcavities and moreover of switching ultralow-intensity light signals, and not on the parallel operation of the devices which somehow was already introduced and demonstrated in the first chapter for the logic circuits. In the proposed configuration, a ultra-low intensity *signal beam* is switched (for example from transmission to reflection) by a second control beam, at higher intensity, called *pump beam* here. The pump beam interacts inside the nonlinear material with the signal beam, inducing parametric down-conversion and eventually phase modulation. To make the input process phase independent[17], three waves coupling (in particular type-II parametric amplification) is considered, where just one of the two fundamental beams and second harmonic are injected at the input, forcing the third beam, still at the fundamental frequency, to be generated inside the cavity.

3.2 Theory

The working scheme for the device is a plane-mirror Fabry–Perot resonator filled with a nonlinear medium as shown in Fig. 3.1, where 1–4 refer to different points in the forward and backward directions inside the resonator. Focusing for the moment on the three fields A_i inside the cavity, the internal boundary conditions can be written as

$$A_i(2) = r_i \cdot A_i(1)$$
$$A_i(4) = r_i \cdot A_i(3) \qquad (3.1)$$

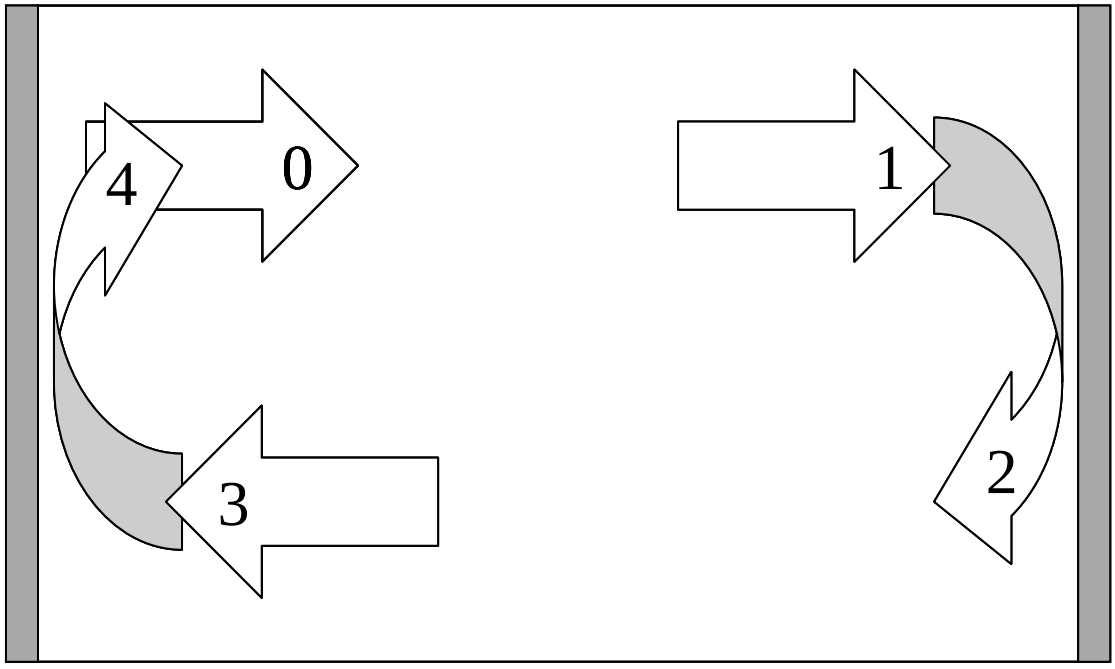

Fig. 3.1. Scheme of light paths inside the Fabry–Perot cavity. 0, input internal interface for the forward wave; 1, output internal interface for the forward wave; 2, 3, similarly output and input interfaces, respectively, for the backward wave, 4, undergoing a complete round trip and overlapping the external beam at position 0; ε, injection from outside.

where the index i = 1, 2, 3 are the three interacting fields. At the same time the internal fields must satisfy propagation conditions in both the forward (i.e., from 0 position to 1) and the backward (i.e., from position 2 to 3) directions:

$$\begin{aligned} A_i(1) &= A_i(0)\cdot f_i\left[A_1(0), A_2(0), A_3(0)\right]\cdot \exp(-ik_i L) \\ A_i(3) &= A_i(2)\cdot f_i\left[A_1(2), A_2(2), A_3(2)\right]\cdot \exp(-ik_i L) \end{aligned} \tag{3.2}$$

Here the f_i functions represent the nonlinear variation of the ith field during its propagation through the crystal, while the exponential term is the phase accumulated in one cavity round-trip. Finally a steady-state condition must be introduced to satisfy the cavity completely:

$$A_i(4) = A_i(0) + E_i^{ext} \ , \tag{3.3}$$

where $t_i E_i^{\text{ext}}$ is the external seed entering the cavity and t_i is the transmission coefficients of the input interface.

The nonlinear variation f_i is due to the parametric interaction between the three fields, which is described by the following well-known equations:

$$\begin{cases} \dfrac{\partial A_1}{\partial z} = -\beta_\omega A_1 - i\cdot\Gamma_1\cdot A_2^* A_3\cdot\exp(-i\Delta k L) \\ \dfrac{\partial A_2}{\partial z} = -\beta_\omega A_2 - i\cdot\Gamma_2\cdot A_1^* A_3\cdot\exp(-i\Delta k L) \\ \dfrac{\partial A_3}{\partial z} = -\beta_{2\omega} A_3 - i\cdot\Gamma_3\cdot A_1 A_2\cdot\exp(i\Delta k L) \end{cases} \tag{3.4}$$

where $\beta_{\omega(2\omega)}$ is the absorption coefficient for the field at frequency $\omega(2\omega)$, $\Gamma_i = \dfrac{8\pi\cdot\omega_i}{n_i(\omega_i)}\cdot d_{eff}$ is the nonlinear coupling coefficients, and ΔK is the phase-

matching of the parametric process. Equations (3.4) can be simplified by using the new internal fields α_i, given by

$$\begin{cases} \alpha_1 = -i \cdot \sqrt{\Gamma_2 \cdot \Gamma_3} \cdot A_1 \cdot \exp(\beta_\omega z) \\ \alpha_2 = -i \cdot \sqrt{\Gamma_1 \cdot \Gamma_3} \cdot A_2 \cdot \exp(\beta_\omega z) \\ \alpha_3 = -i \cdot \sqrt{\Gamma_1 \cdot \Gamma_2} \cdot A_3 \cdot \exp(\beta_{2\omega} z) \end{cases} \tag{3.5}$$

becoming

$$\begin{cases} \dfrac{\partial \alpha_1}{\partial z} = -\alpha_2^* \alpha_3 \cdot \exp(\gamma_{12} z) \\ \dfrac{\partial \alpha_2}{\partial z} = -\alpha_1^* \alpha_3 \cdot \exp(\gamma_{12} z) \\ \dfrac{\partial \alpha_3}{\partial z} = \alpha_1 \alpha_2 \cdot \exp(\gamma_3 z) \end{cases} \tag{3.6}$$

where

$$\begin{cases} \gamma_{12} = -(\beta_{2\omega} + i\Delta K) \\ \gamma_3 = -(2 \cdot \beta_\omega - \beta_{2\omega} - i\Delta K) \end{cases} \tag{3.7}$$

Note that boundary conditions 1–3 remain valid for the new fields α_i with appropriate reflection/transmission coefficients.

Equation (3.6) can be solved by using the Taylor series of the interacting fields up to the fourth terms:

$$\alpha_i(z) = \left(\alpha_i(0) + \left.\frac{\partial \alpha_i}{\partial z}\right|_{(0)} \cdot z + \left.\frac{\partial^2 \alpha_i}{\partial z^2}\right|_{(0)} \cdot \frac{z^2}{2} + \left.\frac{\partial^3 \alpha_i}{\partial z^3}\right|_{(0)} \cdot \frac{z^3}{6} \right) \cdot \exp(-ik_i z) + O(4) \tag{3.8}$$

Considering a noncollinear coupling, the generated beam is not expected to resonate inside the cavity because it is produced at a large angle with respect to the

normal incidence of the mirror. Thus the cavity will be efficient only for the injected fundamental and injected second-harmonic fields.

3.3 Lossless medium and perfect phase matching

Let us consider a lossless medium and a perfect phase-matched interaction ($\gamma_{12}=\gamma_3=0$). Equations (3.6) become

$$\begin{cases} \dfrac{\partial \alpha_1}{\partial z} = -\alpha_2^{*}\alpha_3 \\ \dfrac{\partial \alpha_2}{\partial z} = -\alpha_1^{*}\alpha_3 \\ \dfrac{\partial \alpha_3}{\partial z} = \alpha_1\alpha_2 \end{cases}. \qquad (3.9)$$

By progressive derivations of Eqs. (3.9), it is possible to calculate the first-, second-, and third-order derivative of the fields at the initial position, 0. Once more, it must be stressed that field α_2 does not resonate and is not injected. This means that $\alpha_2(0)=0$ always and consequently all the derivatives at the boundary become

$$\begin{aligned} &\left.\frac{\partial \alpha_1}{\partial z}\right|_{(0)} = 0; \quad \left.\frac{\partial^2 \alpha_1}{\partial z^2}\right|_{(0)} = \alpha_1(0)\cdot|\alpha_3(0)|^2; \quad \left.\frac{\partial^3 \alpha_1}{\partial z^3}\right|_{(0)} = 0 \\ &\left.\frac{\partial \alpha_2}{\partial z}\right|_{(0)} = -\alpha_1(0)\cdot\alpha_3^{*}(0); \quad \left.\frac{\partial^2 \alpha_2}{\partial z^2}\right|_{(0)} = 0; \quad \left.\frac{\partial^3 \alpha_2}{\partial z^3}\right|_{(0)} = \alpha_1(0)\cdot\alpha_3^{*}(0)\cdot\left(|\alpha_1(0)|^2 - |\alpha_3(0)|^2\right) \qquad (3.10) \\ &\left.\frac{\partial \alpha_3}{\partial z}\right|_{(0)} = 0; \quad \left.\frac{\partial^2 \alpha_3}{\partial z^2}\right|_{(0)} = -\alpha_3(0)\cdot|\alpha_1(0)|^2; \quad \left.\frac{\partial^3 \alpha_{1i}}{\partial z^3}\right|_{(0)} = 0 \end{aligned}$$

The previous condition, $\alpha_2(0)=0$, forces the system toward a down-conversion process, for which α_1 is always amplified {in fact $[\partial^2\alpha_1/\partial z^2]>0$} and α_3 is always depleted {i.e., $[\partial^2\alpha_3/\partial z^2]<0$}.

By combining the propagation terms in Eq. (3.8) with the previous derivatives [Eqs. (3.10)], each field varies according to

$$\alpha_1(z) = \alpha_1(0)\cdot\left(1+\left|\alpha_3(0)\right|^2\cdot\frac{z^2}{2}\right)\cdot\exp(-ik_1 z)$$
$$\alpha_2(z) = -\alpha_1(0)\cdot\alpha_3^*(0)\cdot\left[z+\left(\left|\alpha_3(0)\right|^2-\left|\alpha_1(0)\right|^2\right)\cdot\frac{z^3}{6}\right]\cdot\exp(-ik_2 z) \qquad (3.11)$$
$$\alpha_3(z) = \alpha_3(0)\cdot\left(1-\left|\alpha_1(0)\right|^2\cdot\frac{z^2}{2}\right)\cdot\exp(-ik_3 z)$$

A comparison of Eqs. (3.11) with Eqs. (3.2) directly gives the nonlinear terms f_i expected when solving the whole resonator. Thus, by using these propagation conditions together with Eqs. (3.1) and (3.3), the evolution of the internal α_i fields can be derived. Note here the importance of the steady-state conditions [Eqs. (3.3)] that are reported here for the internal α_i fields:

$$\alpha_i(0) = \alpha_i(4) + \mathcal{E}_i \qquad (3.12)$$

where ε_i are the amplitudes of the driving fields injected from outside in the cavity. They are different from zero only for i=1 and i=3:

$$\mathcal{E}_1 = -i\cdot\sqrt{\Gamma_2\cdot\Gamma_3}\cdot t_1\cdot Eext_1$$
$$\mathcal{E}_2 = 0 \qquad (3.13)$$
$$\mathcal{E}_3 = -i\cdot\sqrt{\Gamma_1\cdot\Gamma_2}\cdot t_3\cdot Eext_3$$

where r_i and t_i are the reflection and the transmission coefficients of the mirrors respect to the i-th field frequency. Finally the resonating fields vary according to

$$\alpha_1(0) = \frac{\mathcal{E}_1}{1-r_1^2\cdot\exp(-2ik_1 L)\cdot F_1\left(\left|\alpha_1(0)\right|^2,\left|\alpha_3(0)\right|^2\right)} \qquad (3.14)$$

$$\alpha_3(0) = \frac{\mathcal{E}_3}{1 - r_3^2 \cdot \exp(-2ik_3 L) \cdot F_3\left(|\alpha_1(0)|^2, |\alpha_3(0)|^2\right)}, \tag{3.15}$$

where

$$\begin{aligned} F_1\left(|\alpha_1(0)|^2, |\alpha_3(0)|^2\right) &= \left(1 + |\alpha_3(0)|^2 \frac{L^2}{2}\right)\left[1 + |\alpha_3(0)|^2\left(1 - |\alpha_1(0)|^2 \frac{L^2}{2}\right)^2 r_3^2 \frac{L^2}{2}\right] \\ F_3\left(|\alpha_1(0)|^2, |\alpha_3(0)|^2\right) &= \left(1 - |\alpha_1(0)|^2 \frac{L^2}{2}\right)\left[1 - |\alpha_1(0)|^2\left(1 + |\alpha_3(0)|^2 \frac{L^2}{2}\right)^2 r_1^2 \frac{L^2}{2}\right] \end{aligned}. \tag{3.16}$$

According to Eq.(3.8), the term $|\alpha_1(0)|^2$ in Eq. (3.16a) and the term $|\alpha_3(0)|^2$ in Eq. (3.16b) can be neglected. In this way

$$\begin{aligned} F_1 = F_1\left(|\alpha_3(0)|^2\right) &\cong \left(1 + |\alpha_3(0)|^2 \cdot \frac{L^2}{2}\right) \cdot \left[1 + |\alpha_3(0)|^2 \cdot r_3^2 \cdot \frac{L^2}{2}\right] \\ F_3 = F_3\left(|\alpha_1(0)|^2\right) &\cong \left(1 - |\alpha_1(0)|^2 \cdot \frac{L^2}{2}\right) \cdot \left[1 - |\alpha_1(0)|^2 \cdot r_1^2 \cdot \frac{L^2}{2}\right] \end{aligned} \tag{3.17}$$

Equations (3.14) and (3.15) can be solved graphically by plotting together $|\alpha_1(0)|^2$ Vs $|\alpha_3(0)|^2$ and $|\alpha_3(0)|^2$ Vs $|\alpha_1(0)|^2$.

3.4 Dummy variable method

The active nonlinear mirror is a device whose reflectivity can be controlled and modulated by an external second-harmonic beam. It will be active for a low-intensity beam at a fundamental frequency. Thus the external parameter ε_1 in Eq. (3.14) is constant and represents the injected low-intensity beam at the fundamental frequency. However, the external parameter ε_3 in Eq. (3.15) is not constant and represents the injected high-intensity beam at the second-harmonic frequency: It is

variable because of light control from the mirror behavior. In this way Eq.(3.15) is actually a family of curves for the dummy parameter ε_3, while Eq. (3.14) is a single curve for the constant parameter ε_1. Different geometries of interaction can still be easily solved by using the same method but by changing the dummy variable.

A. Single Curve from Eq. (3.14)

Equation (3.14) has the same mathematical structure as the linear Fabry–Perot resonator with inclusion of the nonlinear factor F_1; thus it strongly depends on the linear tuning, $\Delta\phi_1=k_1L$, of the cavity. When $\Delta\phi_1$ is varied, $|\alpha_1(0)|^2$ Vs $|\alpha_3(0)|^2$ exhibits different behaviors, as shown in Fig. 3.2. When $\Delta\phi_1$ is close to zero, it shows a narrow peak as high as $\frac{|\mathcal{E}_1|^2}{1-\cos^2(2\Delta\phi_1)}$ at $|\alpha_3(0)|^2 = \frac{1+r_3^2+\sqrt{t_3^4+4\frac{r_3^2}{r_1^2}\cdot\cos(2\cdot\Delta\phi_1)}}{r_3^2\cdot L^2}$.

When $\Delta\phi_1$ is increased, both the position and the height of the peak change, moving toward lower values of $|\alpha_3(0)|^2$ until $\Delta\phi_{1max}$ $\arcsin(t_1\sqrt{2})$, a limit value that shows the transit of the peak by $|\alpha_3(0)|^2=0$ (i.e., no amplification is possible). Above $\Delta\phi_{1max}$ the curve monotonically decreases. It is clear below that $\Delta\phi_1<\Delta\phi_{1max}$ is a necessary condition for achieving optical bistability. When $\Delta\phi_1$ goes to zero, $|\alpha_1(0)|^2$ Vs $|\alpha_3(0)|^2$ becomes a Dirac δ, but, as seen below, the amplification is so strong that the model loses validity.

In Fig. 3.2 $|\alpha_1(0)|^2$ Vs $|\alpha_3(0)|^2$ from Eq. (3.14) is shown for three different tuning values of the cavity. At $\Delta\phi_1$=25° the peak (not shown in Fig. 3.2) is at $|\alpha_3(0)|^2$=0 and the whole curve monotonically decreases; from $\Delta\phi_1$=25° toward $\Delta\phi_1$=1°, i.e., toward perfect tuning, there is a pronounced peak in the curve at positions closer to higher second-harmonic intensities.

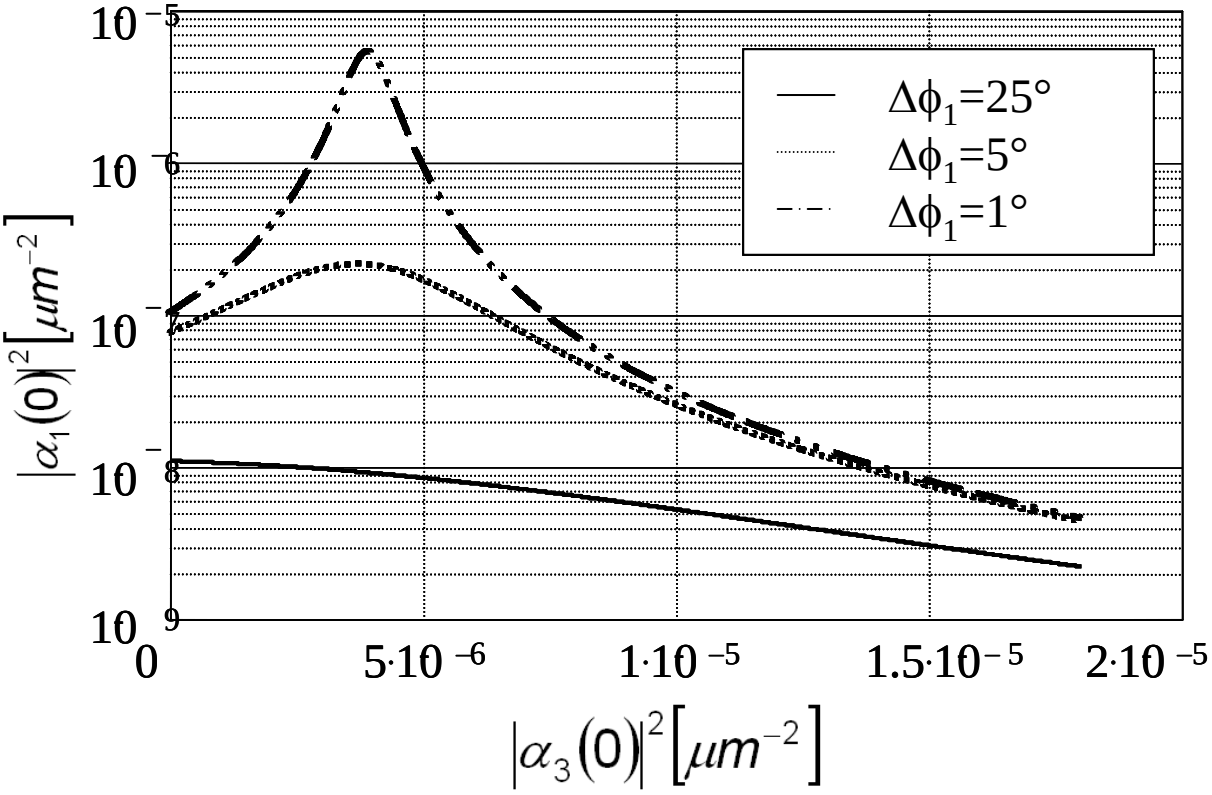

Fig. 3.2. Behavior of the internal mode α_3 at the fundamental frequency as a function of the internal second-harmonic mode just behind the first mirror, i.e., at position 0. The three curves correspond to different cavity mismatches. Note that the peaks of the curves move to the left hand side, increasing the mismatch, even passing the graphic boundary. If this limit is passed, the curve monotonically decreases along the whole intensity range of the second-harmonic internal mode.

B. Family of Curves from Eq. (3.15) for the Dummy Parameter ε_3

Even if the structure is similar, Eq. (3.15) (or better $|\alpha_3(0)|^2$ Vs $|\alpha_1(0)|^2$) behaves differently from Eq. (3.14), since the amplification factor F_3 is different. In particular note that $|\alpha_3(0)|^2$ can attain several extremal points (as many as three) with vanishing prime derivatives in the variable $|\alpha_1(0)|^2$. To visualize these different behaviors, Fig. 3.3 shows $|\alpha_3(0)|^2$ Vs $|\alpha_1(0)|^2$ for four different values of ε_3, the resonance mismatching per round trip of mode 3. If $0<\Delta\phi_3<\arcsin(t_1\sqrt{2})$ (which is the case for $\Delta\phi_3=15°$), the $|\alpha_3(0)|^2$ function monotonically decreases until it reaches a minimum at $|\alpha_1(0)|^2 = \frac{1+r_1^2}{r_1^2 \cdot L^2}$ then it increases to a maximum situated at $|\alpha_1(0)|^2 = \frac{1+r_1^2+\sqrt{t_1^4+4\frac{r_1^2}{r_3^2}\cdot\cos(2\cdot\Delta\phi_3)}}{r_1^2 \cdot L^2}$, followed by one more decreasing region toward the zero value. In this case two extremal points are found here.

If $\arcsin(t_1\sqrt{2})<\Delta\phi_3<(\pi/4)$ (as is the case for $\Delta\phi_3=30°$ shown in Fig. 3.3), the two maxima of $|\alpha_3(0)|^2$ are lower than before and much closer to each other: actually the left-hand-side maximum is shown in the inset and is located at $|\alpha_1(0)|^2 = \frac{1+r_1^2-\sqrt{t_1^4+4\frac{r_1^2}{r_3^2}\cdot\cos(2\cdot\Delta\phi_3)}}{r_1^2 \cdot L^2}$. Thus the whole curve now has three extremal points that move closer and closer, increasing $\Delta\phi_3$.

For $(\pi/4)<\Delta\phi_3<(\pi/2)$ these three extremal points converge toward a flat region, with just one single large maximum at $|\alpha_1(0)|^2 = \frac{1+r_1^2}{r_1^2 \cdot L^2}$ which degenerates in a bell-like curve for $\Delta\phi_3$=90°.

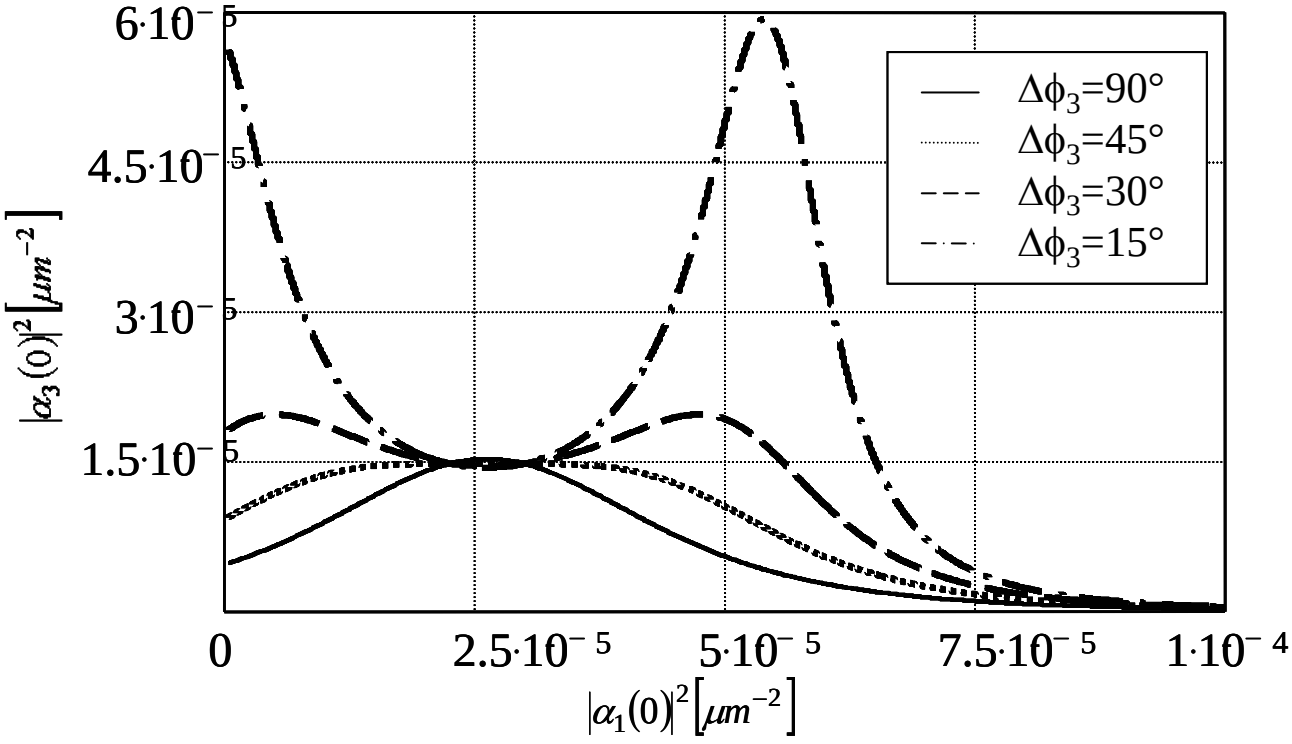

Fig. 3.3. Behavior of the internal mode α_3 at the second-harmonic frequency as a function of the fundamental internal mode α_1 just behind the first mirror, i.e., at position 0. The curves correspond to different cavity mismatches. Note that different trends can be observed, corresponding to just one peak, two peaks, etc.

3.5. Bistable solutions

These different trends in $|\alpha_3(0)|^2$ versus $|\alpha_1(0)|^2$ and $|\alpha_1(0)|^2$ versus $|\alpha_3(0)|^2$ are simultaneously calculated, giving solutions for the whole problem. In particular for each pair, $|\alpha_1(0)|^2$ and $|\alpha_3(0)|^2$, obtained by numerical computation of Eqs. (3.14) and (3.15), one value of $|\varepsilon_3|^2$ can be calculated by

$$\left|\mathcal{E}_3\right|^2 = \left|\alpha_3(0)\right|^2 \cdot \left|1 - r_3^2 \cdot \exp(-2ik_3L) \cdot \left(1 - \left|\alpha_1(0)\right|^2 \cdot \frac{L^2}{2}\right) \cdot \left(1 - \left|\alpha_1(0)\right|^2 \cdot r_1^2 \cdot \frac{L^2}{2}\right)\right|^2 . \quad (3.18)$$

Equation (3.18) can finally be inverted to show how the steady value of $|\alpha_1|^2$, at the input surface called point 0, varies for different values of the external second-harmonic intensity, i.e., the control parameter of the system and of resonator parameters r_1, r_3, L. Note that the optical lengths, L_1 and L_3, that determine the field resonances play the most crucial role: in fact, they give the linear cavity detuning, $\Delta\phi_1$ and $\Delta\phi_3$ (i.e., the difference between k_1L_1 and k_3L_3 from the nearest integer number of π), that affects the complete behavior of the nonlinear resonator. In Fig. 3.4 $|\alpha_3(0)|^2$ Vs $|\alpha_1(0)|^2$ (curves *F*) and $|\alpha_3(0)|^2$ Vs $|\alpha_1(0)|^2$ (single curve S) are shown for cavity parameters $\Delta\phi_1$=0.9° and $\Delta\phi_3$=90°. The F curves differ from one another for different values of the external $\sum_3$ parameter. The F curves have higher values as ε_3 increase. At low ε_3 (dotted *F* line) just one intersection between the F and S curves is present; when ε_3 increases, the F curve (dash + two points) intersects the S curve twice, where indeed the new intersection point is degenerate in the sense that it is formed by two overlapped points that separate the increasing ε_3 (dashed curve). At higher

values of ε_3 a new condition with just two intersections can be found, as shown by the dash-dot curve in Fig. 3.4 (even in this case one of them is degenerate) while, when ε_3 is increased further, just one intersection is possible.

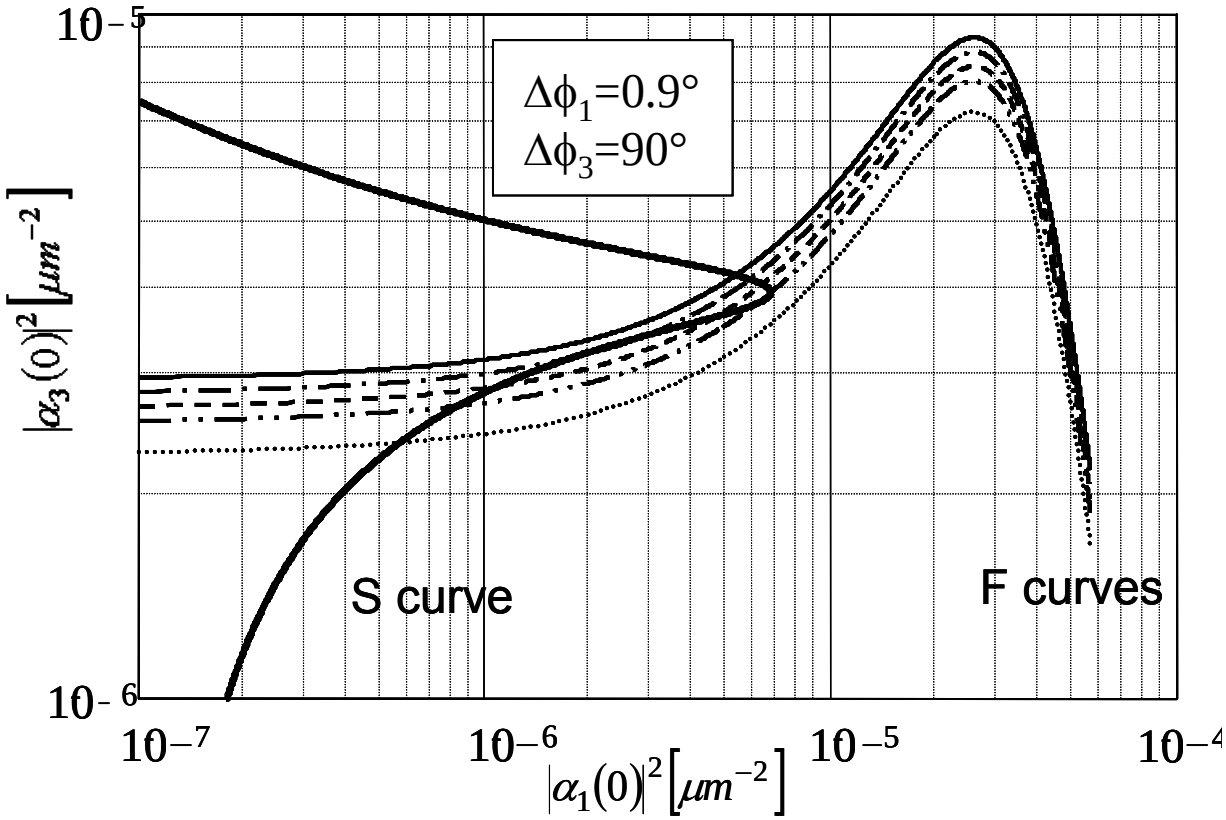

Fig. 3.4. Graphic solution of the cavity performances by plotting the S single curve $|\alpha_1(0)|^2$ versus $|\alpha_3(0)|^2$ from Eq.(14) and the F curve family $|\alpha_3(0)|^2$ versus$|\alpha_1(0)|^2$ from Eq.(15). The F curves differ for dummy parameter ε_3, which represents the external second-harmonic intensity. Intersections between the S curve and the F curves show the cavity solutions: In particular it can be seen that for different values of ε_3 that we have one, two, or three intersections.

In Fig. 3.5 the behavior of $|\alpha_3(0)|^2$ versus $|E_{3ext}|^2$ is shown for the case in Fig. 3.4. When the second-harmonic beam increases, the internal mode is amplified, showing a region between 1.0 and 1.5 MW/cm^2 where a bistable loop can be observed. Note that this loop occurs at quite low intensity for both the amplified fundamental beam (chosen to be as low as a few k W/cm^2 at the input) and the second-harmonic pump beam (this case as high as a few M W/cm^2). These calculations were performed with an effective nonlinearity of 30 pm/V, which is a typical value for semiconductors or organic crystals.

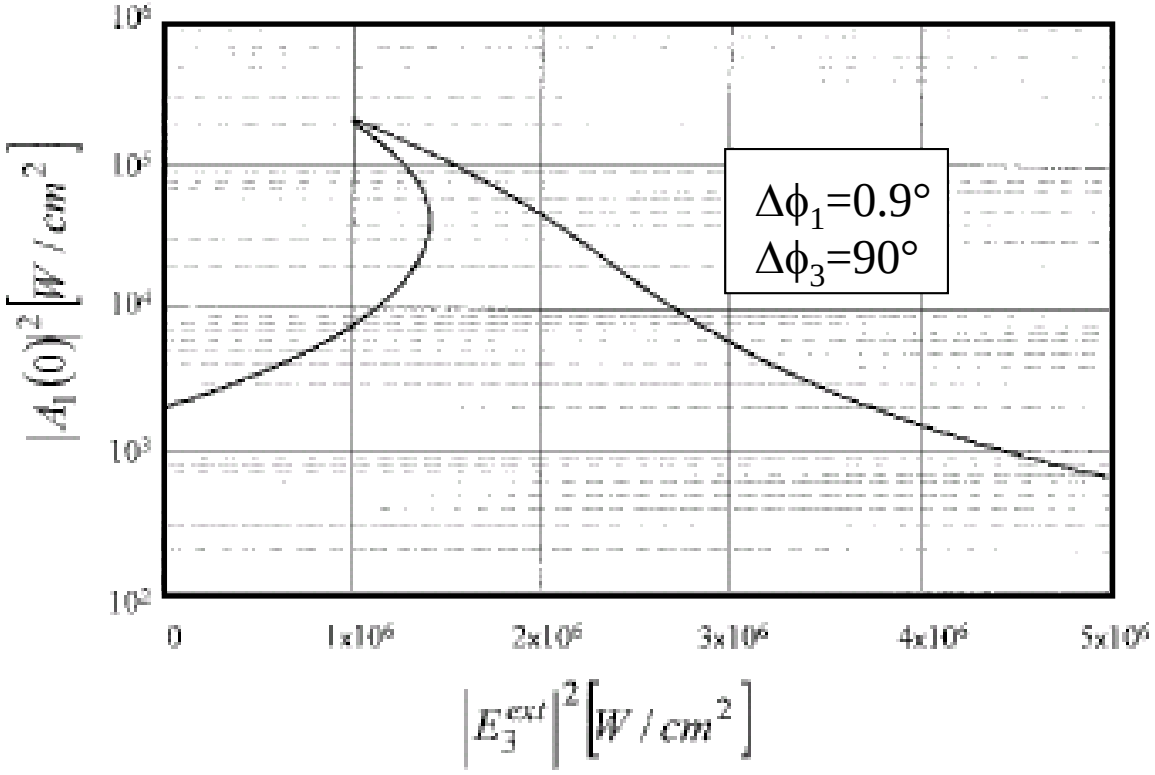

Fig. 3.5. Cavity performances as derived from Fig. 4. In this case the internal intensity of the fundamental frequency at input position 0 is plotted as a function of the external second-harmonic intensity. In the region between 1 and 1.45 MW/cm^2 the cavity accepts three contemporary solutions, typical of bistable behavior.

The amplification and switching of the internal mode α_1 at internal interface 0 reflect themselves in the amplification and switching of the reflected signal beam from the Fabry–Perot active mirror, as shown in Fig. 3.6. In this case the expected jumps are drawn from the lower intensity state to the upper state as well as from the upper to the lower states.

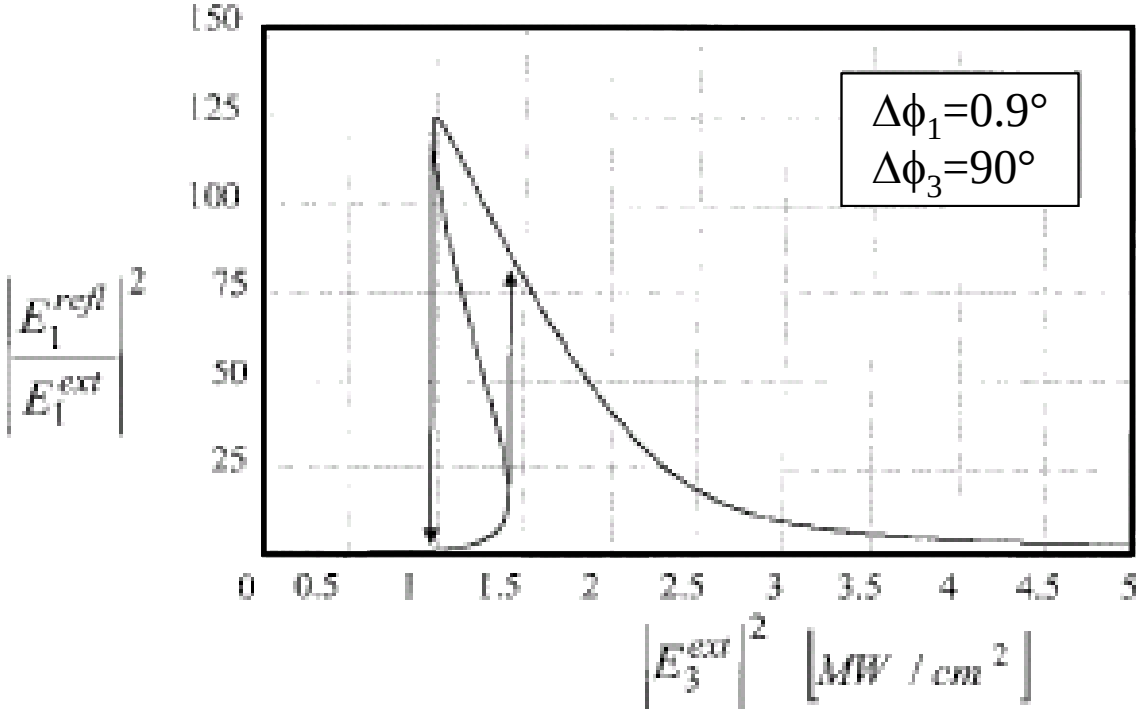

Fig. 3.6. Nonlinear reflection of a low-intensity beam at the fundamental frequency from the Fabry–Perot active mirror driven by a second-harmonic control beam. These results correspond to the behavior of the internal mode described in Figs 3.4 and 3.5. Starting from linear reflection of 1, the signal is amplified 15–20 times, by a control beam as great as 1 MW/cm^2. Above this value the reflected signal beam switches toward a higher reflection of approximately 80–90.

When the cavity characteristics are modified, different loops can be reached. In particular, if the second-harmonic cavity-detuning $\Delta\phi_3$ decreases to 15°, for example, the $|\alpha_3(0)|^2$ versus $|\alpha_1(0)|^2$ curves show different trends, as shown in Fig. 3.7. In this case the F curves monotonically decrease, still showing a region with three intersections, which, however, produces a different trend for the bistable loop (see Fig. 3.8). In this second case bistability occurs at a lower second-harmonic intensity

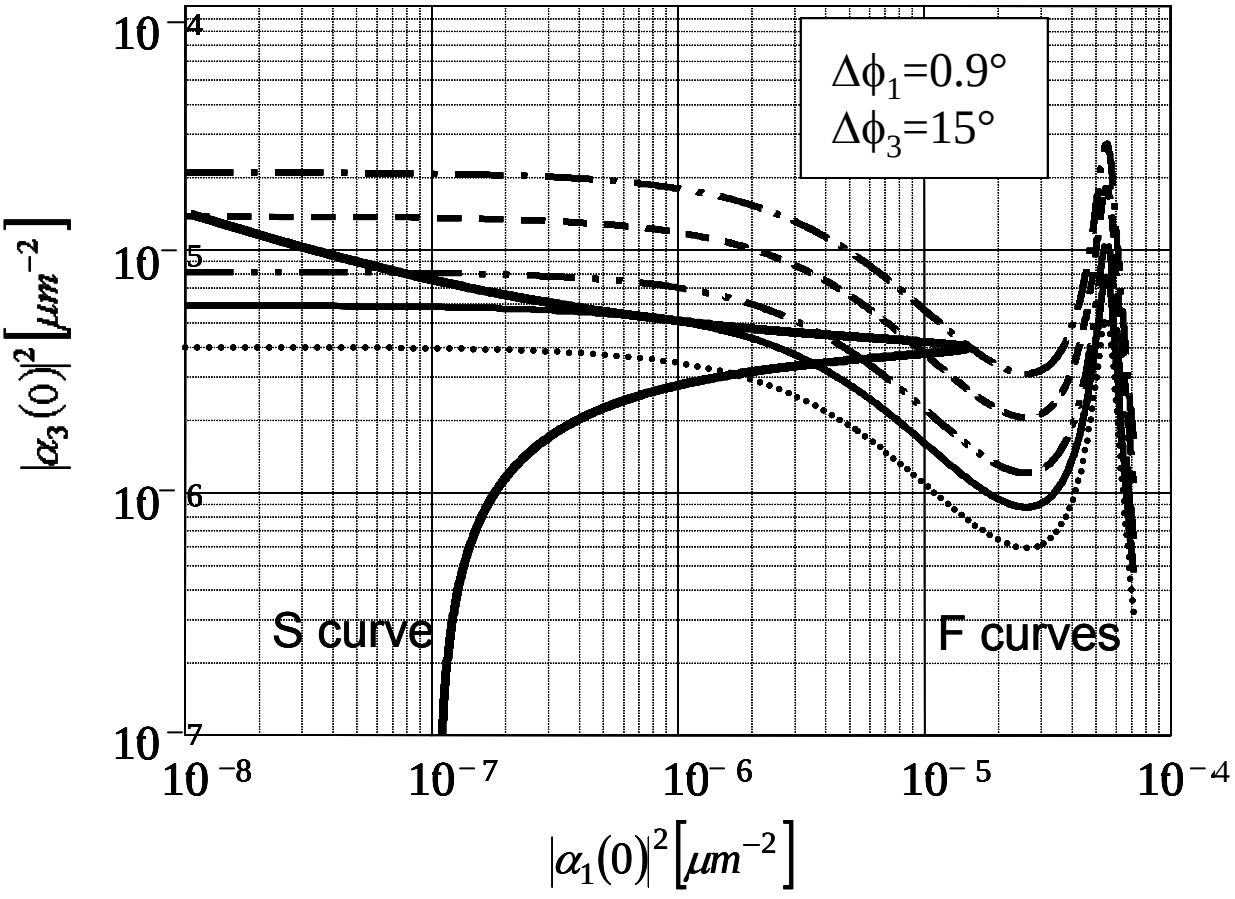

Fig. 3.7. Graphic solution of the cavity performances, as described in Fig. 3.4, for a different mismatch of the second-harmonic cavity. Note that in this case the different behaviors of the F curves now show the trend decreasing, in the region where intersects curve S instead of the trend increasing as in Fig. 3.4. This difference corresponds to a completely different cavity performance, as shown in Fig. 3.8.

(200-400 kW/cm^2). This pump intensity reduction is a result of the higher internal field stored by the cavity for the second-harmonic frequency. Lower detuning $\Delta\phi_3$ induces a higher internal intensity of the second harmonic that drastically reduces the threshold for the bistable loop.

In Fig. 3.9 a comparison of the internal fundamental mode as a function of $\Delta\phi_3$ is shown: for intermediate detuning ($\Delta\phi_3$=30°) no bistable loop can be found, only effective amplification.

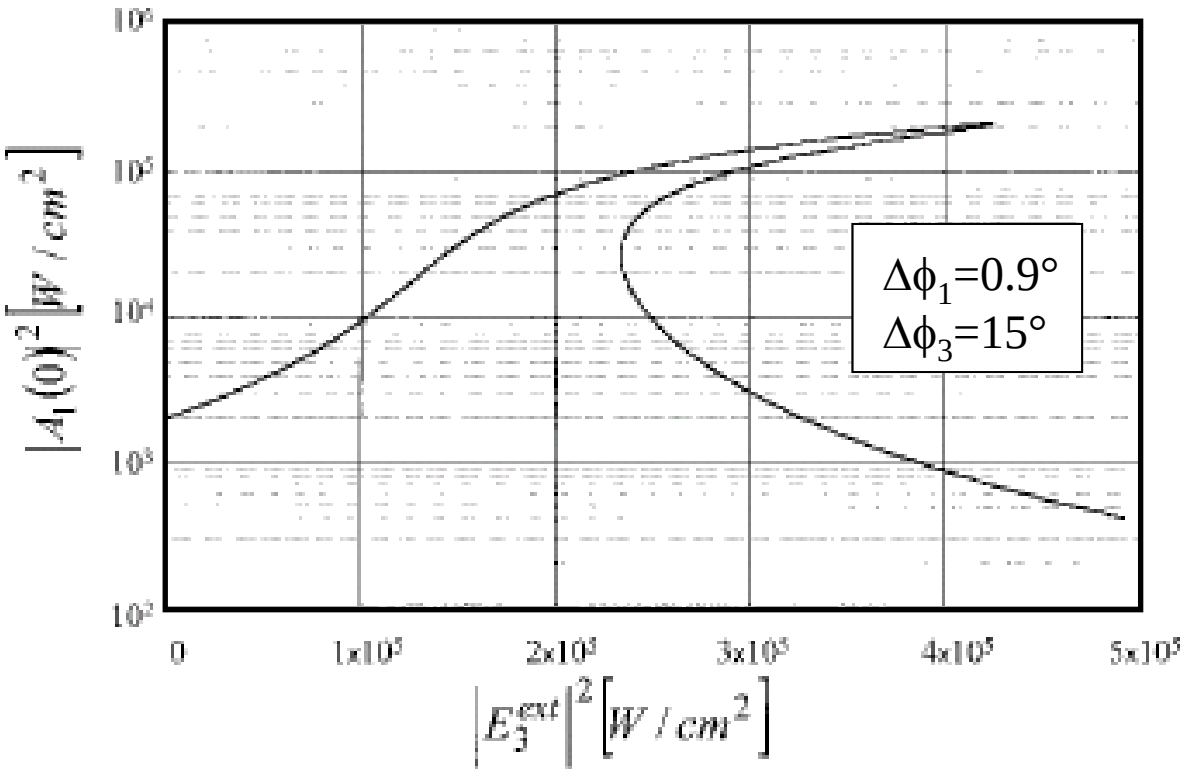

Fig. 3.8. Cavity performances as derived from Fig. 3.7. The internal intensity of the fundamental frequency, plotted as a function of the external second-harmonic intensity, shows a bistable region between 0.24 and 0.42 MW/cm2. Compared with the bistable loop derived in Fig. 3.5, few differences can be identified: The present loop is reversed with respect to the previous one, mainly due to the modal resonances; it occurs at lower power and is larger.

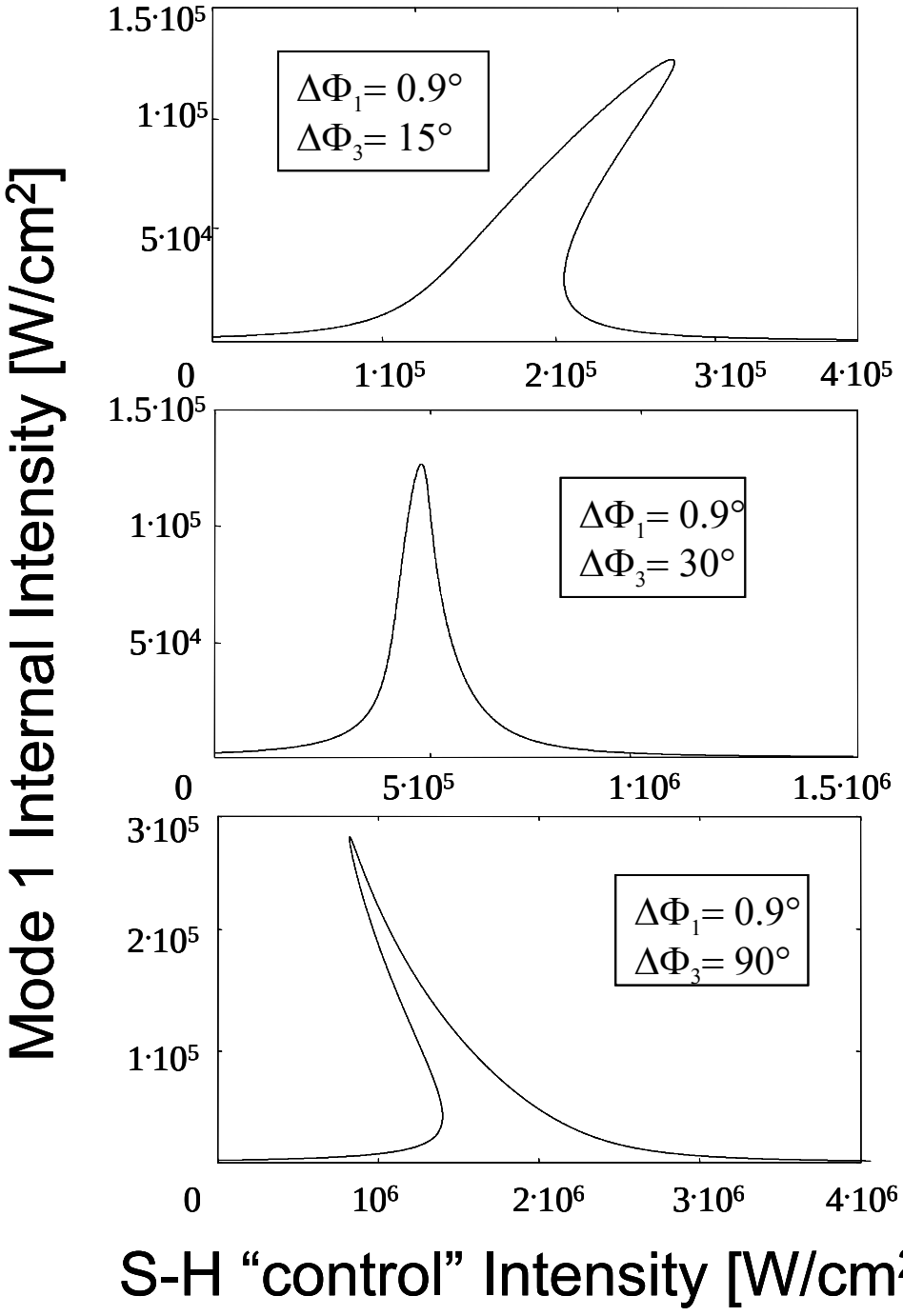

Fig. 3.9. Different cavity performances for three second-harmonic mode mismatches. When the mismatch is low, the bistable loop occurs when the pumping is lower; at a moderate mismatch no loops are present, only efficient amplification; at an elevated mismatch, the loop is reversed and occurs at a higher pump intensity than above. Note that in the last case the loop is folded toward a lower intensity: This characteristic takes into account the low internal intensity of the pump beam that increases cavity switching and, as a consequence, allows the energy stored inside the cavity to be higher.

A. Influence of Phase Matching

Until now, the interaction in perfect phase matching has been analyzed [see Eqs. (3.9)]. This means that all the effects shown above are mainly due to amplitude more that phase modulations. In fact the F_1 and F3 terms described in Eqs. (3.17) are real quantities, which means that during any round trip the internal modes do not suffer phase modulation, only amplification and/or depletion. However, these amplification terms can still modify the resonance conditions described in Eqs. (3.14) and (3.15), giving rise to deformation of the internal mode at the fundamental frequency as a function of the external second-harmonic beam.

Now let us see the influence of a phase mismatch on the parametric process and of linear and nonlinear absorption on the cavity performances.These terms can be taken into account by modifying the third order derivatives in Eqs. (3.10) according to

$$\left.\begin{aligned}\left.\frac{\partial^3\alpha_1}{\partial z^3}\right|_{(0)} &= \left(2\cdot\gamma_{12}+\gamma_{12}^{*}\right)\cdot\alpha_1(0)\cdot\left|\alpha_3(0)\right|^2\\ \left.\frac{\partial^3\alpha_3}{\partial z^3}\right|_{(0)} &= \left(2\cdot\gamma_{3}+\gamma_{12}\right)\cdot\alpha_3(0)\cdot\left|\alpha_1(0)\right|^2\end{aligned}\right. . \tag{3.19}$$

Thus the modal propagation equations [Eqs. (3.11)] inside the resonator become

$$\left.\begin{aligned}\alpha_1(z) &= \alpha_1(0)\cdot\left\{1+\left|\alpha_3(0)\right|^2\cdot\left[\frac{z^2}{2}+\left(2\cdot\gamma_{12}+\gamma_{12}^{*}\right)\cdot\frac{z^3}{6}\right]\right\}\cdot\exp(-i\cdot k_1 z)\\ \alpha_3(z) &= \alpha_3(0)\cdot\left\{1-\left|\alpha_1(0)\right|^2\cdot\left[\frac{z^2}{2}+\left(2\cdot\gamma_{3}+\gamma_{12}\right)\cdot\frac{z^3}{6}\right]\right\}\cdot\exp(-i\cdot k_3 z)\end{aligned}\right. ; \tag{3.20}$$

where the terms Λ_1 and Λ_2 are written as

$$\begin{aligned}\Lambda_1 &= \frac{L^2}{2} + \left(2\cdot\gamma_{12} + \gamma_{12}^{*}\right)\cdot\frac{L^3}{6} \\ \Lambda_3 &= \frac{L^2}{2} + \left(2\cdot\gamma_3 + \gamma_{12}\right)\cdot\frac{L^3}{6}\end{aligned}, \tag{3.21}$$

we then obtain exactly the same equations as Eqs. (3.14) and (3.15) with substitution of the term $L^2/2$ for A, which now accounts for the linear and nonlinear phases inside the resonator. We have

$$\begin{aligned}\alpha_1(0) &= \frac{\mathcal{E}_1}{1 - r_1^2\cdot\exp(-2ik_1L)\cdot\left(1+\left|\alpha_3(0)\right|^2\cdot\Lambda_1\right)\cdot\left(1+\left|\alpha_3(0)\right|^2\cdot r_3^2\cdot\Lambda_1\right)} \\ \alpha_3(0) &= \frac{\mathcal{E}_3}{1 - r_3^2\cdot\exp(-2ik_3\cdot L)\left(1-\left|\alpha_1(0)\right|^2\cdot\Lambda_3\right)\cdot\left(1-\left|\alpha_1(0)\right|^2\cdot r_1^2\cdot\Lambda_3\right)}\end{aligned}. \tag{3.22}$$

Still the amplification terms inside the denominators play the most important role, but now these terms are more general, showing simultaneous amplification and nonlinear phase modulation. This occurs because the A terms, and as a result the F-amplification factors, are no longer real but complex and can be written as

$$\begin{aligned}\tilde{F}_1 &= \left(1+\left|\alpha_3(0)\right|^2\cdot\Lambda_1\right)\cdot\left[1+\left|\alpha_3(0)\right|^2\cdot r_3^2\cdot\Lambda_1\right] = \left|\tilde{F}_1\right|\cdot\exp\left(i\Phi_1^{NL}\right) \\ \tilde{F}_3 &= \left(1-\left|\alpha_1(0)\right|^2\cdot\Lambda_3\right)\cdot\left[1-\left|\alpha_1(0)\right|^2\cdot r_1^2\cdot\Lambda_3\right] = \left|\tilde{F}_3\right|\cdot\exp\left(i\Phi_3^{NL}\right)\end{aligned}. \tag{3.23}$$

The presence of Φ_i^{NL} helps the bistable loops to occur at even lower intensities and clearly at different linear cavity detuning, $\Delta\phi_1$ and $\Delta\phi_3$ (see Fig. 3.10). However, the presence of linear and nonlinear absorption terms, γ_{12} and γ_3, reduces amplification efficiency, clearly because of the simultaneous action of linear absorption and the lower nonlinear conversion.

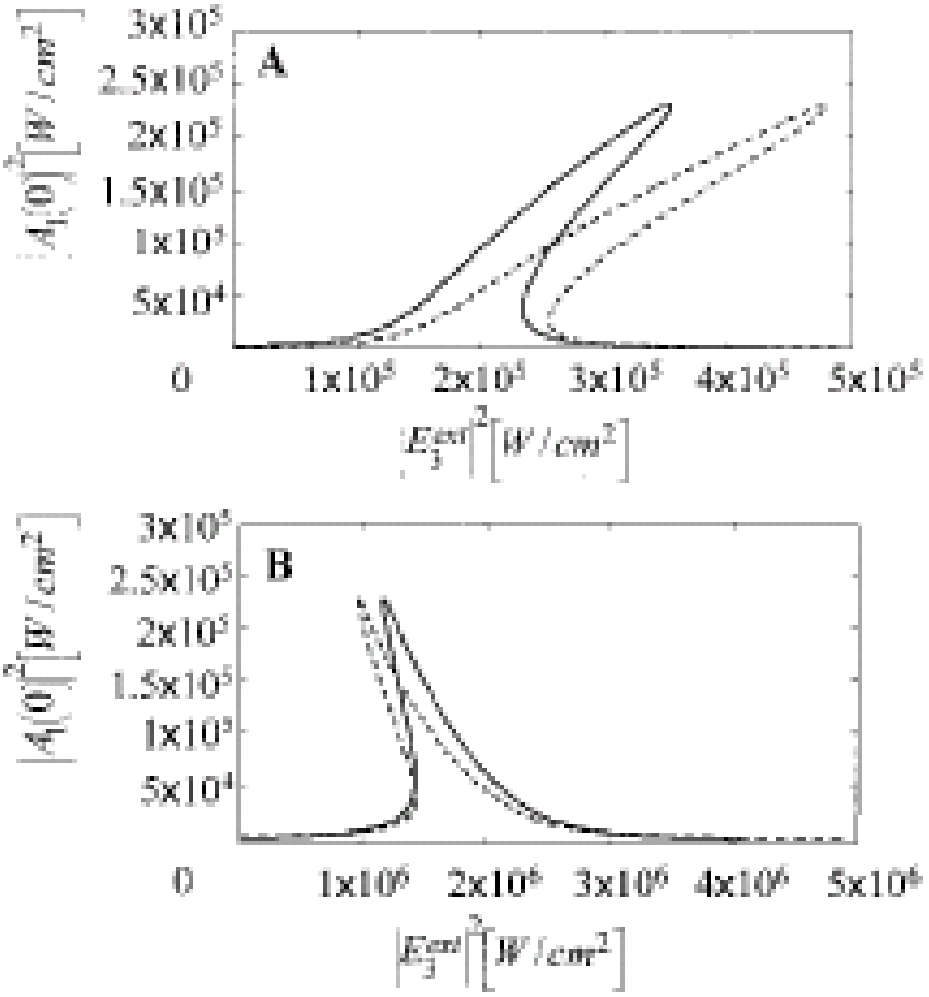

Fig. 3.10. Influence on cavity performances of the phase mismatch of the parametric process and of the linear absorption (dashed-line curve). This behavior is compared with the perfectly matched process without absorption (full-line curve). Both parametric mismatch and absorption decrease cavity efficiencies, making the loops larger.

B. Energy Conservation and the Manley–Rowe Rules

The whole calculation was derived by considering a power expansion of the internal modes during propagation [see Eq. (3.8)]. To check the correctness of the analytical procedure, one must consider whether this process is compatible with the

energy conservation rule. In particular, the power expansion was truncated to the fourth term, but it is not clear whether this is reasonable owing to the high amplification that the cavity feedback can induce, especially during the bistable regimes.

Two main controls have been performed on the field amplitude and phase that grow up on the right-hand side of the input mirror. In particular, $|\alpha_i(0)|^2$ and $|\alpha_i(0)+t_i E_{iext}|^2$ must fulfill the cavity conditions, i.e., they must be the same for both the fundamental and the second-harmonic fields. In Fig. 3.11 these two terms for the fundamental wavelength are depicted (for the case of $\Delta\phi_1$=0.7°; $\Delta\phi_3$=15°): their behavior is almost the same.

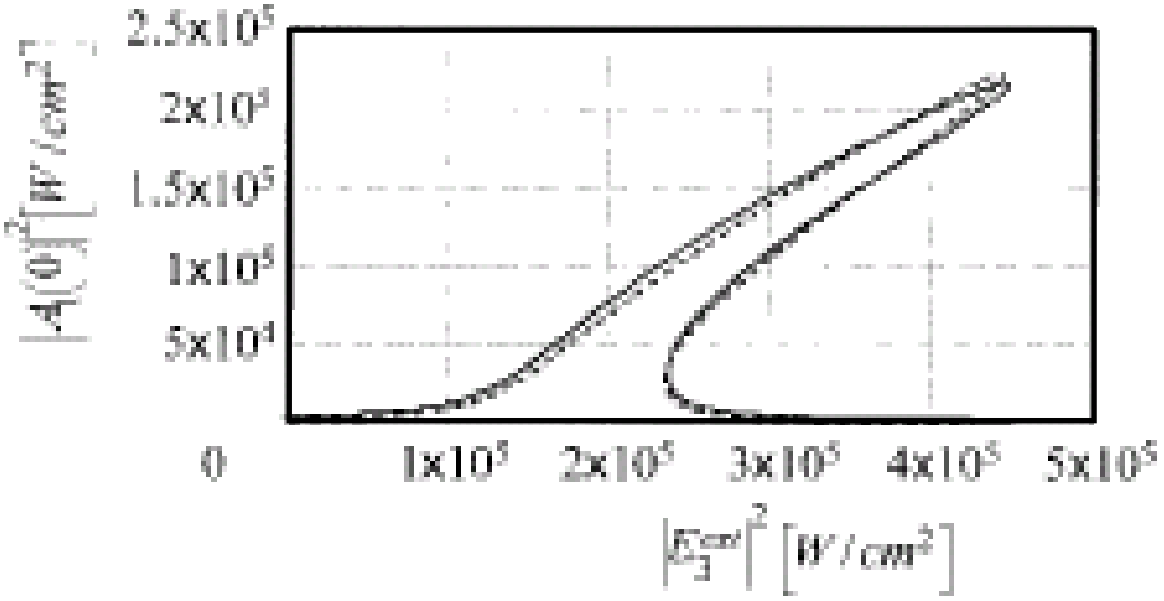

Fig. 3.11. Control of the convergence of the numerical model: From the theory the two terms, $|\alpha_1(0)|^2$ (full-line curve) and $|\alpha_i(0) + t_i E_i^{ext}|^2$ (dashed-line curve), must be equal for both wavelengths in any pumping regime. Here they are reported for the fundamental mode.

In Fig.3.12 the relative errors $\frac{\left|A_i(4)+t_iE_i^{ext}\right|^2-\left|A_i(0)\right|^2}{\left|\alpha_i(0)\right|^2}$ are reported, showing that the numerical calculations are always limited within almost 1% of error. At the same time the Manley–Rowe rule

$$\frac{n_1}{\omega}\left|A_1(z)\right|^2+\frac{n_3}{2\omega}\left|A_3(z)\right|^2=\frac{n_1}{\omega}\left|A_1(0)\right|^2+\frac{n_3}{2\omega}\left|A_3(0)\right|^2, \qquad (3.24)$$

must be verified, as in Fig. 3.13 for the z=L position. If the amplification process is really efficient, the numerical model loses validity owing to the truncation of the power of the power expansion in Eq. (3.8). However, as shown in Fig. 3.14, Eq. (3.24) is verified for low values of the parameter $\Delta\phi_1$, for which bistable loops can be found.

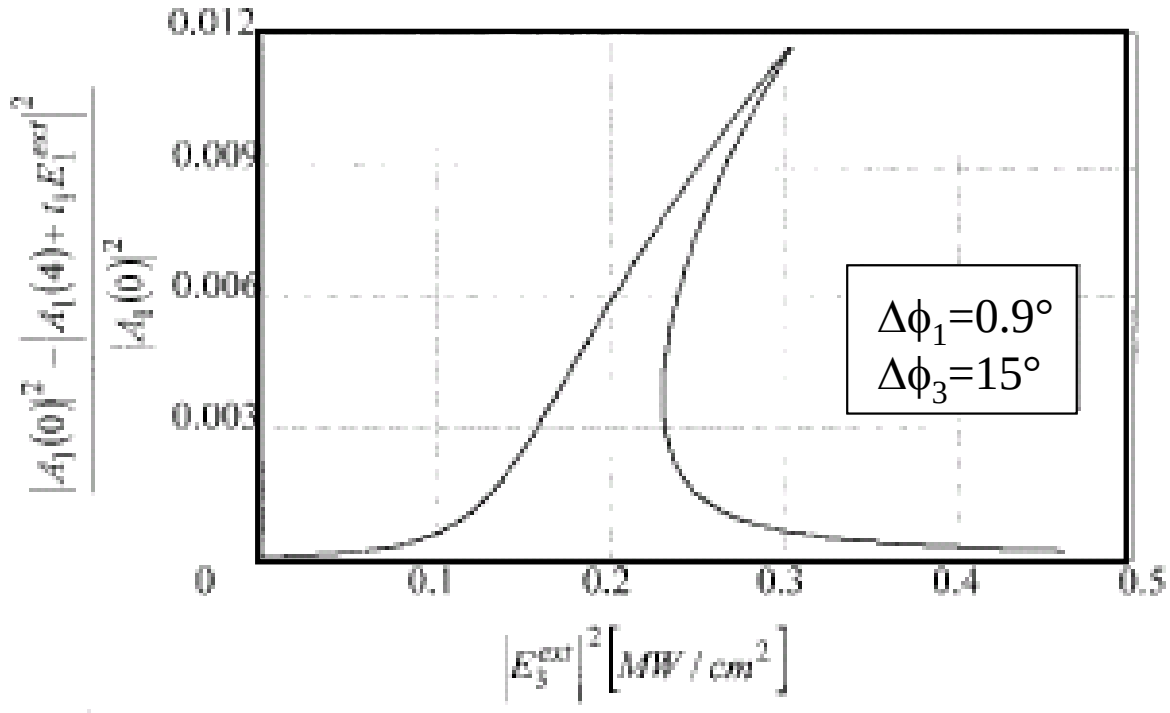

Fig. 3.12. Relative errors recorded during the numerical calculation described in Fig. 3.11. The relative error never exceeds 1.2%.

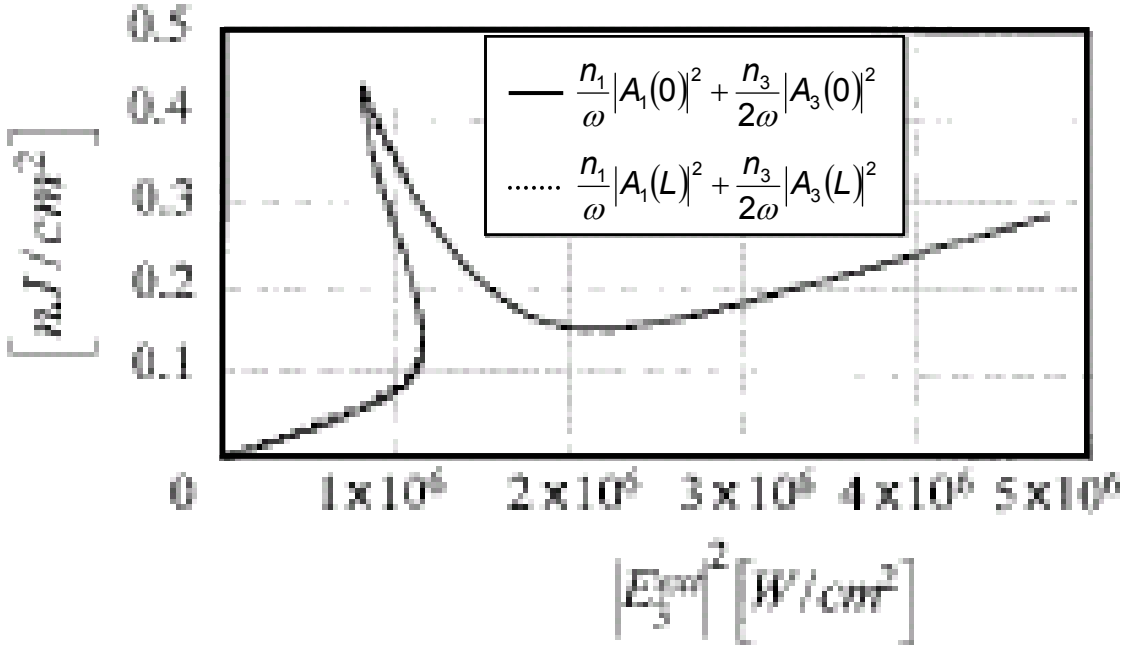

Fig. 3.13. Verification of the Manley–Rowe rule. Also, in this case, as shown in Fig. 3.12, the relative error is really low.

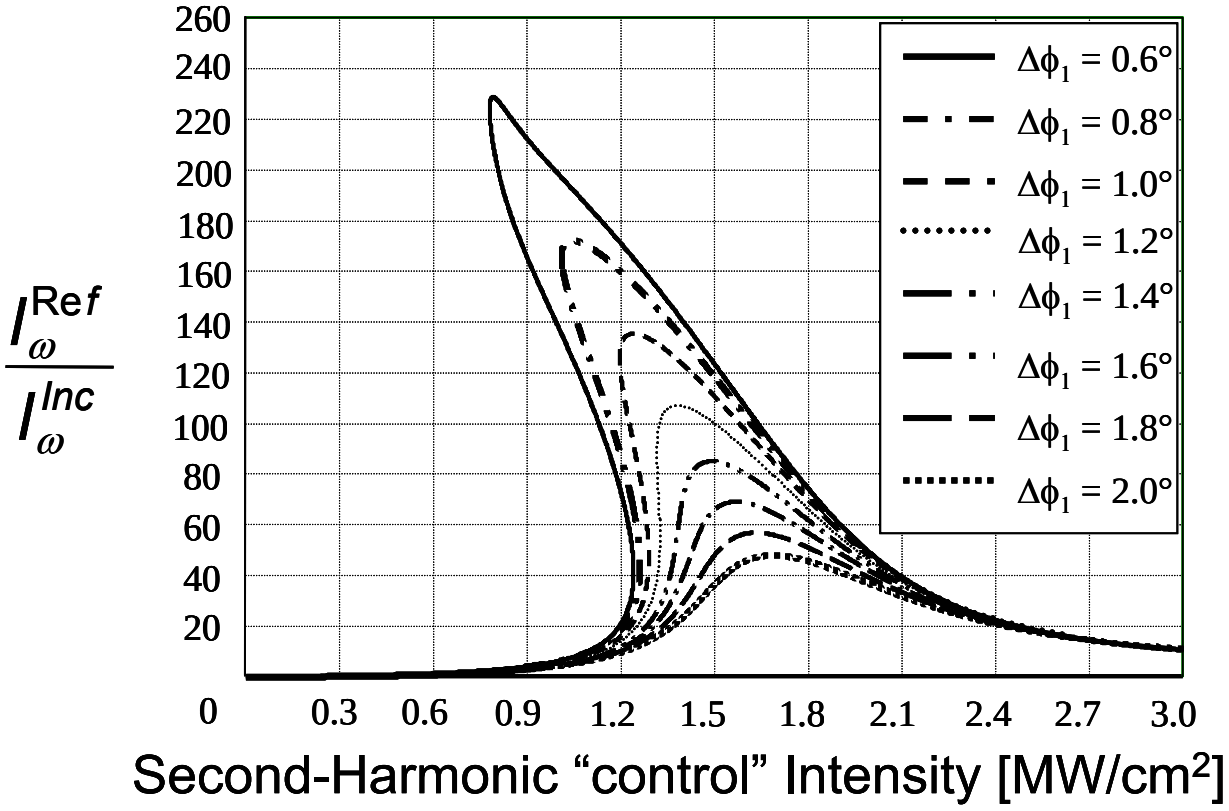

Fig. 3.14. Reflection coefficients of the Fabry–Perot active nonlinear mirror for different $\Delta\phi_1$. Amplifications as high as 220 have been observed at pump intensities of the order of 1MW/cm^2.

References

1. J. Paye and D. Hulin, “Femtosecond response of a semiconductor nonlinear Fabry–Perot etalon,” J. Opt. Soc. Am. B 10, 2371–2376 (1993).
2. N. J. Doran and D. Wood, “Nonlinear optical loop mirror,” Opt. Lett. 13, 56–58 (1988).
3. N. J. Doran, D. S. Forrester, and B. K. Nayar, “Experimental investigation of all-optical switching in fiber loop mirror device,” Electron. Lett. 25, 267–269 (1989).
4. I. Glesk, J. P. Sokoloff, and P. R. Prucnal, Demonstration of all-optical demultiplexing at TDM data at 250 Gbit/s, Electron. Lett. 30, 339–341 (1994).
5. A. D. Ellis, D. M. Patrick, D. Flannery, R. J. Manning, D. A. O. Davies, and D. M. Spirit, “Ultra-high-speed OTDM networks using semiconductor amplifier-based processing nodes,” J. Lightwave Technol. 13, 761–770 (1995).
6. R. DeSalvo, D. J. Hagan, M. Sheik-Bahae, G. Stegeman, E. W. VanStryland, and H. Vanherzeele, “Self-focusing and selfdefocusing by cascaded second-order effect in KTP,” Opt. Lett. 17, 28–30 (1992)
7. A. Re, C. Sibilia, E. Fazio, and M. Bertolotti, “Field dependent effects in a quadratic nonlinear medium,” J. Mod. Opt. 42, 823–839 (1995).
8. G. D’Aguanno, C. Sibilia, E. Fazio, E. Ferrari, and M. Bertolotti, “Field phase modulation and input phase and intensity dependence in a nonlinear second order interaction,” J. Mod. Opt. 45, 1049–1066 (1998).
9. E. Fazio, M. Zitelli, S. Dominici, C. Sibilia, G. D’Aguanno, and M. Bertolotti, “Phase-driven pulse-breaking during perfectly matched second-harmonic generation,” Opt. Commun. 148, 427–435 (1998).
10. E. Fazio, C. Sibilia, F. Senesi, and M. Bertolotti, “All-optical switching during quasi-collinear second-harmonic generation,” Opt. Commun. 127, 62–66 (1996).
11. M. A. Krumbugel, J. N. Sweetser, D. N. Fittinghoff, K. W. DeLong, and R. Trebino, “Ultrafast optical switching by use of fully phase-matched cascaded second-order nonlinearities in a polarization-gate geometry,” Opt. Lett. 22, 245–247(1997).
12. C. N. Ironside, J. S. Aitchinson, and J. M. Arnold, “An alloptical switching employing the cascaded second-order nonlinear effect,” IEEE J. Quantum Electron. 29, 2650–2654 (1993).

13. L. A. Lugiato, C. Oldano, C. Fabre, E. Giacobino, and R. J. Horowicz, “Bistability, self-pulsing and chaos in optical parametric oscillators,” Il Nuovo Cimento 16, 959–977 (1988).
14. L. Lefort and A. Barthelemy, “Cross-phase modulation from second-harmonic to fundamental in cascaded second-order processes: application to switching, Opt. Commun. 119, 163– 166 (1995).
15. C. Sibilia, A. Re, E. Fazio, and M. Bertolotti, “On the second harmonic generation in a ring cavity,” J. Opt. Soc. Am. B 13, 1151–1157 (1996).
16. C. Cojocaru, J. Martorell, R. Villaseca, J. Trull, and E. Fazio, “Active reflection via a phase-insensitive quadratic nonlinear interaction within a microcavity,” Appl. Phys. Lett. 74, 504– 506 (1999).
17. S. Kim, Z. Wang, D. J. Hagan, E. W. VanStryland, A. Koyakov, F. Lederer, and G. Assanto, “Phase-insensitive all-optical transistors based on second-order nonlinearities,” IEEE J. Quantum Electron. 34, 666–672 (1998).

PART III:

Soliton Generation by Photorefractive Effect

Chapter 4

(2+1)-dimensional soliton formation in $Bi_{12}SiO_{20}$ crystal

4.1 Introduction

Spatial solitons in photorefractive materials are really attracting for the number of possible applications in the photonic domain thanks to the extremely low intensity which excite such nonlinearity. Since the first discovery of such solitons[1-3], many experiments[4-12] have been performed in order to characterize the soliton formation as well as the behaviors of different photorefractive materials.

Spatial solitons in photorefractive materials have been predicted in 1992[1] and observed in 1993[2]. Since then, many papers on solitons in photorefractive crystals have been published: a complete review on this can be found in the book by DelRe, Crosignani, and Di Porto[3].

Optical activity has been considered in the past as a detrimental factor for photorefractive spatial solitons formation[4,5]. Photorefractive materials need a static electric field of bias, orthogonal to the light polarization in order to induce optical nonlinearity and, as a consequence, to generate spatial solitons[6]. The optical activity rotates the polarization plane of the optical field, and superimposes it periodically along the crystallographic direction without optical nonlinearity, leading to the loss of soliton confinement (diffraction). Competition between self-focusing, experienced for some orientations of polarization, and diffraction governs the beam dynamics.

In materials with low optical activity, as for example, for $Bi_{12}TiO_{12}$ (BTO) (with a rotatory power of about 8°–10°mm^{-1} at 633 nm^3), this obstacle was overtaken limiting the propagation length and, consequently, limiting the rotation around the polarization direction subjected to self-focusing. This procedure, however, cannot be followed for materials with strong optical activity, as for example for BSO crystal; in this case, the polarization vector rotates by about 39°/mm at 514 nm or 45°/mm at 488 nm[7,8] (just to mention some wavelengths useful for the photorefractive properties), and the crystal should be very short to limit the polarization rotation. In this case, it is difficult to ensure the nonlinear effect (confinement) along reasonable propagation distances. Recently, the possibility of breathing solitons-like propagation in such materials has been analytically demonstrated[9].

In this chapter is reported the experimental observation of (2+1)-dimensional spatial soliton propagation in BSO crystals. It will be demonstrated that solitonic beams are always possible in photorefractive crystals with large optical activity, for any crystallographic direction of the bias field, for very high static bias fields. In fact, by increasing the static bias field, the polarization rotation along the propagation direction accelerates: the rotation period in these regimes can be much shorter than the diffraction length, preventing for efficient diffraction of the beam. We shall analytically demonstrate that the angular speed is inversely proportional to the light beam intensity: thus a competition between acceleration (given by the static field) and deceleration (given by the beam intensity) stabilizes the rotation speed which remains constant across the beam profile. In this case, the beam angular momentum

remains constant along the whole propagation, accelerating and decelerating the polarization according to the breathing of the transversal dimension. However, it was already demonstrated[10,11] that the photorefractive nonlinearity generated also an effective birefringence, which modifies the polarization state from the linear to the elliptical regime.

4.2 Soliton formation dynamics

In order to characterize the whole process of the soliton formation, from the self-focusing to the solitonic regime, numerical simulations of light propagation have been performed. For this purpose, a BSO crystal biased along its [001] crystallographic direction (X) by a static high voltage field and contemporarily illuminated along the $[1\bar{1}0]$ crystallographic direction (Y) by an incoherent background beam has been considered (see Fig. 4.1). A second beam (called signal or soliton beam) was injected along the [110] crystallographic direction (Z) in order to form a soliton. Following this configuration, the electric field of the signal beam has two components, one along *X* and *Y*, respectively; their propagations are described by two equations, coupled together through the optical activity (Γ term) and the photorefractive nonlinearity $\delta\varepsilon_{NL}$:

$$\begin{aligned} &\left(2ik\frac{\partial}{\partial z}+\nabla^2_{transv}\right)E_x - i\Gamma E_y = 0 \\ &\left(2ik\frac{\partial}{\partial z}+\nabla^2_{transv}+\delta\varepsilon_{NL}\right)E_y + i\Gamma E_x = 0 \end{aligned} \qquad (4.1)$$

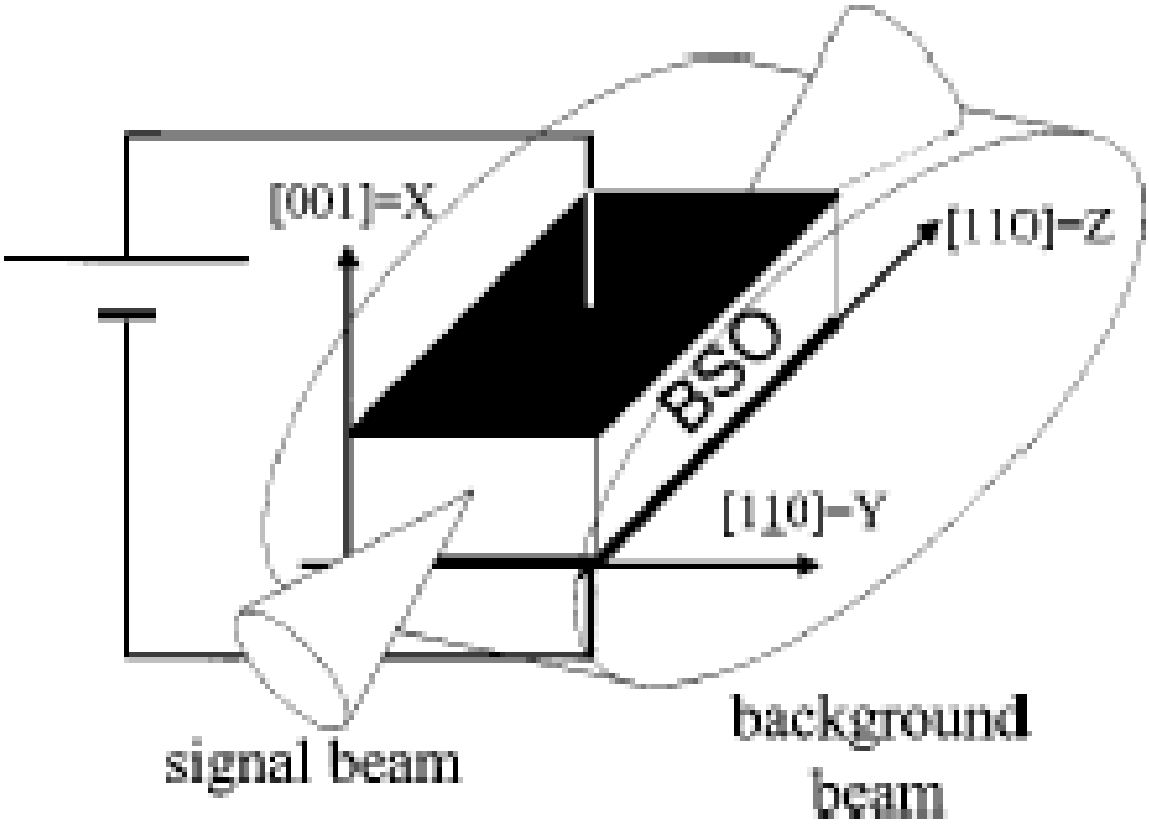

FIG. 4.1. Experimental crystal orientations: the BSO crystal was 8 mm long in its [110] crystallographic direction (called *Z)*, 2 mm along [001] (called *X*), and 3 mm along [1-10] called *Y*. The external bias was applied along *X*; a background beam, incoherent to the signal beam, was sent along *Y* and the signal propagated along *Z*.

The optical activity term here is represented by the gyration constant Γ, defined as the ratio $\Gamma=2\ \rho_0 /k$ between the linear rotatory power ρ_0 and the light wave number *k* inside the crystal. For a BSO crystal, ρ_0 is about 39°/mm at the operating wavelength of 514 nm. The photorefractive nonlinear dielectric constant $\delta\varepsilon_{NL}$ was previously

described by Crosignani *et al.*[12]; in the steady state and drift dominated transport conditions, it can be approximated as

$$\delta\varepsilon_{NL} = -kn_0^2 r_{41} E_{SC} = -kn_0^2 r_{41} \frac{E_{bias}}{1 + I_{soliton} / I_{background}} \tag{4.2}$$

where n_0 is the linear refractive index, r_{41} is the electro-optic coefficient, and E_{sc} is the electric field that screens the applied static bias E_{bias}; the screening field is a function of the applied bias and of the intensity ratio between the soliton ($I_{soliton}$) and the background beams ($I_{background}$), respectively.

Please note that Eq.(4.2), used to simulate soliton formation, is mainly valid in one-dimensional (1D) case. The correct 2D model should involve the material dynamics[13]. However, the used model still well describes the experimental results in this special case, different from that published by anyone before, where a really high bias field is applied. Anyhow, the full material dynamics might give further information on asymmetries that could appear on the beam shape.

Numerical integrations of Eqs. (4.1) consider a Gaussian beam injected at the input, as large as about 10 μm which propagates for 8 mm within the crystal (which corresponds to about 5.5–6.0 diffraction lengths).

Without external bias the laser beam just diffracts, as shown in Fig. 4.2(a). Applying an increasing bias field, the laser beam is more and more confined, but only above 45kV/cm diffraction is completely compensated [see Figs. 4.2(b)–4.2(f)]. These results were obtained injecting a beam with a linear polarization along *Y*: in fact, the injected polarization state is critical for the soliton formation. Fig. 4.3 depicts

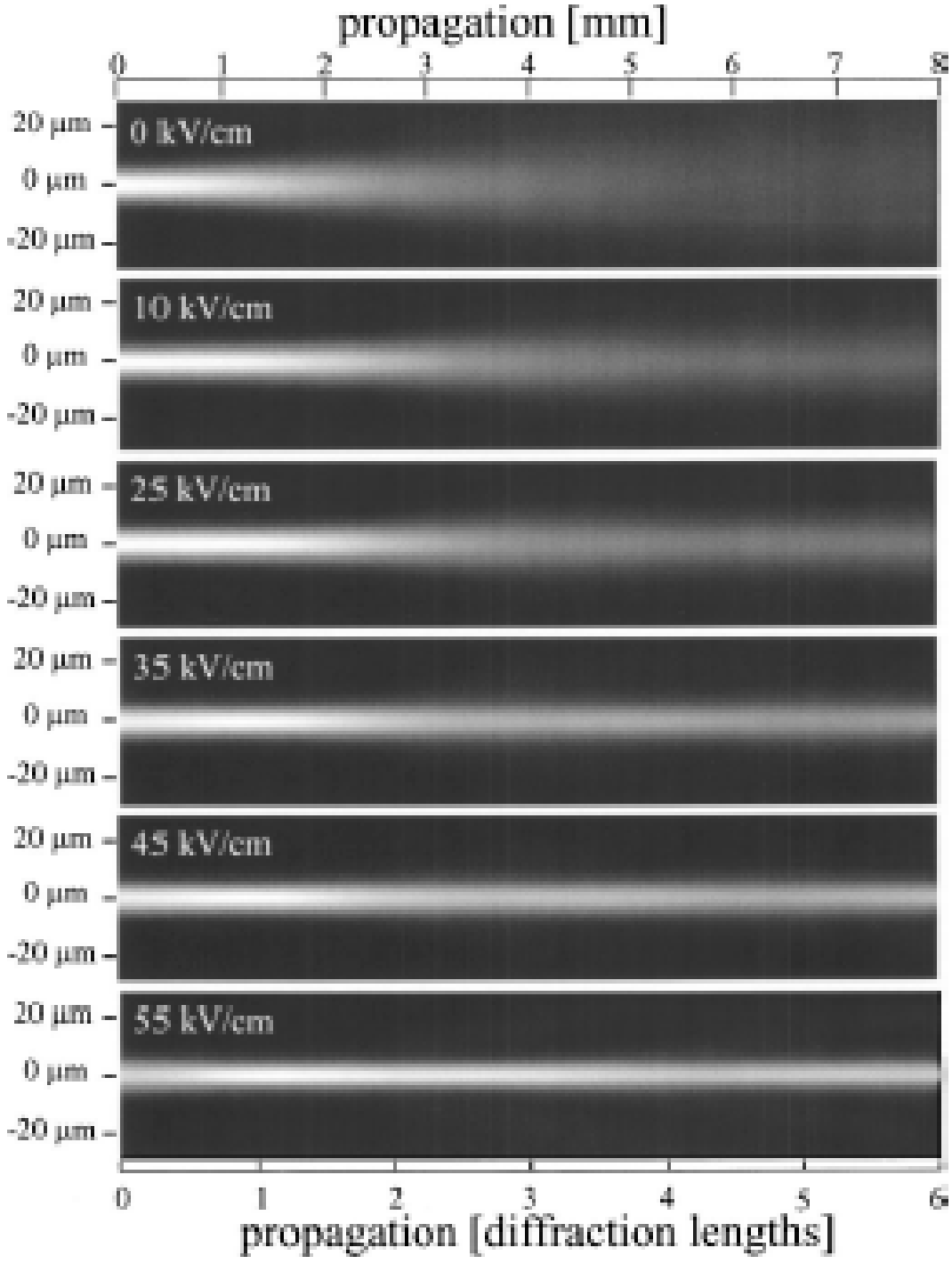

FIG. 4.2. Numerical solutions of the beam propagation for different biases. At 0 kV/cm, the beam linearly diffracts. Increasing the applied bias the beam experiences self-focusing more and more efficient: however, only at about 55 kV/cm, the propagation is keeping the same shape along the whole 8-mm propagation, which corresponds to six diffraction lengths.

a comparison of beam propagation at the same bias conditions of 55 kV/cm, but starting from different polarization states (which are represented on the left-hand side as thicker lines; the optical activity rotation direction is reported as circular arrows for completeness).

Injecting an *X*-polarization state [Fig. 4.3(a)] i.e., with the wave-electric field parallel to the external bias, the beam does not compensate diffraction and diverges. In fact, only the *Y* component experiences self-focusing [see Eq. (4.1)]. If the input polarization is along the *Y* direction [Fig. 4.3(c)], the beam is indeed self-trapped because now the photorefractive nonlinearity is efficient from the beginning. The two intermediate conditions, i.e., polarization states at 45° [Fig. 4.3(b)] and 135° [Fig. 4.3(d)], respectively, give again a self-trapping of the beam, but this time with different efficiencies according to the rotation given by the optical activity (if the polarization is driven towards or away from the *Y* direction). For circularly polarized beams, the rotation direction must be considered with respect to the optical activity one: in Figs. 4.3(e), 4.3(f), polarization rotations parallel and anti-parallel to the optical activity are reported, respectively. In the former case (parallel), a self-trapped beam is formed (even if a strong breathing is excited), while in the latter (anti-parallel one), the beam is diverging.

The beam self-trapping and soliton formation have been experimentally tested by using the setup shown in Fig. 4.4. Light from an Ar_1 laser at 514.5 nm was used for both the signal beam and the incoherent background. Two Pockels cells, one for the background and one for the signal, respectively, set the intensity and the polarization.

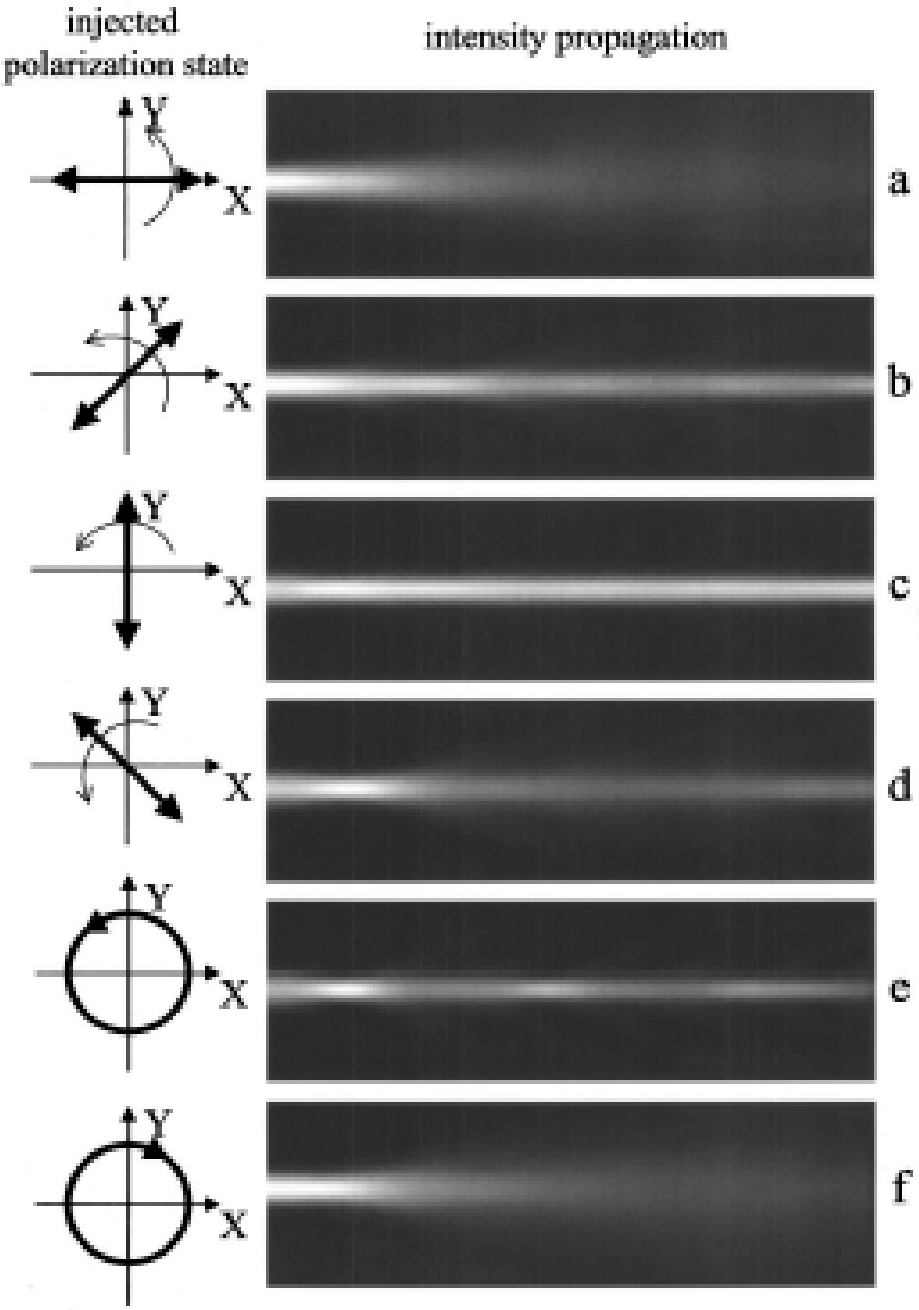

FIG. 4.3. Numerical solutions of the beam propagation at 55 kV/cm of external bias for different input polarization states. On the left-hand side, the input polarization states are represented as thick arrows together with second thin and round arrow that gives the optical activity rotation axis. Injecting an X polarized beam (a), the beam is not confined but diffracts; if instead an Y polarized beam is injected (c) the beam is indeed self-focused and a soliton is formed. Injecting still linear polarizations at 45° (b) and 135° (d), the beams are still confined, but strong breathings influence their propagations, as also occurring is an injected circular polarization that is rotating in the same axis of the optical activity (e). If there is still a circular polarization but with antiparallel rotation with respect to the optical activity injected (f), the beam is not confined and diffracts.

The BSO crystal was 8 mm long along [110], 3 mm along $[1\bar{1}0]$, and 2 mm along [001]; the external static bias was applied along [001]. In order to avoid electric discharge between electrodes, the sample was kept within an insulating cell. The signal beam (Y-polarized) was focused down to a waist of 10 mm and propagated within the sample for about six diffraction lengths. At the crystal output plane, it was imaged on a charge-coupled device (CCD) camera by an optical system with a magnification of 43.

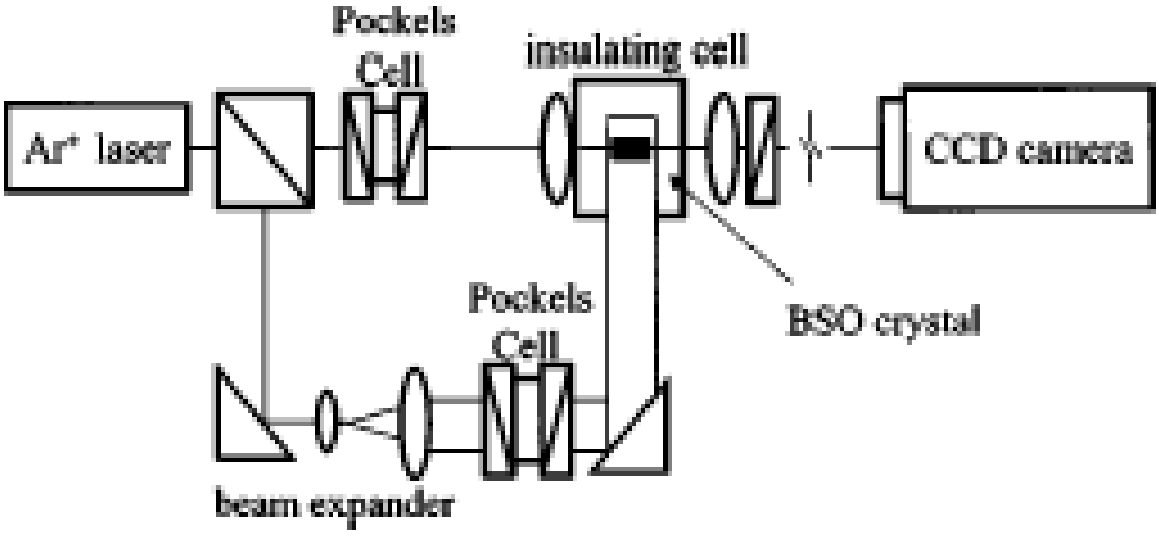

FIG. 4.4. Experimental setup used to investigate the soliton formation. The laser beam from an Ar laser was divided in two beams, one for the background and one for the signal. The background was made incoherent (with a delay line longer than the coherent length of the laser) enlarged and sent transversally on the sample. It was kept within an insulating cell to avoid electric discharge. The output face of the crystal was imaged on a CCD by using an optical system with magnification. The images were then recorded by a PC.

Images of the beam at the input and at output planes have been recorded for bias fields ranging from 0 up to about 55 kV/cm, as shown in Fig. 4.5. Applying an increasing bias field, the light beam becomes narrower and narrower. At 45 and 55 kV/cm, the diffraction is almost completely compensated. In Fig. 4.6, the output waist dimensions in the two *X* and *Y* directions, respectively, normalized to the input one, are reported as a function of the applied bias. The beam shrinkage shows a saturating trend, down to a beam dimension of the same order of the input beam. The shrinkage trend is different for the two transverse coordinates: the obtained soliton-like beam is not circular but elliptical, with an ellipticity factor (defined as the ratio of the minimum axis to maximum axis) of about 60%. This is a consequence of the anisotropy of the screening process[14].

4.3 Polarization dynamics

How is it possible that a light beam can compensate diffraction, if its polarization is periodically rotated along a direction without self-focusing? If the rotation is weak, the propagation does not modify significantly the polarization state, and diffraction can be compensated (this is the case of other photorefractive crystals with lower optical activity, as for example, BTO for which the polarization rotates for few degrees for each millimeter of propagation). Larger rotations can indeed cause some problems if their period is comparable to the diffraction length. In this case, the rotation keeps the polarization for a long propagation in the diffracting state, and consequently the beam diverges. However, really high optical activity could produce rotation periods much shorter than the diffraction length.

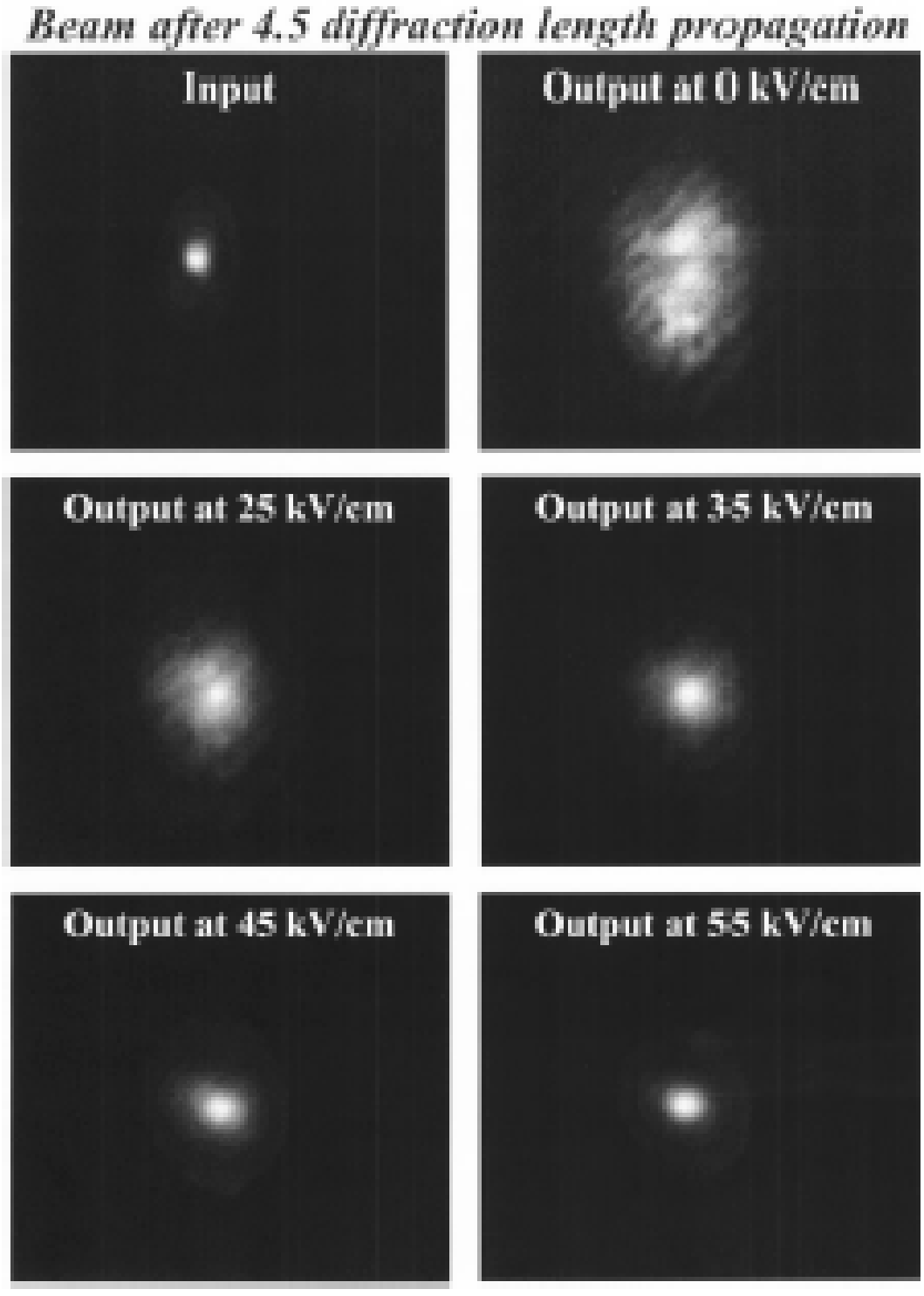

FIG. 4.5. Experimental images of the output beam increasing the bias field applied. A comparison with the input beam demonstrates that at about 55 kV/cm, the diffraction is almost completely compensated.

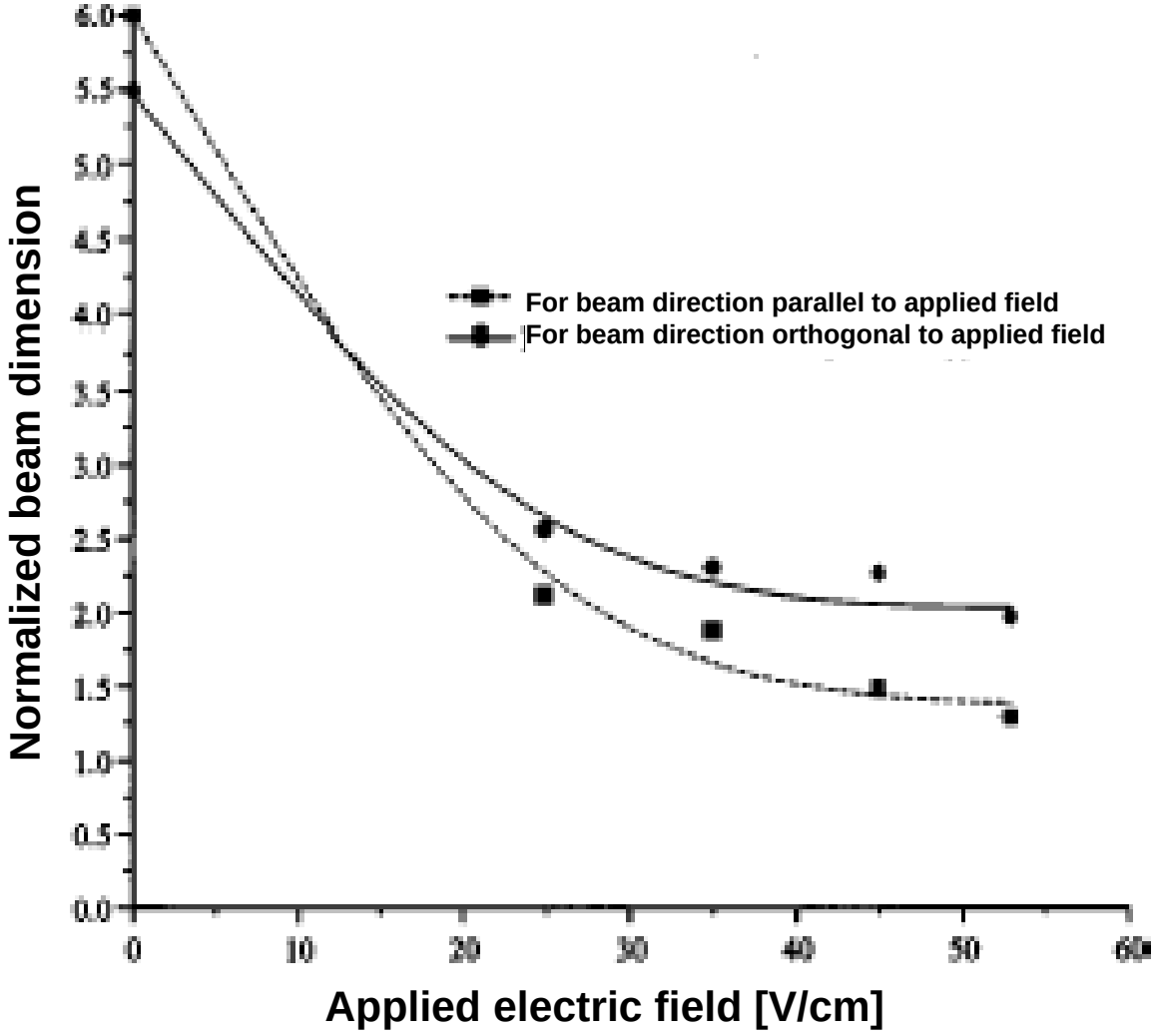

FIG. 4.6. Experimental beam dimensions along the X and Y directions for increasing biases. At about 50–55 kV/cm, the soliton is almost formed. The beam is not circular but elliptical, as a consequence of the asymmetrical action of the photorefractive nonlinearity on the two polarization components.

This case is now again favorable to the soliton formation, because the diffracting state in this case is kept for a short propagation, not enough to make the beam diverge. However, this case of optical activity rotation period, which is much shorter

than the diffraction length, is not our experimental case for the BSO crystal, for which one polarization component remains for about 4–5 mm before being completely converted into the other one, and the beam diffraction length is about 1.8 mm. If this is true in the linear case or for relatively low applied biases, it is not valid anymore for really high biases, for which the polarization rotation speed can accelerate many times because of the photorefractive nonlinearity.

Let us consider the experimental conditions described in Fig. 4.1, i.e., a static bias along the *Y* direction and a signal beam propagating along the *Z* direction. For this particular orientation, the dielectric displacement vector $\vec{D}$ of the light should not have any component along the propagation direction *Z*: it is possible to write without ambiguity $D_z=E_z=0$. Then the $\vec{E}$ vector lies in the plane generated by $\vec{D}$ and $\vec{k}$. From this hypothesis, it is possible to write

$$\frac{D_x}{D_y}=\frac{E_x}{E_y} \tag{4.3}$$

At the same time, the definition of the *X* and *Y* components of the $\vec{D}$ vector in the BSO photorefractive crystal gives

$$\begin{bmatrix} D_x \\ D_y \\ D_z \end{bmatrix} = \begin{bmatrix} n_0^2 & -i\Gamma & 0 \\ i\Gamma & n_0^2+\dfrac{\delta\varepsilon_{NL}}{k} & 0 \\ 0 & 0 & n_0^2 \end{bmatrix} \cdot \begin{bmatrix} E_x \\ E_y \\ E_z \end{bmatrix} \tag{4.4}$$

Equations (4.3) and (4.4) must be simultaneously fulfilled; this leads to the definition of the whole beam as the superposition of two counter-rotating waves[15]: $E_y^{\pm}=iC^{\pm}E_x^{\pm}$, where $C^{\pm}=1/\left(k_E\pm\sqrt{k_E^2+1}\right)$ and $k_E=\delta\varepsilon_{NL}/2\Gamma$. The overlapping of these

two waves generates a field with rotating polarization if the waves have different propagation speeds. The speed difference is now described by the refractive index mismatch Δn of the two waves:

$$\Delta n = \frac{1}{2}\left(n_{+} - n_{-}\right) = -\frac{\Gamma}{2n_0}\sqrt{1+k_E^2} \qquad (4.5)$$

Thus, defining the instantaneous polarization orientation of the rotating field as the angle $\alpha(z)=\Delta n\,\alpha(z) = \Delta n\vec{k}_0 \cdot \hat{z}$, the instantaneous angular speed of the polarization rotation is

$$\rho(z) = \frac{\partial\alpha(z)}{\partial z} = \rho_0\sqrt{1+k_E^2} \qquad (4.6)$$

The factor $\sqrt{1+k_E^2}$ describes a correction to the linear rotation speed, which depends on the beam intensity, on its profile and on the external bias field intensity, through the k_E^2 term, i.e., through $\delta\varepsilon_{NL}$. For the BSO crystals, at a bias of about 55 kV/cm with typical values of the intensity ratio lower than 1, $\rho = \rho_0\sqrt{1+k_E^2} \approx (3-4)\rho_0$: this acceleration of the polarization is not just a small correction. As a consequence, the rotation period can be three to four times shorter than in the linear case and, as a consequence, can become shorter than the diffraction length as well, compensating the diffraction.

Total conversion of the polarization state within 500–600 μm of propagation with about 40–50 kV/cm of bias have been calculated. However, not only an acceleration of the optical activity influences the beam dynamics but also an induced birefringence: in fact, the asymmetric action of the photorefractive nonlinearity on the

two light polarization components [see Eqs. (4.1)] produces an asymmetrical phase modulation of these components and consequently induces a nonlinear birefringence. This birefringence makes the polarization state to be no more linear but elliptical, with the major axis (which now coincides with the original linear polarization direction) rotating with the nonlinear speed $\rho(z)$ previously calculated. For bias fields lower than 20–25 kV/cm, the polarization ellipticity is not so large, and the induced birefringence can be considered as a small modification of a linear polarization state. For this reason, in Fig. 4.7 it is represented the maps of the polarization orientation during the beam propagation as arrows (but effectively the maps better represent the major axis orientations of elliptical polarization). Without external bias, a linear rotation of about $(3/2)\pi$ of the polarization occurs during the 8mm propagation (more precisely the linear optical activity rotates the polarization plane for about 310°). Increasing the bias, the polarization starts to rotate faster: this acceleration is not uniform across the beam. It starts in one portion of the beam and then slowly widens across it. For higher biases, the induced birefringence can largely modify the polarization state until even circular polarizations are reached: in these regimes, the arrow mapping cannot be used any more because they lose significance. However, the polarization evolution during propagation can be still analyzed without ambiguity just by describing the polarization dynamics of the central portion of the beam on a Poincare´ sphere. This is possible because it has been observed that above 10–20 kV/cm of external bias, the polarization state is the same across all the transversal sections of the beam.

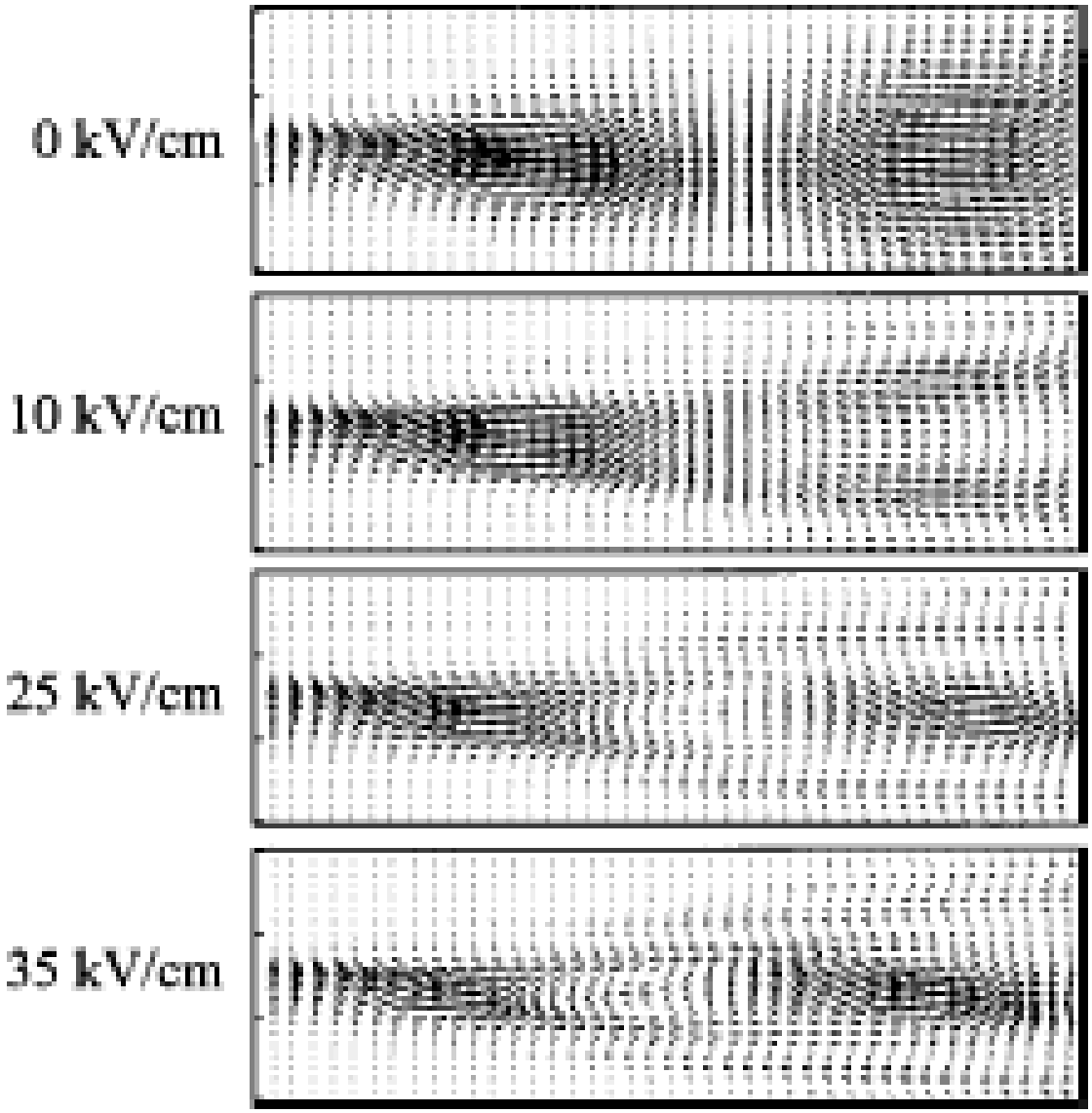

FIG. 4.7. Maps of the polarization orientation during the propagation. By increasing the bias field the polarization rotates faster, factor that helps the diffraction compensation. Some losses are present because of the self-focusing and of the beam breathing, which are caused by the injection of a Gaussian beam at the input. It is interesting to note that these losses have a fixed polarization that does not rotate any more. This map representation cannot be used anymore for applied biases higher than 35 kV/cm: in these cases, an induced birefringence modifies the polarization state from linear to elliptical. In this case, the polarization dynamics must be analyzed on a Poincare´ sphere.

This is a direct consequence of the saturating expression of the rotation speed $\rho(z)$: in fact, Eq. (4.6) states that $\rho(z)$ is directly proportional to k_E and consequently to the nonlinear dielectric constant $\delta\varepsilon_{NL}$. This means that it is directly proportional to the external bias field as well [see Eq. (4.2)], and inversely proportional to the light beam intensity; then the rotation acceleration is favored by a high bias but it is slowed down in the center of the beam where the intensity is higher. The simultaneous combination of these two factors, larger and smaller accelerations across the beam, forces the polarization to reach just one constant and homogeneous state for the whole beam at each propagation position: this is a necessary condition for the soliton formation and consequently for diffraction compensation. The soliton solution (at least for the lowest soliton order) is, in fact, a pure amplitude solution, without any phase modulation across the beam (in case of breathing solitons, a transverse phase modulation is present in order to slightly focus and defocus the beam). This is analogous to saying that the angular momentum of the soliton beams with rotating polarization must be a constant of motion, as it was analytically considered as basic hypothesis for the soliton solution[6].

The light propagation in the homogeneous polarization regime is then represented on the Poincarè sphere, as shown in Fig. 4.8 where the S_1-S_2 projections of the sphere describe the polarization evolutions at increasing biases. For 0 kV/cm of external bias, the polarization dynamics describes an equatorial arc as large as about 310°. Already at 10 kV/cm, the polarization dynamics describes more than one complete turn around the sphere (a bit more than $7\pi/2$).

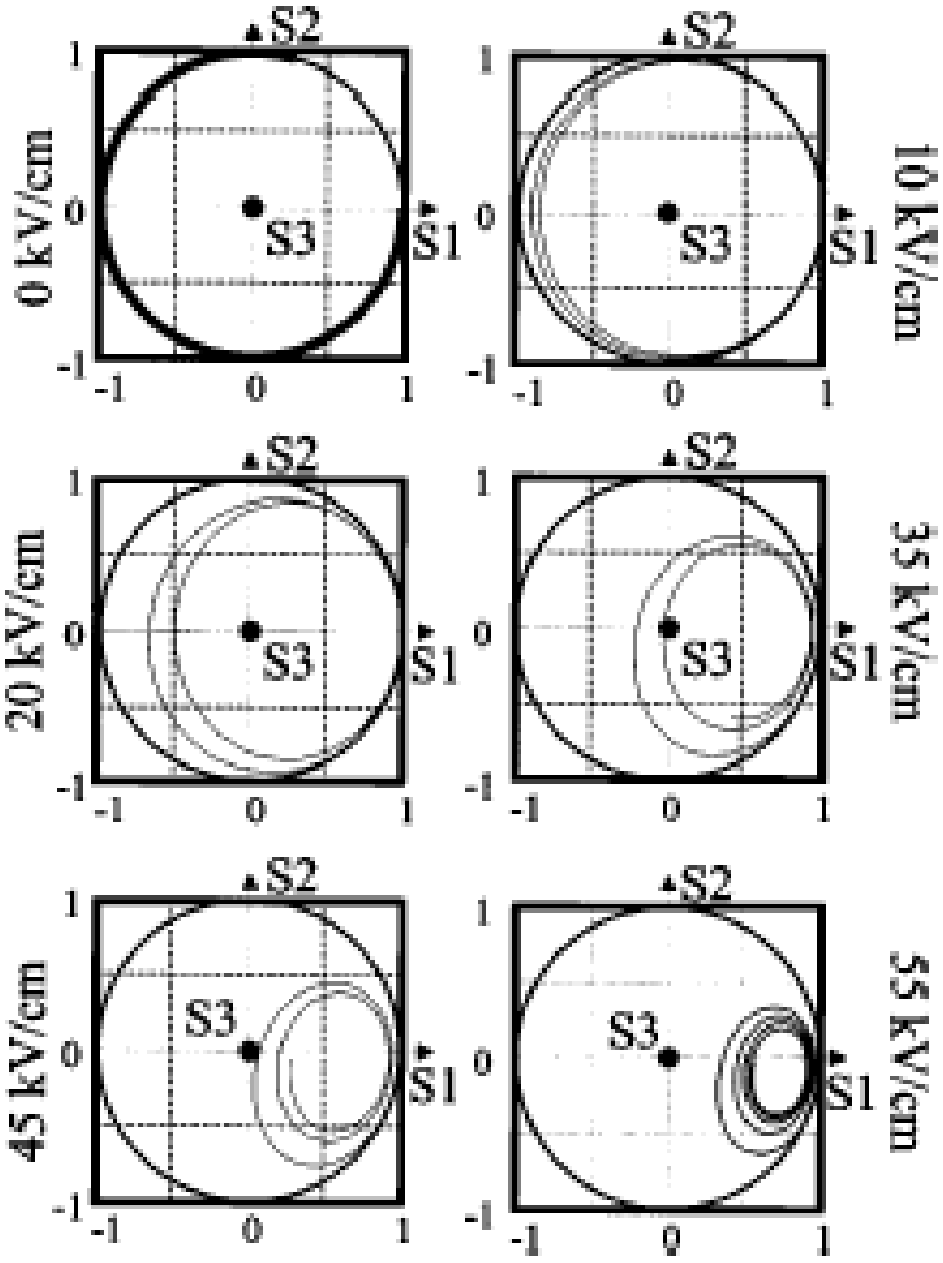

FIG. 4.8. Representation of the polarization dynamics of the beam for increasing applied biases. The graphics show the S_1-S_2 plane projection of the Poincare´ sphere: we have chosen this planar representation of the sphere, instead of the whole 3D one, because it is the only representation able to show the whole polarization trajectories. By increasing the applied biases, the trajectories roll up in smaller and smaller loops. At 45 and 55 kV/cm, the trajectories are confined in the semiplane $S_1>0$, which means the polarization is not anymore completely rotating but vibrates around the Y direction. All the orbits converge towards an attractor state, which is an elliptic state, with the axis oriented as X and Y, and with ellipticity $\delta\varepsilon_{NL}/\Gamma$.

By increasing the bias it is evident that the polarization rotation accelerates, describing many turns, but on the same time the induced birefringence pushes the polarization to follow smaller trajectories which approach the S_3 axis (at 35 kV/cm, the polarization trajectory passes for the circular state). Increasing more the external bias, the dynamics is more concentrated within the region for $S_1>0$, rotating around a stable state: actually, it is quite clear, observing all the obtained trajectories, that all of them rotate around a stable state, which is located within the plane $S_2=0$. Without bias, the center of the polarization rotation is $S_1=0$, while increasing the external bias the center of the polarization rotation moves towards the *Y* axis, i.e., forcing the polarization to follow rotation loops smaller and smaller around the attraction state defined by a dephasing of $\pi/2$ between polarizations (i.e., the major axis parallel to the *Y* direction) and by an ellipticity of $\delta\varepsilon_{NL}/\Gamma$. It is clear from dynamical paths in Fig. 4.8 that the injected beam needs some propagation to follow in the final loop: this occurs, in our simulation, only for 45 and 55 kV/cm applied, whose final polarization states are described by loops almost overlapping after each round turn. In these regimes, the polarization is finally stable during propagation, homogeneous along the transverse direction, and the beam confined: thus, in these conditions a pure solitonic state is reached.

The initial polarization state is critical for the soliton formation, as previously described for the beam propagation. Thus, it has been analyzed, always on the Poincare´ sphere, the polarization dynamics from different polarization states, as shown in Fig. 4.9 (here the numbering follows the same numbering of Fig. 4.3 for

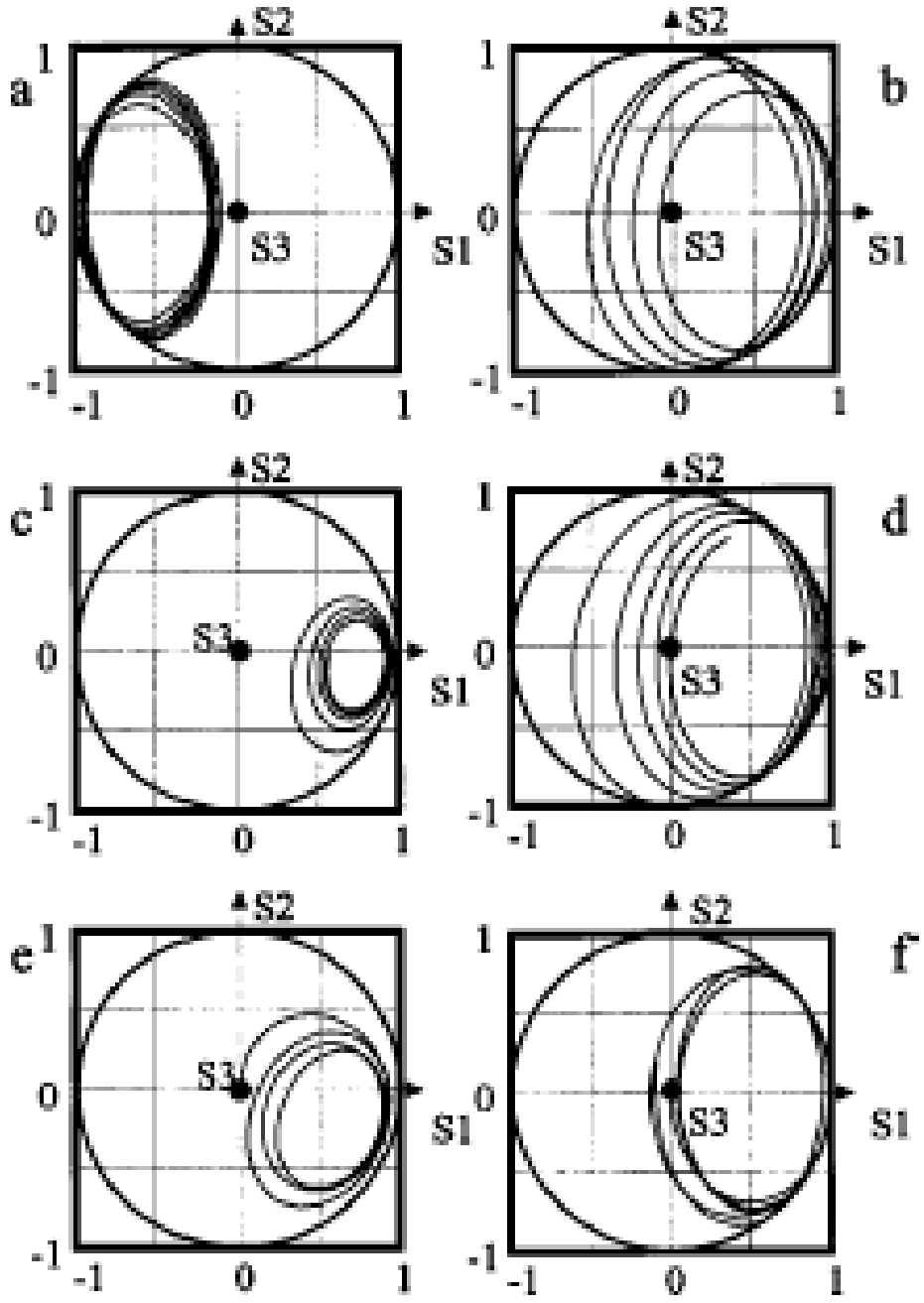

FIG. 4.9. Representation of the polarization dynamics of the beam at 55 kV/cm of applied bias for different input polarization states. (a) X polarization injected; (b) 45°-rotated polarization injected; (c) Y polarization injected; (d) 135°-rotated polarization injected; (e) circular polarization, rotating parallel to the optical activity axis; (f) circular polarization, rotating antiparallel to the optical activity axis.

easier comparison). Injecting a linear *X* polarization [case (a): initial state at S_1=-1, S_2=0, S_3=0], the laser beam does not form any confined state but diverges; its polarization dynamics still describes an high acceleration of the rotation, which now occurs in an unstable region. The beam polarization is now following loops larger and larger because its light diffracts. Injecting a linear polarization at 45° [case (b): initial state at S_1=0, S_2=1, S_3=0], and 135° [case (d): initial state at S_1=0, S_2=-1, S_3=0] with respect to the *X* direction, the polarization follows large trajectories which are converging towards the attraction state (dephasing $\pi/2$, ellipticity $\delta\varepsilon/\Gamma$) located in the semi-plane (S_2=0,S_1>0). Injecting a *Y*-polarized beam [case (c): initial state at S_1=1, S_2=0, S_3=0], the dynamic route is soon attracted in a stable loop, i.e., it forms a stable soliton. Injecting a circular polarization rotating in the same direction of the optical activity one [case (e): initial state at S_1=0, S_2=0, S_3=1; clockwise rotation] again the dynamic route is attracted in an almost stable loop, larger than the linear Y-polarization case. In fact from the intensity propagation map shown in Fig. 4.3(e), it is clear that the beam is still self-confined but is strongly pulsing around different dimensions (and polarization states). The final case is the injection of a circular polarization with an opposite rotation with respect to the optical activity [case (f): initial state at S_1=0, S_2=0, S_3=1; counterclockwise rotation]. The trajectory starts from the initial state and rotates (counterclockwise) towards the S_1=1, S_2=0, S_3=0 state (*Y* polarization): at this point the polarization rotation is inverted by the optical activity that dominates the dynamics, forcing the polarization to rotate again in the clockwise direction. As in the first case (a) diffraction dominates the intensity propagation,

leading the polarization to follow larger and larger loops. Experimentally, the polarization properties of the beam at the output plane has been analyzed recording the beam profiles for the *Y*- and *X*-polarization orientations at different bias fields, as shown in Fig. 4.10. At 10 kV/cm, the polarization state is almost linear and large. At 25 kV/cm, the beam is smaller and the polarization state shows that the *Y* profile is more intense than the *X* component. At 35 kV/cm, the *X* component is now larger with an darker hole inside: this behavior is clearly described by the polarization map in Fig. 4.7; the beam is going toward a solitonic profile losing some energy during propagation. This lost energy is located as rings around the beam (much brighter along the *Y* direction). The central part of the beam has now only an *Y*-polarization component: in fact, the central part of the *X* component is now dark. At 45 kV/cm, the beam has almost reached an elliptical state: in fact the confined beam has now both the *X* and *Y* polarization components. It is interesting to note that the diffracted portion if the beam (i.e., the large ring present is the *X*-polarization image) has a fixed polarization that does not rotate anymore, neither becomes elliptical. This feature was numerically found in the polarization maps of Fig. 4.7, where it is possible to follow these propagation losses without polarization rotation. At about 55 kV/cm, the polarization state is now described by both the *X* and *Y* components, both of them completely confined. Still, here small losses are present in the *X* component, whose intensity is much smaller than the solitonic beam. It must be pointed out here that the presence of losses does not mean that the solitonic beam is lossy while that the injected Gaussian profile is not optimized for the solitonic formation.

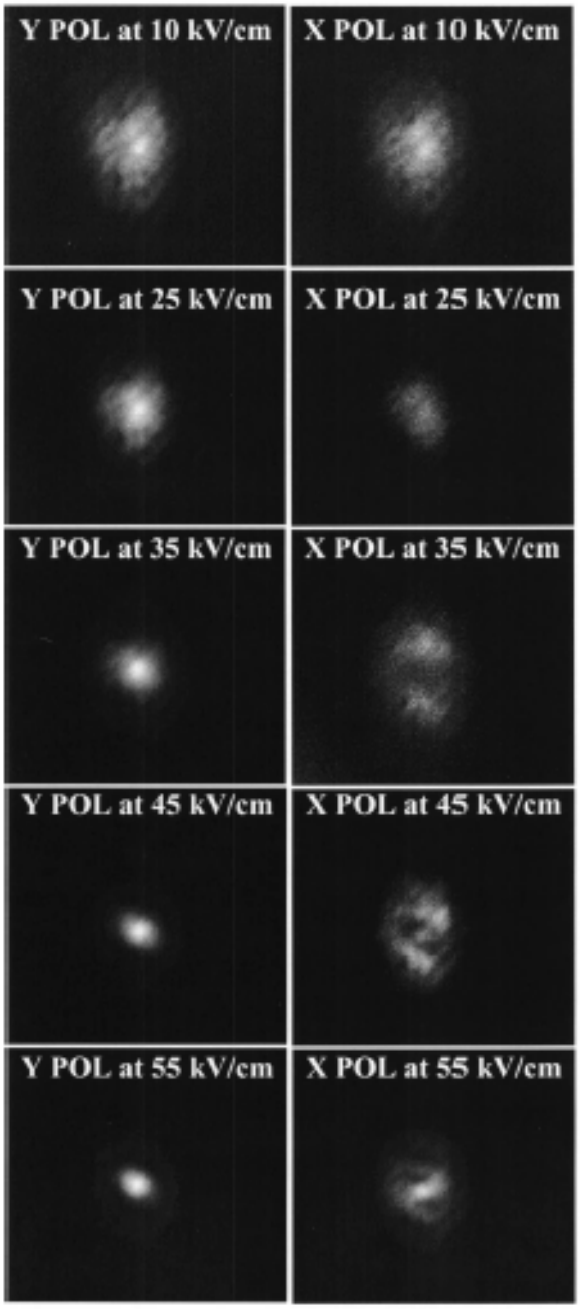

FIG. 4.10. Experimental images of the X and Y polarization components at the output plane for different applied bias. The large rings visible for the X component at 35 and 45 kV/cm are the losses given by the breathing because a Gaussian beam is injected at the input. It can be observed that these losses do not rotate but keep a fixed polarization, as numerically described in the maps of Fig. 7. At 55 kV/cm, the soliton is completely formed: along the two crossed polarization direction, the same profile is present because the solitonic polarization state is now elliptical.

4.4. Comparison with the analytical solution

Analytical solutions for the soliton formation in photorefractive materials with strong optical activity have been recently found[9] and experimentally verified for the (1+1)-dimensional case. The coupled equations (4.1) for the light propagation in photorefractive materials (in the slowly varying envelope approximation[5]), have been analytically solved, under the hypothesis of constant angular momentum of the spatial soliton during propagation. This assumption is the basis for the soliton formation as already described. It allowed to express the beam as the vectorial product of two fields, one transverse (describing the transverse shape of the beam) and one longitudinal along the propagation direction (describing the angular rotation of the polarization): this last longitudinal field is constant for the soliton. The constant-momentum assumption, using cylindrical coordinates normalized to the photorefractive nonlinearity ($Z=ckz$, $\phi=\arctan(y/x)$, $r=\sqrt{ck\left(x^2+y^2\right)}$ or better $r_N=\sqrt{\pi/2R}\cos\left(\frac{1}{2}\phi+\frac{1}{2}g_1kz-\pi/4\right)r$, where $c=n_0{}^2\ r_{41}E_0$ and R is the intensity ratio $I_{soliton}/I_{background}$. gave the analytical solitonic solution

$$I(r,\varphi,Z)=\frac{2RI_{background}}{\pi^2w_0^2}\gamma^2\exp\left(2r_N^2/w_0^2\right)\left[1+\frac{2}{\cosh^2\left(\sqrt{2}r_N\right)}\right] \qquad (4.7)$$

where w_0 is the input Gaussian beam width and γ^2 is a normalized term which describes the periodical beam breathing. According to Eq. (4.7), the soliton width is

$$w_{soliton}=\frac{1}{k\sqrt{n_0^2r_{41}E_0}}\left[\frac{\pi^2}{4R^2}+\frac{1}{w_0^2}\right]^{\frac{1}{2}} \qquad (4.8)$$

which means that it is scaling as $(w_0R)_{21}$, as expected. For our experimental case, considering w_0=10.5μm and R=4, we obtain a necessary bias between 55 and 58 kV/cm in order to reach the soliton solution, which is in good agreement with the experimental observations.

References

1. M. Segev, B. Crosignani, A. Yariv, and B. Fischer, Phys. Rev. Lett. 68, 923 (1992).
2. Crosignani, M. Segev, D. Engin, P. di Porto, A. Yariv, and G. J. Salamo, J. Opt. Soc. Am. B 10, 446 (1993).
3. E. DelRe, B. Crosignani, and P. di Porto, in Spatial Solitons, edited by S. Trillo and W. Tourellas, Springer Series in Optical Sciences Vol. 82 (Springer, Berlin, 2001).
4. S. R. Singh and D. N. Christodoulidis, J. Opt. Soc. Am. B 13, 719 (1996).
5. W. Krolikowski, N. Akhmediev, D. R. Andersen, and B. Luther-Davies, Opt. Commun. 132, 179 (1996).
6. M. Segev, G. C. Valley, B. Crosignani, P. di Porto, and A. Yariv, Phys. Rev. Lett. 73, 3211 (1994).
7. M. P. Petrov, S. I. Stepanov, and A. V. Khomenko, in Photorefractive Crystals in Coherent Optical Systems (Springer-Verlag, Berlin, 1991).
8. E. Fazio, F. Mariani, A. Funto, M. Zitelli, M. Bertolotti, V. Babin, and V. I. Vlad, J. Opt. A, Pure Appl. Opt. 3, 466 (2001).
9. E. Fazio, V. Babin, M. Bertolotti, and V. I. Vlad, Phys. Rev. E 66, 016605 (2002).
10. A. Marrakchi, R. V. Johnson, and A. R. Tanguay, Jr., J. Opt. Soc. Am. B 3, 321 (1986).
11. B. I. Sturman, E. V. Podivilov, V. P. Kamenov, E. Nippolainen, and A. A. Kamshilin, J. Exp. Theor. Phys. 92, 108 2001).
12. B. Crosignani, M. Segev, D. Engin, P. di Porto, A. Yariv, and G. J. Salamo, J. Opt. Soc. Am. B 10, 446 (1993).
13. A. Zozulya and D. Anderson, Phys. Rev. A 51, 1520 (1995).
14. A. Zozulya, D. Z. Anderson, A. V. Mamaev, and M. Saffman, Europhys. Lett. 36, 419 (1996).
15. M. Born and E. Wolf, Principles of Optics, 6th ed. (Pergamon Oxford, NY, 1980).

Chapter 5

Soliton in $Bi_{12}SiO_{20}$ crystal at 633nm

5.1 Introduction

Part of the actual research for new photorefractive materials is pushing towards the infrared region of the light spectrum because of possible applications in the telecommunication domain. However not many materials are really efficient in such region, and moreover their availability in the market is really poor, being them still research topic for crystal growers.

In the present work it is present a new method that allow the applicability of the "old" but well-known photorefractive crystals in spectral regions where their absorption is to low to efficiently give rise to photorefractive nonlinearity. For this investigation $Bi_{12}SiO_{20}$ photorefractive crystals has been chosen (BSO) among all the others, because of our material knowledge. Recently spatial solitons in BSO crystals have been theoretically[1-3] and experimentally[4-7] demonstrated: however their applicability is limited in the blue-green spectral region of the light, due to energy band structure.

Grunnet-Jepsen et al.[8] in 1995 measured the effective electro-optic coefficient of BSO at 633nm measuring the polarization rotation induced by at variable bias voltage applied. They introduced a current-assisted model to analyze such results.

Latter on in 1999 Kobozev et al.[9] measured a light-induced absorption at 633nm using a kind of pump-probe experiment.

In the present experiment the light absorption at 633nm induced by the presence of a second beam at 514nm has been used. The model uses a procedure similar to the Grunnet-Jepsen model. Let us consider two different electronic populations in the conduction band, one cold, excited at the bottom by the green light at 514 nm, and one hot, excited at higher energies by the absorption of the 633nm photons by the cold population. Both these populations participate to the current that flows inside the crystal when a bias voltage is applied. However they move with different mobilities, according to their kinetic energy and to the band curvature. This difference in the drift speed, in the stationary case, generates a spatial modulation of the conducting field, which consequently modulates the dielectric constant by the electro-optic effect.

5.2 Theoretical Model

A laser beam at 633 nm usually is not able to efficiently excite a photorefractive nonlinearity inside a BSO material, because its absorption is too low. All the previous works on BSO crystals have been using radiation at wavelengths of 514 nm or shorter, where the absorption becomes significant.

Let’s consider now a PR crystal uniformly illuminated by a CW background light which is absorbed, let’s say at 514 nm: this time the illumination continuously

generates electrons in the conduction band, which can give rise to a current if a bias electric field is applied to the crystal.

If now a laser beam at 633 nm propagates inside the crystal, the green-excited free carriers can now absorb the red light I_R, jumping to higher energy level in the conduction band. This process is described by a 3-level model for the electrons (and a two-level models for the holes), which involves the two absorption processes given by the green and red lights (see the scheme in fig.5.1):

$$\textit{Electrons:}\begin{cases}\dfrac{\partial n_0}{\partial t} = \sigma_G I_G (n_0 - n) - (\gamma n + \gamma_+ n_+) N_+ \\ \dfrac{\partial n}{\partial t} = \sigma_G I_G (n_0 - n) - \sigma_R I_R n - \gamma_+ n N_+ + \gamma_{IB} n_+ \\ \dfrac{\partial n_+}{\partial t} = \sigma_R I_R n - \gamma_+ N_+ n_+ - \gamma_{IB} n_+ \end{cases} \tag{5.1}$$

$$\textit{Holes:}\quad \begin{cases}\dfrac{\partial N_+}{\partial t} = \sigma_G I_G (N - N_+) - (\gamma n + \gamma_+ n_+) N_+ \\ n_0 = N - N_+ \end{cases} \tag{5.2}$$

N is the total number of donor atoms, while N_+ are the ionized ones; n_0, n and n_+ are the electron populations in the trapped states, bottom and high energy states of the conduction band respectively; the σ terms identify the absorption cross section for the green (σ_G) and red (σ_R) lights; the γ terms are the inverse of the electron life times for inter-band (γ and γ_+) and intra-band (γ_{IB}) transitions. Eq. (5.2.b) describes

the connection between the electron and hole models. These equations should be combined with the material equations:

$$\begin{aligned} &\vec{\nabla}\cdot\vec{D}=\rho \\ &\rho=e(N_{+}-n-n_{+}) \\ &\vec{J}=e(\mu\, n+\mu_{+}n_{+})\vec{E}_{CD} \\ &\vec{\nabla}\cdot\vec{J}=0 \end{aligned}, \qquad (5.3)$$

where eq. (5.3a) describes the Gauss theorem for the dielectric displacement vector $\vec{D}$ and the free-carrier distribution ρ, which is the combination of the excited hole and

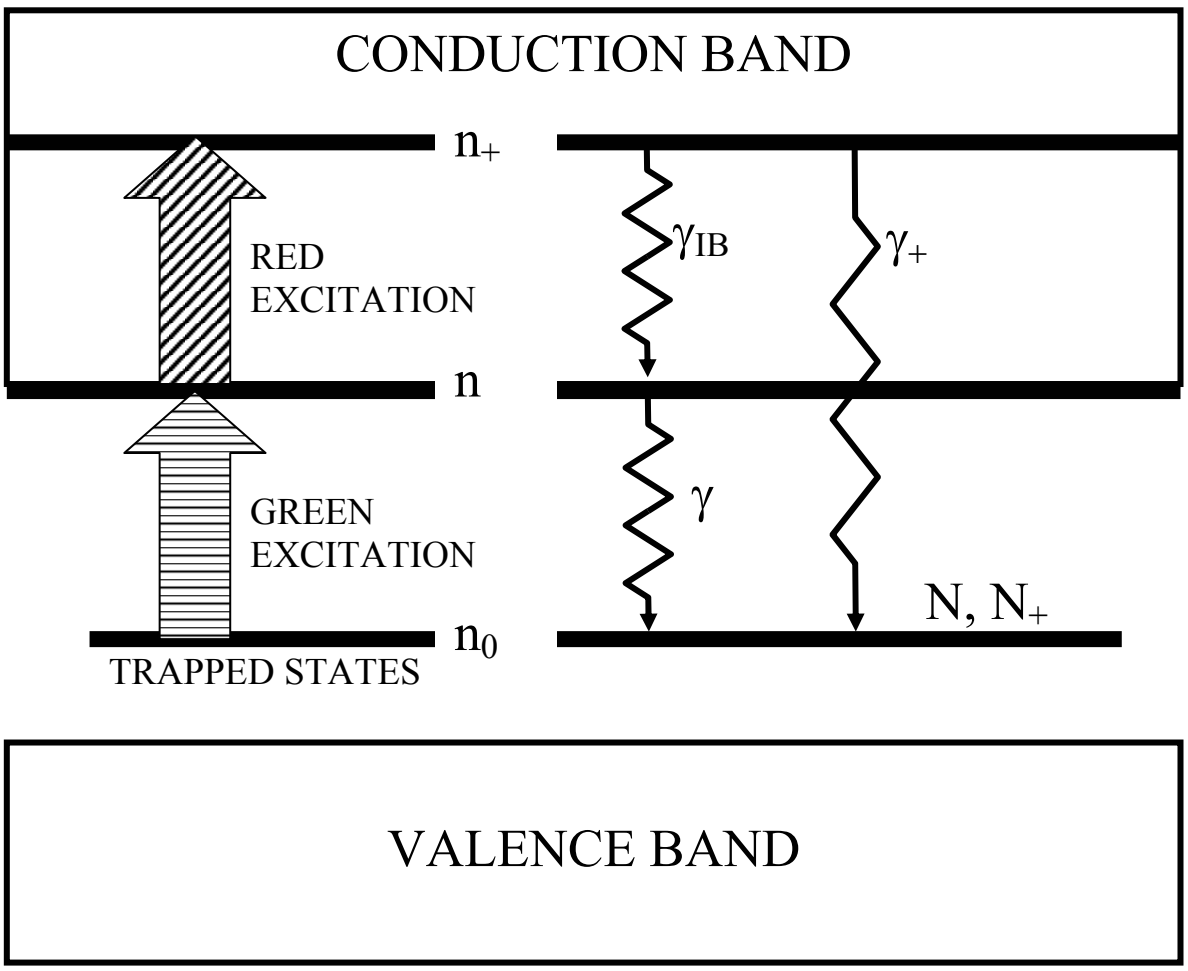

Fig. 5.1 scheme of the electronic energy levels of the process

electron distributions; $\vec{J}$ is instead the current-density vector eq.(5.3.c), which is given only by electron populations moving with different mobilities, according to their energy levels and conduction band curvature, inside the same conducting electric field $\vec{E}_{CD}$.

In the steady state regime, the current-density vector has vanishing divergence eq. (5.3.d) according to the charge continuity law. Thus, all the rate equations in eq.s(5.1) should be vanishing too, which brings to analytical solutions for the electron carrier populations n and n_+:

$$n = \gamma n_{bg} \frac{\sigma_G I_G \left(\gamma_{IB} + \gamma_+ N\right) + \gamma n_{bg}}{\sigma_R I_R \left(\sigma_G I_G \gamma_+ + \gamma\gamma_+ n_{bg}\right) + \sigma_G I_G \gamma\left(\gamma_{IB} + \gamma_+ N\right) + \gamma^2 n_{bg}}$$
$$n_+ = \gamma n_{bg} \frac{\sigma_R I_R \left(\sigma_G I_G + \gamma n_{bg}\right)}{\sigma_R I_R \left(\sigma_G I_G \gamma_+ + \gamma\gamma_+ n_{bg}\right) + \sigma_G I_G \gamma\left(\gamma_{IB} + \gamma_+ N\right) + \gamma^2 n_{bg}} \qquad (5.4)$$

where n_{bg} is the steady state electron population that is responsible for the electric current just in presence of the background illumination, i.e. without the red signal. Both these carrier populations contribute to the current density vector through their mobilites, according to eq.(5.3.c) and especially to eq.(5.3.d) which states that this vector must be constant and uniform in each position inside the crystal. Thus the conducting electric field $\vec{E}_{CD}$ must suffer a spatial modulation to account for the different drift mobility of the electrons in the two energy levels n and n_+:

$$\vec{E}_{CD} = \frac{\vec{J}}{e(\mu n + \mu_+ n_+)} \qquad (5.5)$$

Substituting eq.s (5.4) into (5.5), the conducting field takes the expression:

$$\vec{E}_{CD} = \vec{E}_{bias}\ \frac{\mu}{\gamma}\frac{\gamma\left[\sigma_G I_G\left(\gamma_{IB}+\gamma_+ N\right)+\gamma\gamma_{IB}n_{bg}\right]+\sigma_R I_R\gamma_+\left[\sigma_G I_G+\gamma n_{bg}\right]}{\mu\left[\sigma_G I_G\left(\gamma_{IB}+\gamma_+ N\right)+\gamma\gamma_{IB}n_{0,bg}\right]+\mu_+\sigma_R I_R\left[\sigma_G I_G+\gamma n_{bg}\right]}, \qquad (5.6)$$

i.e. the externally applied bias $\vec{E}_{bias}$ is modulated by the two electrons distributions and, consequently, modulates the dielectric constant of the PR material because of the electro-optic effect. In fact, assuming for simplicity $\gamma=\gamma_+$, the BSO dielectric constant gets a nonlinear modulation according to the expression:

$$\delta\varepsilon = -kn_0^2 r_{41}E_{bias}\frac{\alpha+\beta I_R}{\alpha+\beta\eta I_R} = -kn_0^2 r_{41}E_{bias}\frac{1+RI_R}{1+\eta RI_R}, \qquad (5.7)$$

where now n_0 is the linear refractive index of the material, k is the light wave-vector, r_{41} is the electro-optic coefficient, and:

$$\begin{aligned}\alpha &= \mu\left(\sigma_G I_G\left(\gamma_{IB}+\gamma_+ N\right)+\gamma\gamma_{IB}n_{bg}\right)\\ \beta &= \mu\left(\sigma_G I_G+\gamma n_{bg}\right)\end{aligned}, \qquad (5.8)$$

where R denotes the ratio $\frac{\beta}{\alpha}$ and η the ratio $\frac{\mu_+}{\mu}$.

Using a gaussian profile of the red signal beam, Eq.(5.7) effectively gives nonlinear modulations of the dielectric constant, according to the R and η parameters. A first estimation of the η parameter can be obtained by considering the hypothesis that the absorbed red-photon energy entirely goes into kinetic energy of free electrons. Consequently it is possible to write:

$$\frac{1}{2}mv_+^2 - \frac{1}{2}mv^2 = h\upsilon. \qquad (5.9)$$

According to this, the ratio η becomes:

$$\eta = \frac{\mu_+}{\mu} \approx 1 + \frac{h\upsilon}{mv^2} \cong 1.9 \qquad (5.10)$$

A first estimation of the ratio R instead is only dependent on the uniform background intensity I_G and of the current population n_{bg}. It roughly represents the ratio between the n_+ and the n populations and must be much lower than 1. For $R \approx 0$, which corresponds to vanishing I_R, no spatial modulation of the conducting field $\vec{E}_{CD}$ is present. Above $R \approx 0.1$, which corresponds to very low value of background intensity, the conducting field is indeed modulated, but the variation profile is much larger than the laser one, showing a saturating trend that squared the nonlinear dielectric constant. Then the R value must be included among these values.

5.3 Numerical simulations of beam propagation

The light propagation in a PR material with optical activity can be described by the wave equation for the electric vector $\vec{A}$ of the optical field[10,11]:

$$\nabla^2 \vec{A}\left(\vec{r},t\right) - \frac{1}{c^2} \cdot \left[\vec{\varepsilon} \otimes \frac{\partial^2 \vec{A}}{\partial t^2} + \frac{\Gamma}{k}\left(\vec{\nabla} \times \frac{\partial^2 \vec{A}}{\partial t^2} \right) \right] = 0 \qquad (5.11)$$

where c is the light velocity in vacuum, $\vec{\varepsilon}$ is the dielectric tensor of the material, "$\otimes$" is the tensor-vector multiplication, $\Gamma = 2\rho_0 / k$ is the gyration constant (ρ_0 is the optical rotatory power, i.e. the polarization rotation speed, defined as the number of rotation degrees per each millimeter of propagation, whose value at 633 nm is 21.4°/mm) and k the wave vector inside the material. If the material presents a nonlinear behavior, its

dielectric tensor is usually expressed as a linear term and a nonlinear correction caused by the electro-optic effect:

$$\vec{\vec{\varepsilon}} = \vec{\vec{\varepsilon}}_{linear} + \delta\vec{\vec{\varepsilon}} = \begin{bmatrix} n_0^2 & -i\Gamma & 0 \\ i\Gamma & n_0^2 & 0 \\ 0 & 0 & n_0^2 \end{bmatrix} + \begin{bmatrix} 0 & 0 & 0 \\ 0 & -n_0^4 r_{41} E_{CD} & 0 \\ 0 & 0 & 0 \end{bmatrix}. \qquad (5.12)$$

where r_{41} is the electro-optic coefficient and E_{CD} is the local conducting electric field.

For a propagation along the Z-direction, and a bias field applied along the Y-direction, eq.(5.11) becomes:

$$\begin{cases} 2ik\dfrac{\partial A_x}{\partial z} + \dfrac{\partial^2 A_x}{\partial x^2} + \dfrac{\partial^2 A_x}{\partial y^2} - i\Gamma A_y = 0 \\ 2ik\dfrac{\partial A_y}{\partial z} + \dfrac{\partial^2 A_y}{\partial x^2} + \dfrac{\partial^2 A_y}{\partial y^2} + i\Gamma A_x - k^2 n_o^4 r_{41} E_{bias} \dfrac{1 + R\left(|A_x|^2 + |A_y|^2\right)}{1 + \eta R\left(|A_x|^2 + |A_y|^2\right)} A_y = 0 \end{cases}, \qquad (5.13)$$

which have been solved numerically. In particular, to simulate the experimental conditions, propagations of 8 mm (almost 6 diffraction lengths) along the [1̲10] crystallographic direction (*z*-direction) has been considered, with a static bias applied along the [001̲] (*x*-direction).

In the absence of biased field, the conducting field will be homogeneous and no modulation of the dielectric constant will occur. Thus the laser beam diffracts during propagation, as shown in fig. 5.2.

For sufficiently high bias field (for example 60 kV/cm), the modulation of the dielectric constant, induced by the modulation of the conducting field, would be strong enough to compensate the diffraction and thus to cause the beam self-trapping (fig.5.2). Even if the beam diffraction is almost completely compensated, no

pure solitons are generated: in fact the beam intensity slightly fluctuates during propagation, giving an output beam of the same size but different intensity. For this reason it is more correct to call them self-trapped beams instead of solitons.

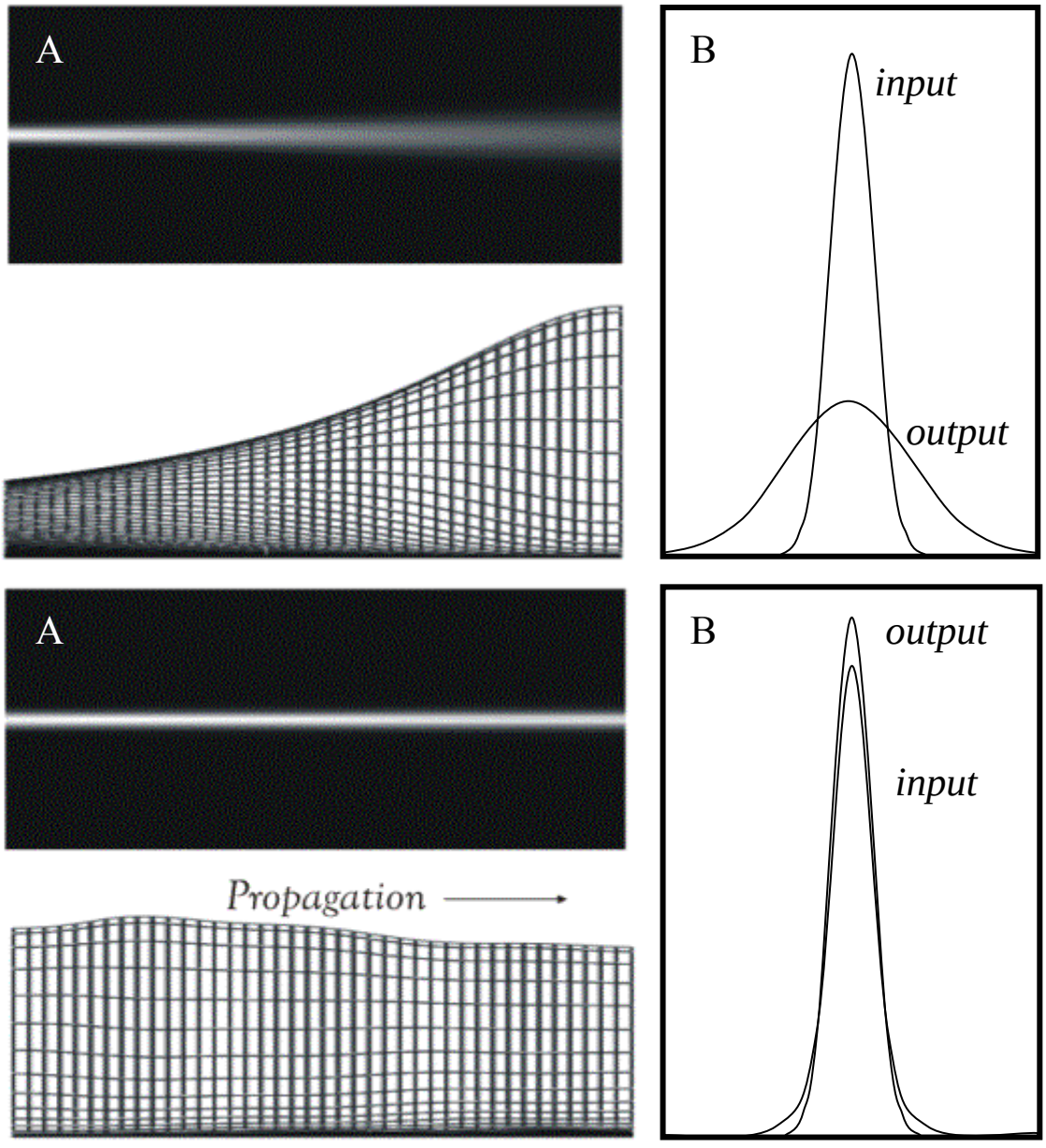

Fig. 5.2. Beam propagations without (0 kV/cm) and with (60 kV/cm) external bias pplied. The external application of the bias field forces the beam toward a self-confined behaviour. However it is clear from the A and B images (A: intensity during propagation; B: input and output intensity profiles) that the propagation is not homogeneous but some losses are present.

Fig.5.3 shows the output beam waists, obtained by numerical simulations, as function of the applied bias field, for different η parameters (R=0.005, I_{red}=200 mW/cm^2). For η<1.9 the self-confinement of the beam is not so efficient, while for η>1.9 (see for example η=2.5) a minimum size of about 80% of the input beam is obtained for $E_{bias} \cong$ 64 kV/cm.

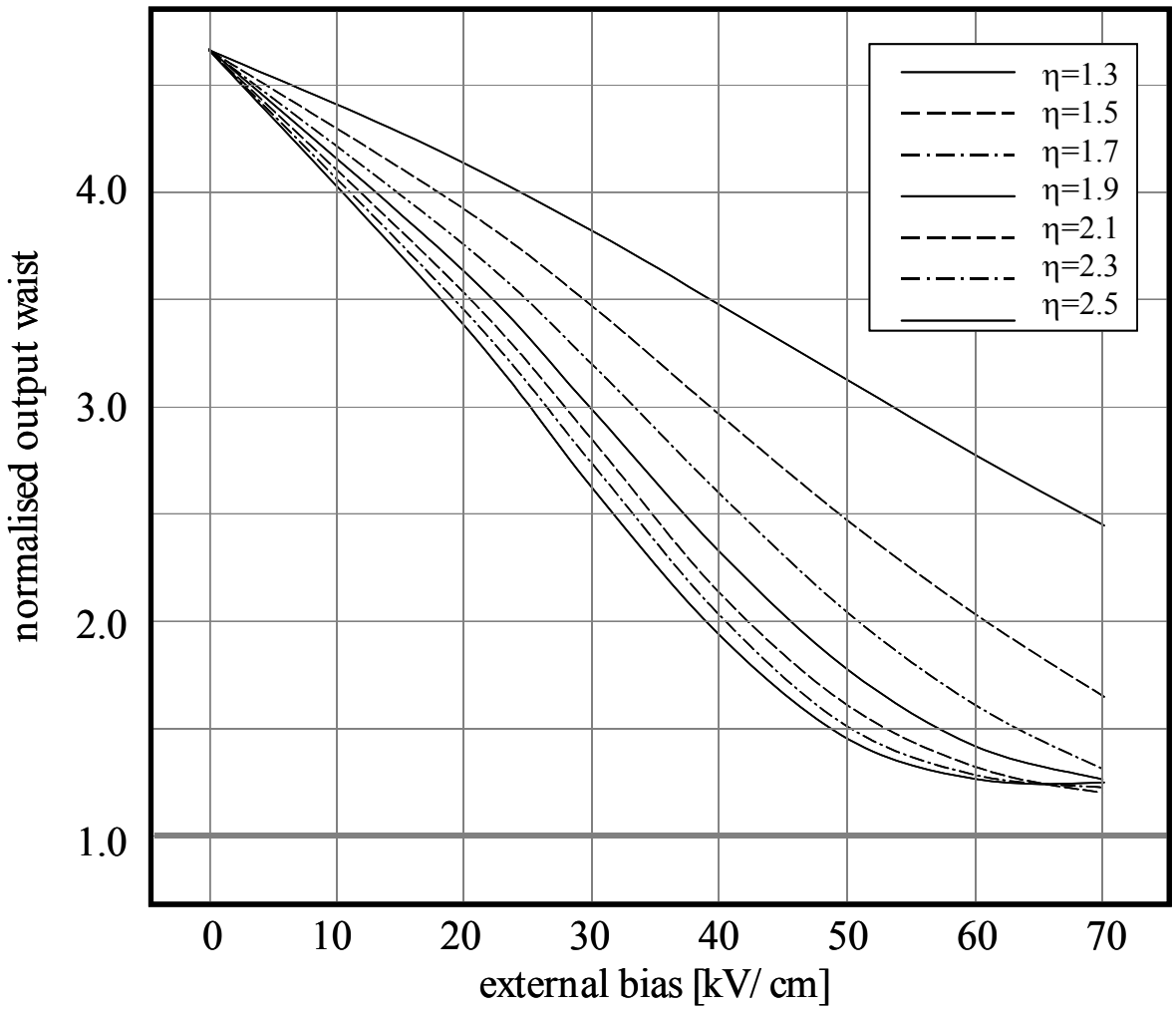

Fig. 5.3. Output beam waist as function of the external bias and for different values of the η parameter (Ired=200 mW/cm2, R=0.005).

The influence of the R parameter on the self-trapping process is then shown in fig.5.4. The output waist decreases exponentially with a characteristic intensity parameter (called *trapping intensity*)

$$w_{nonlinear}^{out} = w_{linear}^{out} e^{-\frac{I_R}{I_{trapping}}}. \qquad (5.14)$$

This exponential behavior points towards the randomness buried in the formation of the spatial field profile. From the rate equations (5.1-5.2), the carriers n_+,

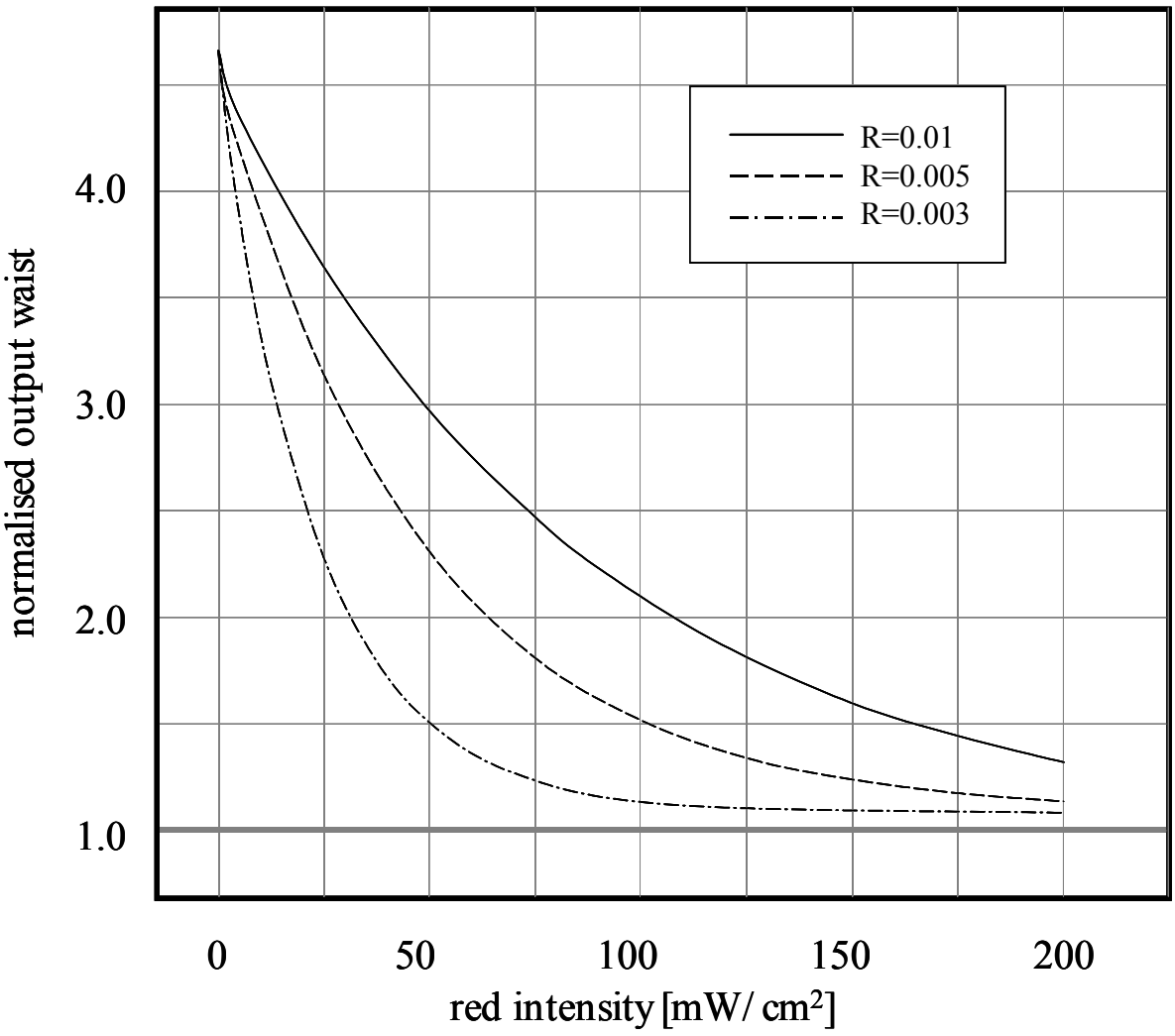

Fig 5.4. Normalised output beam waist as function of the intensity of the red light beam for different values of the R parameter (η=1.9).

main responsible for spatial modulation of the conducting field, increases exponentially in time, to a stable value $\approx \frac{I_R}{N_+}$. This effect appears as the exponential decay of output waist on intensity scale.

5.4 Experimental evidence of beam self-trapping

The scheme of the experimental set-up is shown in fig.5.5. The light beam from an Ar+ laser at 514.5 nm is used for the background illumination of the sample. This background is expanded using a spatial filter with magnification, and then sent to the sample along its [1$\underline{1}$0] crystallographic direction, giving an homogeneous illumination on the crystal. The signal beam, responsible for soliton formation, was generated by

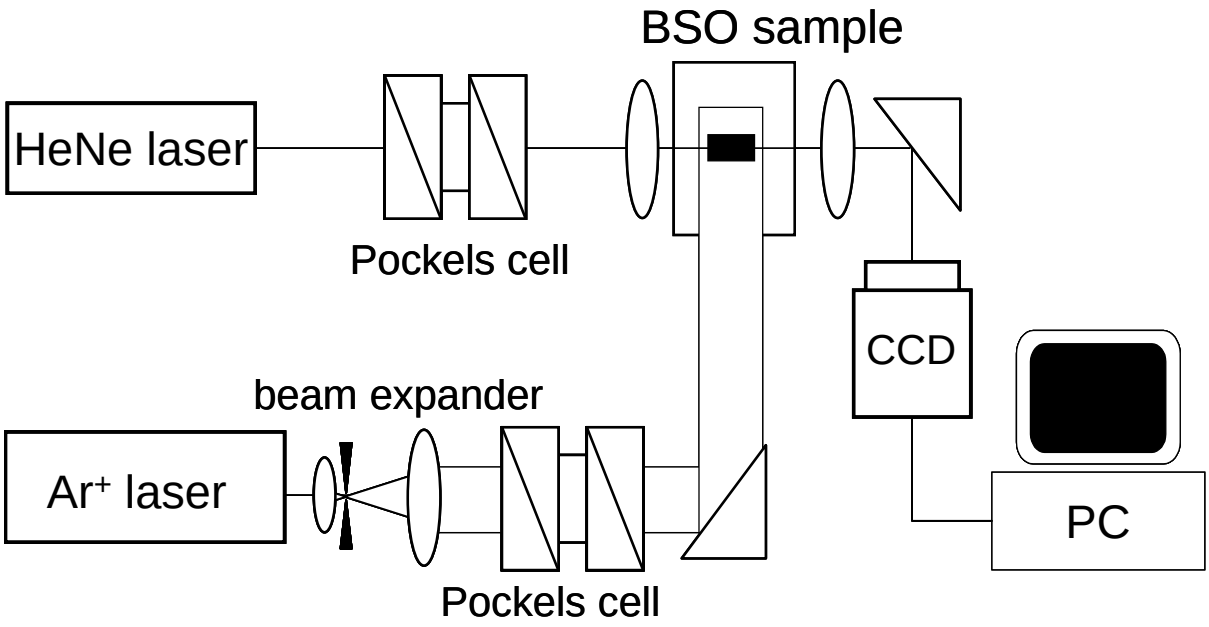

Fig 5.5. Experimental set-up.

a HeNe laser and focused on the sample input face with a waist of about 10 μm. Two Pockels cells, one for the background and one for the signal respectively, regulated the intensities of the two beams and their polarization. The BSO crystal, 8 mm long along the [110] crystallographic direction (propagation direction), was biased along the [001] direction with a static electric field variable up to 53 kV/cm. In order to avoid electric discharge between electrodes, the sample was kept within an insulating cell. After the sample, the laser beam was imaged on a CCD camera by an optical system with a magnification of 43.

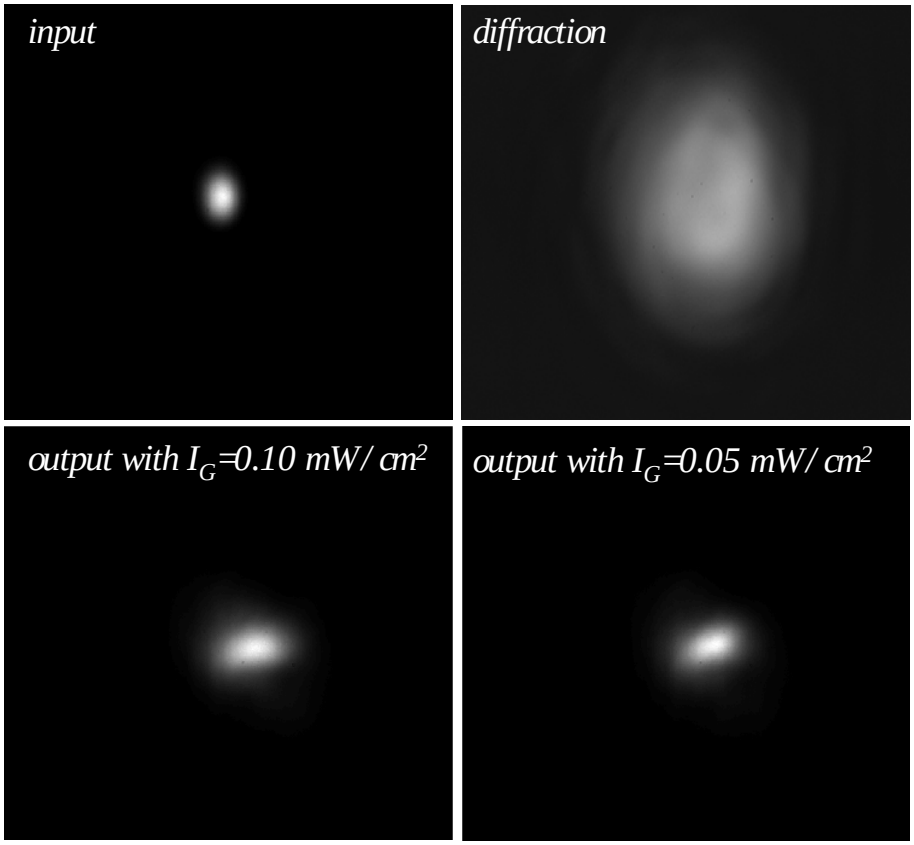

Fig. 5.6. Experimental images of the beam at 633 nm taken at the input and output crystal planes.

In fig.5.6 the images of the beam self-trapping are reported. In particular the image of the input has been reported for comparison as well as the output diffracting beam. The two self confined beams have been obtained using different intensities of the background green beam. In fig.5.7 it is reported the experimental waists (squares), obtained for the two background intensities of 100 and 50 $\mu W/cm^2$, together with the exponential fits from the theory: The 100 $\mu W/cm^2$ background trend has been fitted with a trapping intensity of 74.8 mW/cm^2 (for the signal red light), while the 50 $\mu W/cm^2$ has a trapping intensity of 33.7 mW/cm^2. These values give, for the experimental case, R=0.005 and η=2.1, which are matching with the hypothesis.

References

1. V.I.Vlad, V.Babin, M.Bertolotti, E.Fazio and M.Zitelli, Proc. Romanian Academy A1, 25 (2000).
2. V.I.Vlad, V.Babin, M.Bertolotti and E.Fazio, Proc. SPIE 4430, 418(2001).
3. E.Fazio, V. Babin, M. Bertolotti, V.I. Vlad, Phys. Rev. E 66, 016605 (2002).
4. E Fazio, F Mariani, M Bertolotti, V Babin and V Vlad, J. Opt. A: Pure Appl. Opt. 3, 466 (2001).
5. E.Fazio, F. Mariani, A. Funto, M.Zitelli, M.Bertolotti, V.Babin and V.I.Vlad, Proc. SPIE 4430, 411 (2001).
6. E.Fazio, W. Ramadan, A. Belardini, A. Bosco, M. Bertolotti, A. Petris, V.I. Vlad, Phys. Rev. E 67, 026611 (2003).
7. E.Fazio, W. Ramadan, M. Bertolotti, A. Petris, V.I. Vlad, in press on J. Opt. A: Pure Appl. Opt.
8. A. Grunnet-Jepsen, I. Aubrecht, L. Solymar, J. Opt. Soc. Am. B 12, 921 (1995).
9. O.V. Kobozev, S.M. Shandarov, A.A. Kamshilin, V.V. Prokofiev, J. Opt. A: Pure Appl. Opt. 1, 442 (1999).

Chapter 6

Solitons by femtosecond pulses in $LiNbO_3$

6.1 Introduction

The second material used for studying the formation of spatial solitons by photorefractive effect is the lithium niobate ($LiNbO_3$ - LNB), which is actually a widely used material for optoelectronic applications. Among all the materials which show photorefractive effects, the LNB shows a very slow relaxation time[1]. This property makes possible in such material writing waveguides practically permanent[2]. In this experiment spatial solitons in LNB have been generated using ultrashort laser pulses. This was possible and just because LNB has such a long dielectric relaxation time, and consequently a large charge accumulation is possible over a long temporal integration.

Photorefractive nonlinearities in LNB are based either on the generation of a local photovoltaic electric field[3], or the generation of bound carrier populations, that can produce a screening of an uniform externally-applied bias[3], or on a combination of the two[4,5]. Following these possibilities, analytical predictions have been made for obtaining spatial solitons, either bright o dark [5,6,7]. Experimentally dark solitons have been observed[8,9,10] without any external bias, in both open and closed circuit configurations[11]. Transition from defocusing to focusing behaviors of photovoltaic

nonlinearities have been predicted and experimentally observed[1] just for the open circuit configuration, and, as written in the abstract. Screening-photovoltaic bright solitons where indeed observed and experimentally characterized[2] using a CW laser beam in the green. In such a case a strong bias was applied to increase the screening field with respect to the photovoltaic one. It must be pointed out here that all the experimental testing for photorefractive soliton generation have been performed either with CW laser light or with relatively long pulses[12] (100 ps).

6.2 Experiment

The experimental set-up is shown in fig. 6.1. A nominally pure LNB crystal, 5 mm long, was electrically biased at 35 kV/cm along its optical-axis direction ([001] crystallographic direction). A light beam from a Ti-Sapphire laser was focused down to about 9 μm (HWHM) on the input (100) face of the crystal. This beam was constituted by laser pulses at 800 nm, as long as 75 fs at the input face, at the repetition rate of 78 MHz, and average power of about 16 mW. The linear dispersion of the pulses inside the LNB crystal was 9.9 fs/mm; nonlinear dispersion was negligible. Experimental measurements were performed with and without an uniform background illumination: such an illumination was obtained by using a CW Argon-ion laser beam, at 514 nm, expanded and sent to the (010) crystal face. At the end, the output crystal face was imaged on the CCD sensor of a computer interfaced camera.

The dynamics of the Ti-Sapphire laser beam propagating inside the lithium niobate without the background illumination is shown in fig. 6.2 where, for

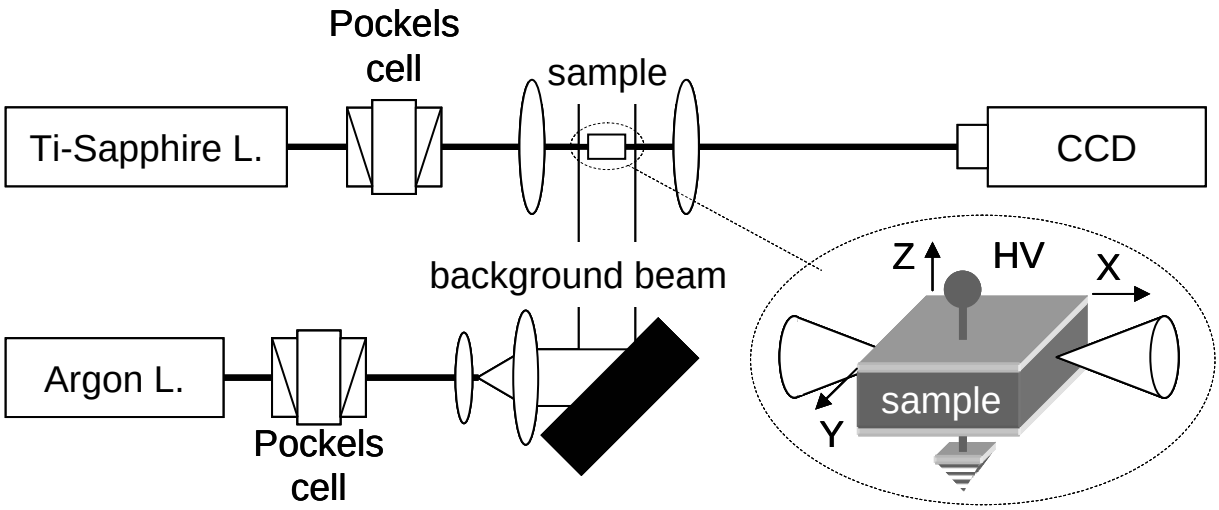

Fig. 6.1: Experimental set-up. 75 fs-long pulses from a Ti-Sapphire laser was focused down to 10 mm of waist on a lithium niobate crystal, that was biased along its Z-axis. The output face was imaged on a CCD camera. Two sets of measurements were performed, without and with a uniform transversal illumination provided by a CW Argon Laser.

comparison, the beam profile at the input face of the crystal is shown as well. The linear diffraction inside the crystal is evident at the initial experimental time called 0 min, for which both the bias and the beam were turned on. In the very initial part of the measurements the beam experienced a self-focusing which reduced the output size of the beam after 20 min. Even if a residual self-focusing remained active, after approximately 40 min, the beam started to break down into two sections along the vertical direction. Such a breaking is the starting of a 1-dimensional dark soliton (with confinement along the optical axis direction) which is completely formed after 1 hour from the experiment starting. The dark soliton is not stable because in the experiment a Gaussian beam was injected at the input instead of an uniform illumination with a

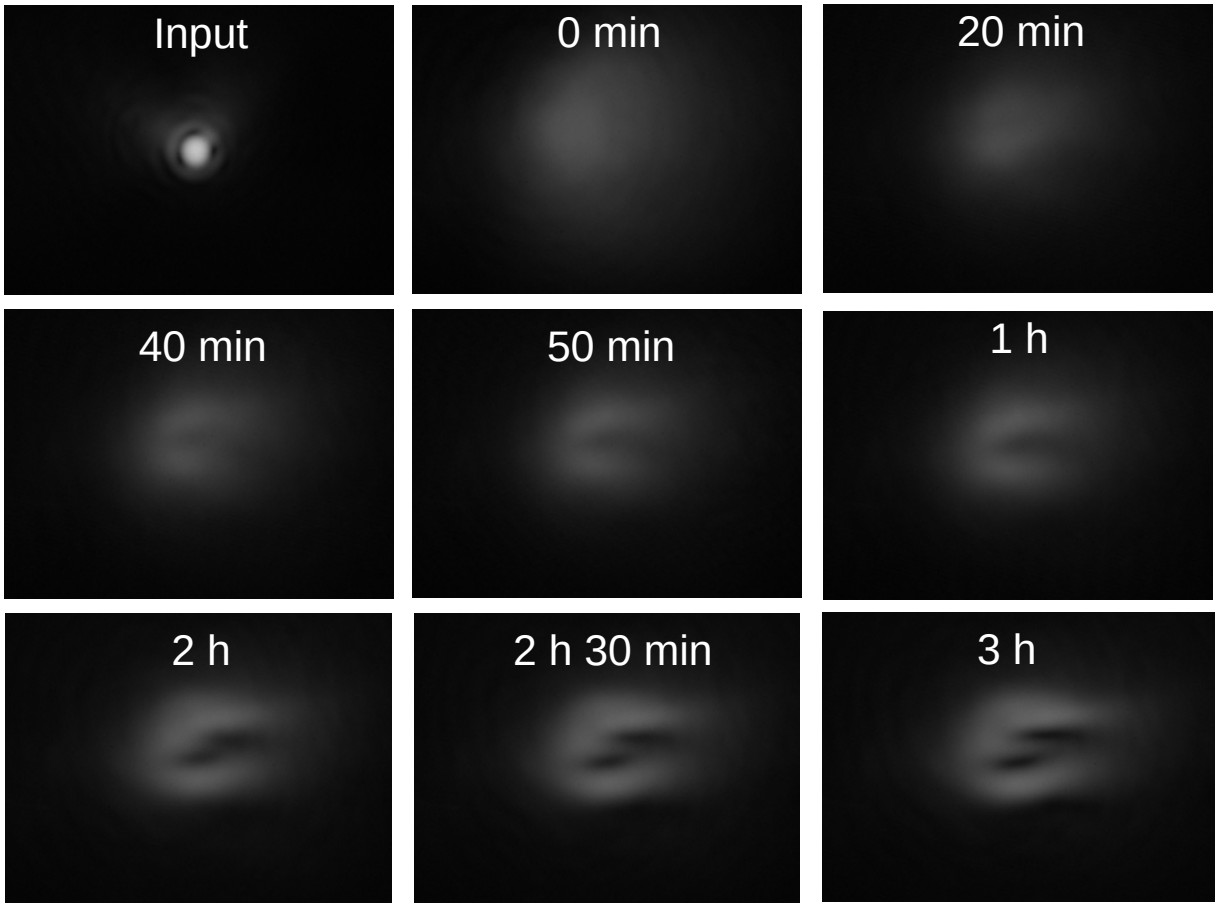

Fig. 6.2: A first set of measurements was performed without a transversal background illumination. In the first minutes after the bias voltage and the beam are turned on, the beam experienced a slight selfocusing (in fact after 20 min the beam is a bit smaller than the initial case. However this selfocusing is not able to reach a stable solitonic regime. A defocusing nonlinearity became dominant after 40 min, breaking the beam and giving rise to a dark soliton. However such a dark soliton is not stable because of the bell-shaped signal beam, breaking down into two different dark solitons after 2 hours.

dark seed. For such a reason 1 hour later, which means after 2 hours from the starting, the dark soliton broke down into two dark solitons. After 3 hours the experiment was interrupted, even if we expected further breaking of these solitons into other dark solitons. Please note that the horizontal dimension of the dark soliton

became smaller after the first splitting: we might expect that after some splitting a 2-dimensional dark soliton could be reached.

The dynamics of the Ti-Sapphire laser beam propagating inside the lithium niobate this time with the background illumination is shown in fig. 6.3, where the beam profile at the input face is again shown for comparison. The background beam was set in order to give an uniform illumination as intense as some tens of mW/cm^2. In such a case the selfocusing was very efficient since the first minutes, firstly along the vertical direction which corresponds to the optical axis of the crystal. This process

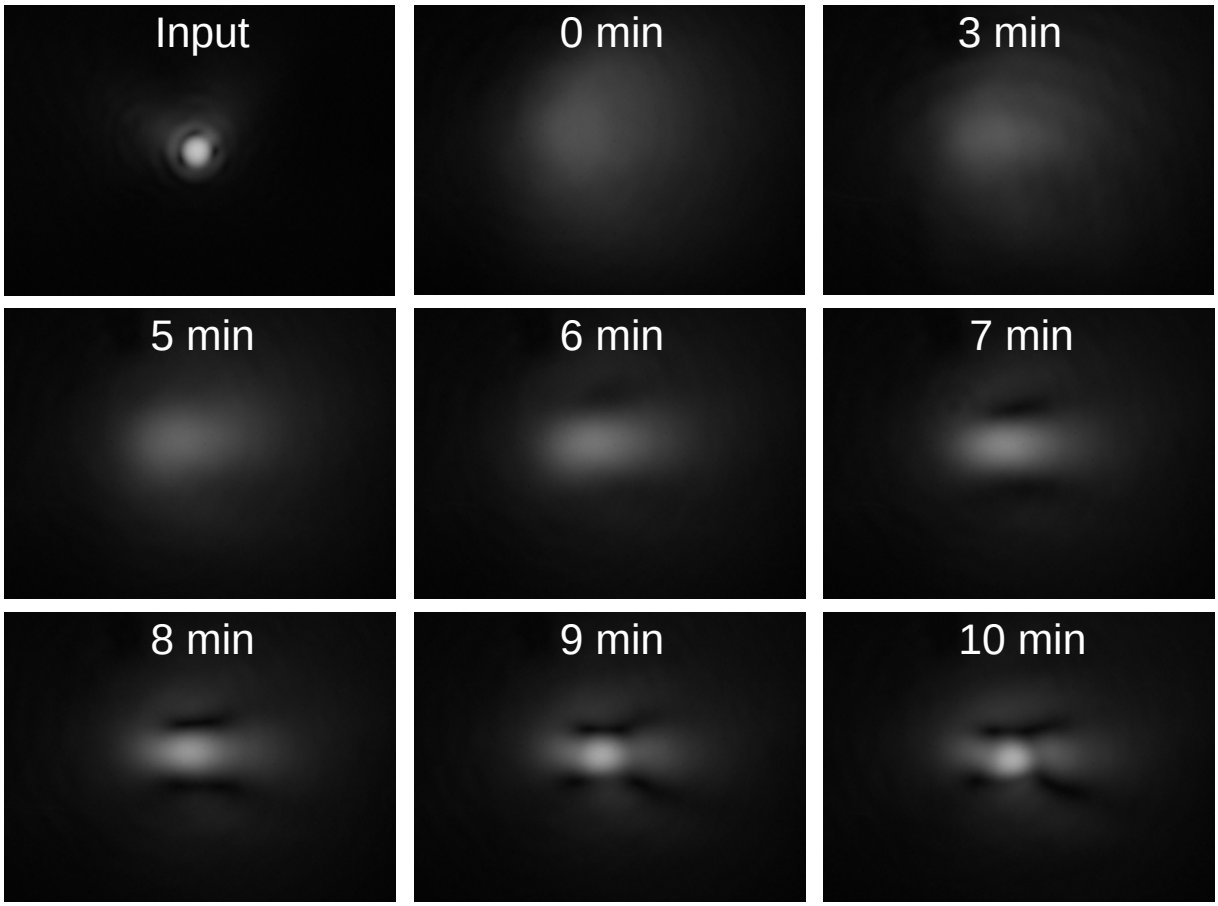

Fig. 6.3: The second set of measurements was performed with a transversal background illumination. In such a case the selfocusing is really efficient, and generates a circular bright soliton in only 10 min after the bias voltage and the beam are turned on.

was already observed in CW regime[2], where this fast axis confined the beam much faster than the other (slow axis). As shown in fig. 6.4, the soliton size (20±1 μm , FWHM) along the fast axis was reached after 8 min while along the slow horizontal axis it was slower, reaching the same size after about 11 min. The beam shape along the slow axis was indeed changing from Gaussian to squared hyperbolic secant after about 8 min, where the temporal evolution for the slow component shows a deep decreasing of the transverse size. As previously reported also in this case solitons with circular sections (single-mode fibre type) are reached in LNB; however due to high light intensity (1.1 GW/cm^2) and the high bias field applied (35 kV/cm), a strong bending of the beam was observed, as high as 40-50 μm, which slightly distorts the beam.

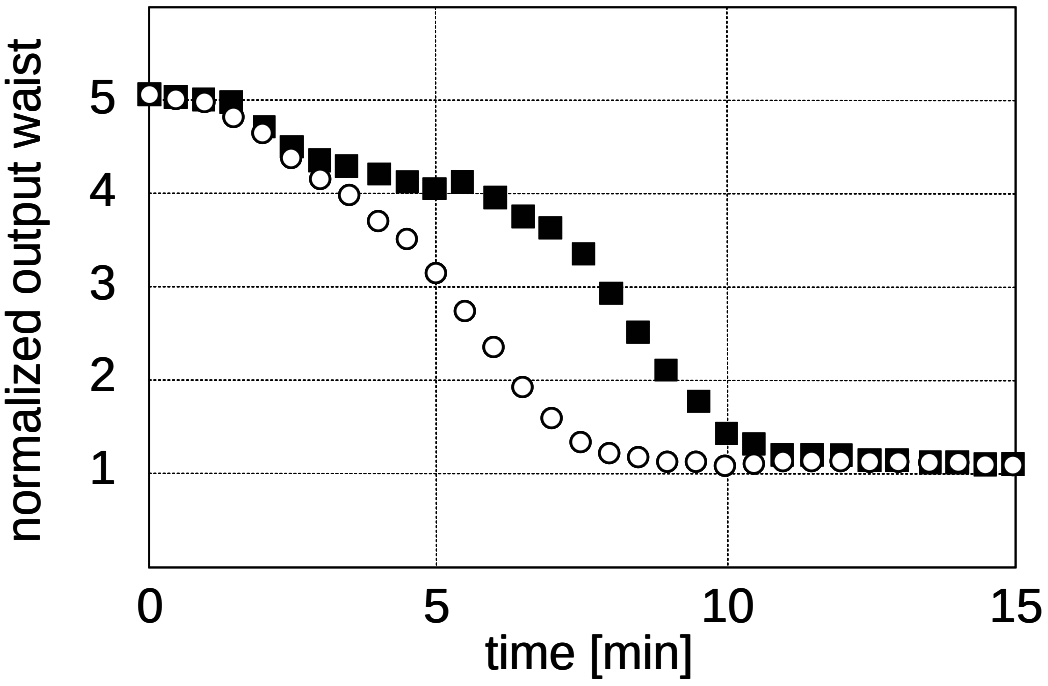

Fig. 6.4: Temporal evolution of the bright soliton formation (output waist normalized to the input one) for the fast-vertical (open circles) and slow- horizontal (closed squares) transverse directions of the beam profile.

The different behaviors of the soliton formation without and with the background are explained as follow. When the short-pulse beam at 800 nm is injected in the sample, two main absorption processes occur, direct transitions from shallow traps[1] and two-photon-absorption[13,14,15,16] (TPA). Both these processes, as previously reported, can occur in pure LNB, being completely independent from the doping level or purity of the crystal. TPA can be really high or can even overpass the linear absorption for elevate intensities: in the present case the linear absorption was as high as 0.06 cm^{-1}, while the TPA, at 1 GW/cm^2, was 0.25 cm^{-1}, 4 times larger. Green-induced infrared absorption was observed[12,17] in doped LNB and at green light intensities much higher than those used here (few mW/cm^2), factors that led us to neglect such a process in our experiments. According to the absorption transitions, a free electron population is generated as well as free-hole and bound-hole populations. Free-carriers are then mobilized by photovoltaic field, much stronger in the center of the beam than at the boundary due to the nonlinear nature of the absorption processes. Due to the purity of the crystal, such carriers are free of moving for long inside the lattice before recombining, giving rise to a weak current flow. The bound ionized levels, centered inside the beam, generate a screening field for the applied bias and for the photovoltaic field. Such a field starts producing an initial selfocusing of the beam. However the screening effect cannot be complete because the screening field expands across a large area of the crystal, due to the long average-free-path of the carriers. Consequently the photovoltaic field remains dominant in the core of the laser beam, making it split into a dark soliton due to the

negative variation of refractive index associated to it. The observed dark soliton is not stable because its bright sides are bell-shaped[18], forcing it to split in two different dark solitons.

When the uniform background is turned on, absorption from deep levels occurs all around, originating a uniform distribution of ionized traps. Thus the average-free-path of the electrons is strongly reduced in comparison with the previous case: the electrons re-saturate the ionized traps just at the beam boundary. Consequently the screening field is now taking place between two well localized charge populations, i.e. the ionized traps inside the beam (both shallow and deep traps), positive in charge, and the depleted zone just outside the beam, negative in charge. Such screening effect is now very efficient and rapid and higher that the photovoltaic, inducing a self-trapping of the light.

References

1. C. Anastassiou, M. Shih, M. Mitchell, Z. Chen, M. Segev, Opt. Lett. 23, 924 (1998)
2. E. Fazio, F. Renzi, R. Rinaldi, M. Bertolotti, M. Chauvet, W. Ramadan, A. Petris, V.I. Vlad, Appl. Phys. Lett. 85, 2193 (2004)
3. A.M.Glass, D. von der Linde, T.J. Negran, Appl. Phys. Lett. 25, 233 (1974)
4. A.M. Glass, Opt. Engineering 17, 11-20 (1978)
5. L. Keqing, Z. Yanpeng, T. Tiantong, H. Xun, J. Opt. A: Pure Appl. Opt. 3, 262 (2001)
6. G.C. Valley, M. Segev, B. Crosignani, A. Yariv, M.M. Fejer, M.C. Bashaw, Phys. Rev. A 50, R4457 (1994);
7. H. Chun-Feng, L. Bin, S. Xiu-Dong, J. Yong-Yuan, X. Ke-Bin, Chinese Physics 10, 310 (2001)
8. M.Taya, M.C. Bashaw, M.M. Fejer, M. Segev, G.C. Valley, Phys. Rev. A 52, 3095-3100 (1995)

9. Z. Chen, M. Segev, D. W. Wilson, R. Muller, P. D. Maker, Phys. Rev. Lett. 78, 2948 (1997).
10. G. Couton, H. Maillotte, R. Giust, M. Chauvet. Electr. Lett. **39**, 286 (2003).
11. M. Chauvet, J. Opt. Soc. Am. B 20, 2515-2522 (2003)
12. N. Fressengeas, D. Wolfensberger, J. Maufoy and G. Kugel, J.Appl. Phys. 85, 2062(1999)
13. D. von der Linde, A.M.Glass, K.F. Rodgers, Appl. Phys. Lett. 25, 155 (1974)
14. D. von der Linde, A.M.Glass, K.F. Rodgers, J. Appl. Phys. 47, 217 (1976);
15. H. Kurz, D. von der Linde, Ferroelectrics 21, 621 (1978)
16. H.Li, F.Zhou, X.Zhang, W. Ji, Appl. Phys. B 64, 659 (1997)
17. Y. Furukawa, K. Kitamura, A. Alexandrovski, R.K. Route, M.M. Fejer, G. Foulon, Appl. Phys. Lett. 78, 1970 (2001)
18. V.E. Zakharov, A.B. Shabat, Sov. Phys. JEPT 36, 823 (1973)

Conclusions

The development of all-optical processing is a mandatory step for improving ultrafast photonics networks architectures, whose performances are still limited by the need of optic-electric conversion.

In the present thesis all-optical signal processing have been deeply investigated, and I have proposed new solutions for both photonic circuits for signal processing and basic phenomena and devices to increase the performances of such circuits, in terms of lower intensities needed to reach the switching thresholds, input-phase-independent processes and self-confined beams with ultra-low losses and dispersion.

In particular in chapter 1, it has been proposed a new signal processing procedure using the well-known second order nonlinear processes such as second-harmonic generation and parametric down amplification. In fact, from the point of view of binary logic, those processes can be used for implementing fundamental operations of a complete Boolean algebra. This new way of processing optical data presents two main advantages: the possibility of parallel operation, which allows bit-to-bit processing of matrices of binary numbers at once, and the non-resonant response of the materials which means that operation could be performed with bits encoded over ultra-short light pulses (down to tens of femtoseconds), at really high repetition rates (10^{13}-10^{14} bits/s). In order to make clear how is possible to build up complex circuit, starting from the elementary logical gates, a notation for indicating any possible functionalities realizable by such processes has been introduced.

Experimentally, it has been proven the implementation of a XOR and an AND gate by a type-II second-harmonic generation set-up. Those binary operations, performed over single-bit digits, realized themselves a single-bit adder (see fig. 1.7). Starting from this experimental result, Several other functionalities based on the proven logical gates, such

as a multi-bit parallel adder and a multiplexer and demultiplexer have been thought and here illustrated, and they will be realized in the next future.

In the second chapter, the dimension reduction of the device has been investigated analyzing the possibility to realize second-order nonlinear processes in one-dimensional photonic crystal. It was here experimentally demonstrated the possibility to enhance the conversion efficiency by tailoring the material structure which gives, as result, larger effective nonlinear properties. In particular the first realization of type-II second-harmonic generation (the same process used for implementing the logical gates described in chapter 1) in photonic crystal is presented. The total sample thickness was 3.5μm, i.e. 200 times thinner than the BBO crystal used in the former experiment (described in chapter 1). The actual efficiency of the process was of course much smaller (it depends on the second power of the interacting length) but a strong enhancement of the nonlinearity has been measured: the sample nonlinearity shown in this experiment was 52 pm/V: 25 times higher than the BBO's one.

In chapter 3, the problem of decreasing the switching threshold using second-order nonlinear materials in Fabry–Perot cavities has been investigated from the theoretical point of view. In this different approach, the proposed device switches a ultra-low intensity signal by changing both its phase and amplitude within the resonator (not just the amplitude as in chapters 1 and 2). The Fabry–Perot cavity is designed to work for a fundamental light frequency whose characteristics can be modified by a second driving field at the second harmonic. The studied process is input-phase-independent (and consequently active for incoherent fields), being chosen type-II phase-matching where just one of two polarizations at the fundamental frequency is injected from outside. The nonlinear behavior of the cavity have been characterized by mean of linear and nonlinear parameters (mirrors reflectivity, cavity detuning, phase mismatch, etc..). By using an effective nonlinearity of the order of a few tens of pm/V (typical values for organic crystals

or semiconductors), all-optical bistability and all-optical switching of really low-intensity signals (a few hundreds of W/cm^2) have been found by pumping the cavity with incoherent second-harmonic beams as low as 100 k W/cm^2.

The third part (chapters 4, 5, 6) of this work deals with the generation of spatial solitons by photorefractive effect. Such solitons are fundamental for photonic circuits because they represent the first and unique case of self-written waveguides which are also, in a sense, self-aligning. Moreover it was previously demonstrated that the photorefractive nonlinearity can be permanently written or erased, factors that make it really attractive for applications.

In chapter 4, it is presented the experimental evidence of generation of (2+1)-dimensional solitons over 4.5 diffraction lengths of propagation in BSO crystals, a photorefractive material with large optical activity. The experimental solitonic state has been reached numerically by analyzing the dynamics of the soliton formation. We have found that it is influenced by an acceleration of the angular speed of light polarization (which prevents the beam from broadening by making the polarization rotation period much shorter than the diffraction length) and contemporarily by an induced birefringence. The soliton is formed where the induced birefringence becomes constant across the beam, and the polarization is trapped in a stable loop around an attraction state. The numerical analysis of the soliton formation guided the experimental investigation, whose results are in good agreement with the previously proposed-analytical solutions for the soliton.

In chapter 5 it is presented for the first time experimental evidence of the possibility to produce self-confined light beams at non-directly absorbed wavelengths. The process involves a two-step absorption process, where the electrons are first excited to the conduction band by a background absorbed beam, and then are excited towards higher levels in the conduction band by second red beam. If this second red beam is spatially modulated, and a static bias field is applied, a current flows inside the material which is

spatially modulated as well and which can locally modify the dielectric constant of the material by the electro-optic effect. The numerical simulations performed confirm that self-trapped beams can be generated and that the beam waist shrinkage follows an exponential trend. The experimental tests that have been performed confirmed both an efficient self-trapping of the red-light beams and the exponential shrinkage trend.

This new process for using the electro-optic effect could push the applications of spatial solitons in photorefractive materials towards the infrared spectrum even if the material did not show any absorption in the region, almost with continuity.

Finally, in chapter 6 it is reported the generation of spatial solitons by using 75 fs long pulses at 800 nm. Photorefractive nonlinearities can grow up even in such extreme case due to a slow accumulation of charges. Thus two different regimes have been experimentally identified, without and with an uniform background illumination of the same, which gave rise to dark and bright solitons respectively. Such background illumination modulates the average-free-path of free carriers, making either the photovoltaic or the screening effect dominate over the other one.

Publications

[1] A. Bosco, E. Fazio, M. Bertolotti, C. Cojocaru, J. Martorell, “Low-intensity optical bistability in an active Fabry-Perot mirror induced by input-phase-insensitive parametric down conversion” Appl. Opt., 41 (2002).

[2] E. Fazio, W. Ramadan, A. Belardini, A. Bosco, M. Bertolotti, A. Petris, V. I. Vlad “*(2+1)-dimensional soliton formation in photorefractive* $Bi_{12}SiO_{20}$ *crystals*“ Phys. Rev. E 67, (2003)

[3] W. Ramadan, E. Fazio, A. Mascioletti, F. Inam, R. Rinaldi, A. Bosco, V. I. Vlad, A. Petris and M. Bertolotti “*Stationary self-confined beams at 633 nm in Bi12SiO20 crystals*” J. Opt. A: Pure and Appl. Opt., 5 (2003) S432–S436

[4] E. Fazio, A. Bosco, R. Rinaldi, A. Mascioletti, F. Renzi, M. Bertolotti, W. Ramadan, V. Babin, A. Petris, V.I. Vlad, “*Light polarization dynamics in self-confined beams and solitons propagating in photorefractive media*”, Proc. SPIE Vol. 5581, p. 51-55 (2003)

[5] A. Bosco, M. Centini, L. Sciscione, C. Sibilia, E. Fazio and M. Bertolotti, A. Fiore, A. Convertino, L. Cerri, M. Scalora, “*Noncollinear type-II second-harmonic generation in a* $Al_{(0.3)}Ga_{(0.7)}As/Al_2O_3$ *one-dimensional photonic crystal*”, Appl. Phys. Lett., 84 (2004)

[6] A. Bosco, L. Biader-Ceipidor, E. Fazio, M. Bertolotti “All-optical parallel Boolean algebra” Proc. SPIE Vol. 5453 (2004), p. 305-310, (Micro-Optics, VC-SELs, and Photonic Interconnects; H. Thienpont, K. D. Choquette, M. R. Taghizadeh Eds.)

[7] A. Bosco, M. Centini, L. Sciscione, C. Sibilia, E. Fazio and M. Bertolotti, A. Fiore, A. Convertino, L. Cerri, M. Scalora, “*Noncollinear type-II second-harmonic generation in a* $Al_{(0.3)}Ga_{(0.7)}As/Al_2O_3$ *one-dimensional photonic bandgap structure*”, Proc. SPIE Vol 5450 (2004), p. 269-274, (Photonic Crystal Materials and Nanostructures, R. M. De La Rue, P. Viktorovitch, C. M. Sotomayor Torres, M. Midrio Eds.)

[8] A. Petris, A. Bosco, V. I. Vlad, M. Chauvet, M. Bertolotti and E. Fazio, “*Photorefractive solitons generated by femtosecond pulses in lithium niobate*” in press on Appl. Phys. Lett.

[9] E. Fazio, W. Ramadan, A. Petris, M. Chauvet, A. Bosco, V. I. Vlad, M. Bertolotti “*Writing single-mode waveguide in lithium niobate by ultralow-intensity solitons*” in press on Appl. Surf. Science

[10] V. I. Vlad, E. Fazio, M. Bertolotti, A. Bosco, A. Petris, "*Laser generated soliton waveguides in photorefractive crystals"*, in press on Appl. Surf. Science

Submitted

[1] A. Bosco, L. Biader-Ceipidor, E. Fazio, M. Bertolotti "*All-optical parallel signal processing*" submitted to J. Opt. A: Pure and Appl. Opt.

Conferences Contributions

[1] E. Fazio, A. Bosco, M. Bertolotti, C. Cojocaru and J. Martorell, "*Low intensity optical bistability in active $\chi^{(2)}$ Fabry-Perot resonators*" Cleo-Europe Focus Meeting 2001,

[2] E. Fazio, W. Ramadan, A. Bosco, R. Rinaldi, A. Mascioletti, F. Renzi, V.I. Vlad, A. Petris, V. Babin and M. Bertolotti, "*Intensity and polarization dynamics of spatial solitons in photorefractive crystals with large optical activity*", Romopto 2003, Constanza (Romania) September 8th – 11th 2003, INVITED PLENARY LECTURE

[3] A. Bosco, E. Fazio, M. Bertolotti, K. Regelskis, R. Butkus, V. Smilgevicius, A. Piskarskas, *Low-intensity all-optical switching and bistability in nonlinear Fabry-Perot*, Lithuanian Physics Conference, Vilnius (Lithuania), June 19th – 21st 2003, Poster Presentation

[4] E. Fazio, W. Ramadan, A. Bosco, M. Bertolotti, Petris, V. Babin, V.I. Vlad, "*Intensity and polarization dynamics of spatial solitons in photorefractive crystals with large optical activity*", Cleo-Europe 2003, Munich (Germany), June 2003, ORAL Presentation

[5] E. Fazio, W. Ramadan, A. Belardini, A. Bosco, M. Bertolotti, V. Babin, A. Petris, V. I. Vlad, Intensity and polarization dynamics of solitons in BSO crystals, 9th International Conference on Photorefractive Effects, Materials and Devices, Nice, France (2003)

[6] A. Bosco, M. Centini, L. Sciscione, C. Sibilia, E. Fazio and M. Bertolotti, A. Fiore, A. Convertino, L. Cerri, M. Scalora, "*Noncollinear type-II second harmonic generation in a $Al_{(0.3)}Ga_{(0.7)}As/Al_2O_3$ one-dimensional photonic crystal*", CLEO/IECQ 2004, S. Francisco (USA) May 16th – 21st 2004 ORAL Presentation

[7] A. Bosco, L. Biader-Ceipidor, E. Fazio and M. Bertolotti, "*All-optical parallel Boolean algebra*", Photonics Europe 2004, Strasbourg (France) April 26th – 30th 2004, Poster Presentation

[8] A. Bosco, M. Centini, A. Fiore, L. Sciscione, E. Fazio, C. Sibilia, M. Scalora, M. Bertolotti, "*Noncollinear type II second harmonic generation in $Al_{(0.3)}Ga_{(0.7)}As/Al_2O_3$ one-dimensional photonic bandgap structure*", Photonics Europe 2004, Strasbourg (France) April 26th – 30th 2004, ORAL Presentation

[9] A. Bosco, M. Centini, L. Sciscione, C. Sibilia, E. Fazio and M. Bertolotti, A. Fiore, A. Convertino, L. Cerri, M. Scalora, "*Noncollinear type-II second harmonic generation in a $Al_{(0.3)}Ga_{(0.7)}As/Al_2O_3$ one-dimensional photonic bandgap crystal*", International Workshop on Parametric Processes and Periodical Structures, Vilnius (Lithuania), Sept. 26th – 29th 2004 INVITED ORAL PRESENTATION

[10] A. Bosco, R. Butkus, E. Fazio, A. Piskarskas, K. Regelskis, V. Smilgevicius, M. Semeta "*Efficient parametric amplification of optical vortices*" International Workshop on Parametric Processes and Periodical Structures, Vilnius (Lithuania), Sept. 26th – 29th 2004, poster presentation

[11] A. Bosco, E. Fazio, M. Bertolotti "*About all-optical switching and bistability in nonlinear Fabry-Perot*" International Workshop on Parametric Processes and Periodical Structures, Vilnius (Lithuania), Sept. 26th – 29th 2004, poster presentation

[12] A. Bosco, M. Centini, L. Sciscione, C. Sibilia, E. Fazio, M. Bertolotti, A. Fiore, A. Convertino, L. Cerri, M. Scalora, "*NonCollinear Type-II Second Harmonic Generation in Al(0.3)Ga(0.7)As/Al2O3 one dimensional Photonic Bandgap Structures*", Photon 04 Conf.: Quantum Electronics and Photonics (QEP 16), Glasgow (UK), Sept. 6th – 9th 2004

[13] A. Bosco, M. Centini, L. Sciscione, C. Sibilia, E. Fazio, M. Bertolotti, M. Scalora, "*Non linear frequency conversion in finite 1D Photonic crystals: Role of fields' enhancement vs. phase matching conditions"* CostP11&Cost288 Joint meeting, Roma (Italy), October 17th – 20th 2004

[14] A. Bosco, M. Centini, L. Sciscione, C. Sibilia, E. Fazio, M. Bertolotti, A. Fiore, A. Convertino, L. Cerri, M. Scalora. "*One-dimensional photonic crystal: evidence of noncollinear second harmonic generation in a $Al_{(0.3)}Ga_{(0.7)}As/Al_2O_3$ multilayer stack*", 4° Workshop su ottiche diffrattive, Microottica e Microsistemi, Firenze (Italy), April 1st – 2nd 2004.

Participation to international schools

September 1st – 14th 2002; 56th Scottish Universities Summer School in Physics "*Ultrafast Photonics*" (SUSSP 56) – University of S. Andrews – S. Andrews (UK)

September 30th – October 8th 2002; INFM Summer School on "*Progress in Laser Sources and Photonic Devices*" – Capri (Italy)

April 19th – May 1st; Summer School on "*Nanophotonics*" – Cargese (France)

Participation to joint research projects

October 18th – November 30th 2002; June 5th – July 13th 2003; August 16th – October 17th 2004; Participation to the joint research project "*Centre of Excellence in Cell Biology and Lasers CEBIOLA*"; Laser Research Centre of Vilnius University (Lithuania)